



Silicon Carbide for Nuclear Fusion Applications

Helen Elizabeth Pratt

St Peter's College

University of Oxford

Submitted for the degree of Doctor of Philosophy

Hilary Term 2019

Supervisors: David Armstrong and Steve Roberts

Preface

This thesis describes works carried out by the author in the Department of Materials, University of Oxford from October 2013 to April 2019 under the principal supervision of Dr. David E.J. Armstrong and additional supervision by Prof. Steve G. Roberts and was funded through the Science and Technology of Fusion Centre for Doctoral Training (FCDT).

No part of this thesis has been previously submitted for a degree at this or any other university. The work of other authors has been drawn upon and has been referenced and acknowledged in the text. A list of references is given at the end of the thesis.

Some work from this thesis has been reported at the following conferences:

- Culham PhD Showcase, Culham, UK - Effects of Ion Irradiation Damage on Mechanical Behaviour in Silicon Carbide, June 2016. (Invited speaker)
- MS&T 2016, Salt Lake City, USA - Effects of ion-irradiation damage on mechanical behavior in Silicon Carbide, October 2016.
- MRS Fall 2016, Boston, USA - Effects of ion-irradiation damage on mechanical behavior in Silicon Carbide, November 2016.

Abstract

In developing designs for real fusion devices silicon carbide is being considered for multiple uses, including being a structural material. Its performance under the extreme fusion environment, with the added difficulties involved with neutron damage, must be known and mechanical properties quantified for designs to become a reality. This work has directly addressed this issue, by looking at ion irradiated materials and their mechanical properties up to operationally relevant fusion temperatures. By focussing on how these properties change to understand tolerances and behaviours in operationally relevant environments this project has produced some key results in understanding both SiC and radiation damage in ceramics.

Commercially available forms of silicon carbide, as well as Transient Eutectic-Phase (TEP) fabricated materials have been subjected to silicon ion irradiations to peaks of 0.24 and 2.4dpa, at 300°C and 750°C. An additional neon ion implantation was performed to 2.4dpa at 300°C. Various materials were fabricated using the TEP method, focussing on the changes in properties between monolithic and composite samples with varying percentage weights of sintering agents. Changes in mechanical properties were then measured using nanoindentation and high temperature nanoindentation.

Consistent increases in hardness and decreases in elastic modulus were seen across all material types, under all irradiation conditions when tested at room temperature. In a direct sintered sample the largest increase in hardness and smallest decrease in modulus was seen under the high dose, high temperature condition, with the smallest increase in hardness and largest decrease in elastic modulus seen after the low temperature, low dose implantation. The neon implantation and silicon implantation under the same conditions showed almost identical changes in the direct sintered material. In the fabricated materials, the composite sample produced with 5%wt sintering agent was the most consistent across all irradiation conditions, while the 10%wt composite sample exhibited the largest increase in hardness of $\sim 30\%$ in the high dose, low temperature condition, the 10%wt monolithic sample showed the largest reduction in modulus of $\sim 19\%$ under the same condition. Distinct changes in optical properties were seen under all irradiation conditions, alongside suppression of surface fracture around indentations, and the mechanisms driving this combination of effects explored. Sub-surface indentation fracture was significant in virgin and irradiated material.

High temperature nanoindentation up to 675°C on high dose, low temperature direct sintered material showed large reduction in elastic modulus and hardness with temperature, while the percentage increase of hardness in the irradiated material was maximum at the irradiation temperature. Elastic modulus which had shown a reduction with irradiation at room temperature showed increases in comparison to the unirradiated materials at temperature. Both hardness and elastic modulus plateaued above ~ 300°C in the unimplanted material.

The direct comparison between materials, ion irradiation dose, ion irradiation temperature, and nanoindentation temperature in this work has directly addressed the absence of this in the field, especially with regards to how higher temperature observations show more realistic properties for in-service components. This in combination with the correlation of the changes in fracture behaviour and optical properties with these different experimental variables gives a much more comprehensive understanding of the changes in mechanical properties and the mechanisms behind them due to irradiation damage.

Acknowledgements

I would like to thank my supervisors, Dave Armstrong and Steve Roberts for their unfailing support and guidance. Their balance of the academic and the personal has allowed this project to succeed, despite the many bumps along the road.

I was able to take advantage of the FCDT collaborative project with a brilliant collaboration with General Atomics. I would like to thank General Atomics, Hesham Khalifa, Christian Deck, Eric Song, George Jacobsen, Kirill Shapovalov, Sarah Oswald, Bernardo Serrato and the rest of the team for their help and embracing me as part of the team.

Many thanks are due to the various members of the department and elsewhere for their support and training on all the instruments: Ian Lloyd, Laurie Walton, Gareth Hughes, Gabriella Chapman, Greg Cook, Graham Wyatt, Jenny Holter, Adrian Harris, Colin Johnston and Richard Todd. Thanks also to Nianhua Peng and the Surrey Ion Beam Center.

I must also thank the members and supporters of the PCSA 2016/2017, for all our networking and enthusiasm about the future of our science. Special thanks go to Tessa Davey for world crossing support.

Particular thanks to members of the OMG! and MFFP groups: to James Gibson, Katie Plummer, and Andy London for early training and welcoming me into the group; to Yevhen Zayachuk for early TEM work, and with Alex Leide and now Bo-Shiuan Li enlarging our SiC group ; and to Jack Haley (whom I must also thank for further TEM work) and Anna Kareer for keeping me sane these last few years.

I could not have reached the end of this project without the support of Tessa Webber, whose help has been invaluable. I must also thank my St Peter's family from across the years, especially Lucy Russell, Zoe Fletcher, Katie Fellows and Vicky Elliott. And various CSCC members for keeping me grounded and providing incredible unbiased advice, especially Laura Corner.

Finally I must thank those who I count as family: to Sam and Monique, you prove that anything is possible; to Frances, I promise I'll be a bit more normal now; to Cathy (and family) and to Richard, Zoe (and Phoebe), your support has been incredible and reminds me just how important family is; to my parents, there are no words, THANK YOU. To Tom: thank you for everything, you made all of this worth while. I love you. Now here's to the next adventure!

Glossary of Abbreviations

appm atomic parts per million.

BEI Backscattered Electron Image.

CL Cathodoluminescence spectroscopy.

CSM Continuous Stiffness Measurement.

CVD Chemical Vapour Deposition.

CVI Chemical Vapour Infiltration.

DAF Diamond Area Function.

dpa displacements per atom.

DS-SiC Direct Sintered SiC.

EBSD Electron Backscatter Diffraction.

EDX Energy Dispersive X-Ray Spectroscopy.

EPD Electrophoretic Deposition.

EPR Electron Paramagnetic Resonance spectroscopy.

FCC Face Centered Cubic.

FCI Flow Channel Insert.

FEA Finite Element Analysis.

FIB Focused Ion Beam.

FLO First Longitudinal Optical.

FTO First Transverse Optical.

HFIR High Flux Isotope Reactor.

HP-SiC Hot Pressed SiC.

IFMIF International Fusion Materials Irradiation Facility.

IPFZ Inverse pole figure z-direction.

LWR Light Water Reactor.

MCL Minority Carrier Lifetime.

MD Molecular Dynamics.

NITE Nano-powder Infiltration and Transient Eutectic-phase.

PAS Positron Annihilation Spectroscopy.

PID Proportional-Integral-Derivative.

PKA Primary Knock-on Atom.

PL Photoluminescence spectroscopy.

PQ Pattern Quality.

PyC Pyrolitic Carbon.

RBS Rutherford Backscattering Spectroscopy.

REFEL Reaction Bonded SiC.

SEI Secondary Electron Image.

SEM Scanning Electron Microscope.

SITE Slip Infiltration and Transient Eutectoid.

SRIM Stopping Range of Ions in Matter.

STEM Scanning Transmission Electron Microscope.

TEM Transmission Electron Microscope.

TEP Transient Eutectic-Phase.

TKD Transmission Kikuchi Diffraction.

TRISO Tristructural-isotropic.

XCT X-ray Computed Tomography.

XRD X-Ray Diffraction.

Contents

1 Introduction **1**

2 Literature Review **3**

2.1 Introduction . . . 3

2.2 Silicon Carbide for Fusion Applications . . . 5

2.2.1 SiC Material Properties . . . 7

2.2.2 SiC Composites and their Properties . . . 10

2.3 Irradiation Studies in Silicon Carbide . . . 13

2.3.1 Studies in Monolithic Silicon Carbide . . . 14

2.3.1.1 Studies in α-SiC . . . 14

2.3.1.2 Studies in β-SiC . . . 19

2.3.1.3 Studies in Mixed Phase Monolithic SiC forms . . . 23

2.3.1.4 Summary of Radiation Damage in Monolithic SiC . . . 26

2.3.2 Studies in Silicon Carbide Composites . . . 27

2.3.2.1 Studies of Neutron Irradiated SiC Composites . . . 27

2.3.2.2 Studies of Ion Implanted SiC Composites . . . 31

2.3.3 Comparison of different types of irradiation studies . . . 34

2.4 Nanoindentation . . . 36

2.4.1 Nanoindentation for ion irradiation studies . . . 36

2.4.2 Indentation Damage Mechanisms . . . 38

2.5 Conclusion . . . 40

2.6 Research Goals . . . 42

3 Experimental Techniques **43**

3.1 Nanoindentation . . . 43

3.2 Nanoindentation Data Analysis . . . 44

3.3 Hot Nanoindentation . . . 45

3.4 Hot Nanoindentation Data Analysis . . . 48

3.5 FIB Milling . . . 49

3.6 Ion implantation . . . 51
3.7 Damage Calculations . . . 52
3.8 Raman Spectrography . . . 56
3.9 Sample Preparation . . . 57

4 Room Temperature Studies 58
4.1 Introduction . . . 58
4.2 Material Characterisation . . . 58
4.2.1 Polytype Identification and Grain Structure Observations . . . 58
4.2.2 Nanoindentation . . . 60
4.2.3 Nanoindentation Fracture . . . 62
4.3 Silicon Ion Irradiation on commercially available materials . . . 65
4.3.1 Nanoindentation . . . 65
4.3.2 Nanoindentation Fracture . . . 67
4.3.3 Damage Characterisation . . . 69
4.4 Comparative ion irradiations into Direct Sintered SiC . . . 72
4.4.1 Nanoindentation . . . 72
4.4.2 Damage Characterisation . . . 75
4.5 Discussion . . . 77
4.6 Summary . . . 82

5 Material Fabrication and Characterisation 83
5.1 Introduction . . . 83
5.2 The TEP process . . . 83
5.2.1 Precursor powder processing . . . 84
5.2.2 Laying up process . . . 85
5.2.3 Hot pressing and removal of material . . . 85
5.3 Fabricated Materials . . . 86
5.4 Material Characterisation . . . 86
5.4.1 Post process parameters . . . 87
5.4.2 Four-Point Bend Testing . . . 91

5.5 Silicon Ion Irradiation . . . 94
5.5.1 Nanoindentation . . . 95
5.5.2 Fracture . . . 99
5.6 Discussion . . . 102
5.7 Summary . . . 104

6 Hot Nanoindentation Studies 106
6.1 Introduction . . . 106
6.2 Methods . . . 106
6.2.1 Calibration Methods . . . 106
6.2.2 Thermal Drift and Thermal Matching . . . 109
6.2.3 Data collection and selection . . . 111
6.3 Results . . . 112
6.3.1 Size Effects . . . 113
6.3.2 Bulk Properties . . . 117
6.3.3 Fracture Behaviour . . . 120
6.3.4 Recovery Mechanisms . . . 122
6.4 Discussion . . . 123
6.5 Summary . . . 127

7 Summary, Conclusions and Future Work 129
7.1 Summary . . . 129
7.2 Conclusions . . . 133
7.3 Future Work . . . 134

References 136

Chapter 1

Introduction

Fusion power is seen by many as the solution to the worlds future energy supply because it is seen as a clean, safe, renewable energy source. Current estimates put the increase of energy demand by 2040 at over 25%, although without continued advances in energy efficiency the demand could be double that [1]. If we continue to rely on the quickly depleting fossil fuels of the past, such increases in energy consumption will be both difficult to sustain and destructive to our planet by increasing carbon dioxide emissions and accelerating climate change.

The UN Secretary-General, Ban Ki-moon remarked at the Council on Foreign Relations in February 2013 :

> 'We must limit global temperature rise to 2 degrees. We are far from there, and even that is enough to cause dire consequences. If we continue along the current path, we are close to a 6 degree increase.' [2]

Now this target has been reduced to only 1.5°C, more research has shown how adverse change will be occurring by the time a 1.5°C change has occurred, and limiting to this will help create a more sustanable and equitable society [3]. The hope is to have zero net CO_2 emissions by 2050 [3].

Across the world there is a desire for a change in the way we produce our energy. In 2014 nuclear output grew by an above average 1.8% and renewable energy production reached a record high contributing to 3% of the total world energy production [4]. It is now predicted that renewable energy is likely to be the primary source of energy by 2040, with more cost effective renewables being developed [5]. Renewable energy sources, like wind power or solar power, are inherently intermittent in their energy production [6]: the power market needs a reliable source of energy which these forms cannot provide without developments of energy storage technology [3, 7].

Nuclear fission output remains high across the world, despite recent big accidents like that at Fukushima where there was a total radioactive release of around 940 PBq [8]. Such accidents are a stark reminder of the dangers associated with nuclear fission energy production. It is

due to the dangers of fission that their power production costs are high, both monetarily and potentially environmentally. Currently however, nuclear fission is seen as the most affordable low-carbon producing form of producing electricity [9]. The deployment pace of nuclear fission is vastly constrained by social acceptability, where concern over the risk of such accidents as Fukushima and Chernobyl as well as dealing with radioactive waste management are forefront in the public's mind despite the comparative health risk of nuclear fission against other energy types being low per unit of energy [7].

A nuclear fusion reactor would be both low-carbon and free from the radioactivity dangers posed by fission reactors. Fusion power could have the potential to be a more reliable renewable energy source. The IPCC (International Panel on Climate Change) talk about the need for non-CO_2 emitting technologies, and fusion has the potential to help in a society ever more concerned with environmental issues. At the moment fusion power is not near term, but research into the science behind the various physical and engineering aspects will allow technological innovation to occur and has the potential to be world changing.

This thesis will investigate mechanical properties of various types of silicon carbide, after irradiations have taken place, to help investigate and evaluate behaviours and the suitability of different forms for different fusion applications. Silicon carbide is seen as a suitable structural material in many technologically advanced designs of demonstrator fusion reactors, although it is only recently transitioning from an experimental to a truly engineering material [10].

Chapter 2

Literature Review

2.1 Introduction

For fusion to be a realistic near term goal many design aspects still need to be finalised, particularly relating to the structural engineering materials, as they need to be suitable for the extreme fusion environment. With temperatures in some locations in the tokamak predicted to be more than 1000°C, due to the large amount of energy released from the fusion reaction, mechanical stability at high temperatures is clearly a concern. It is the radiation damage which is the largest challenge to understand, especially in combination with these high temperatures.

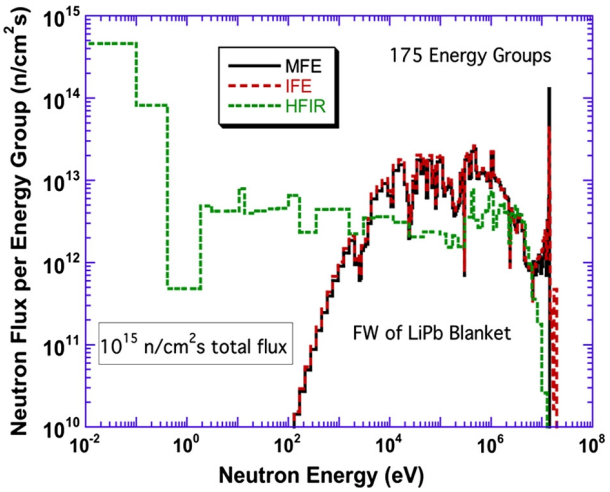


Figure 2.1: Neutron spectra at the first wall in a magnetic confinement fusion plant (MFE) and internal confinemtnet fusion plant (IFE) compared to the HFIR fission spectra. Taken from Sawan et al 2013 [11]

Current fusion designs involve a deuterium-tritium (D-T) reaction as its energy source resulting in 14.1MeV neutrons, which cannot be directed away from the containing structure [11]. In a demonstration reactor we would expect neutron loading on the walls of up to 3MW/m^2 [12]. It is understanding the effects of this type of bombardment which is most important in the development of a future power plant design. This is problematic, as the only way of creating suitable testing conditions is with a fusion source, and no fusion source yet exists, and the International Fusion Materials Irradiation Facility (IFMIF) is still not finished. Instead other methods are being used to investigate effects of radiation damage on materials. The first method is by using non-fusion energy neutrons, the second is by using ion implantations.

Non-fusion neutrons used are fission neutrons like those produced at the High Flux Isotope Reactor (HFIR) at the Oak Ridge National Lab. The problem is that fission neutrons have a

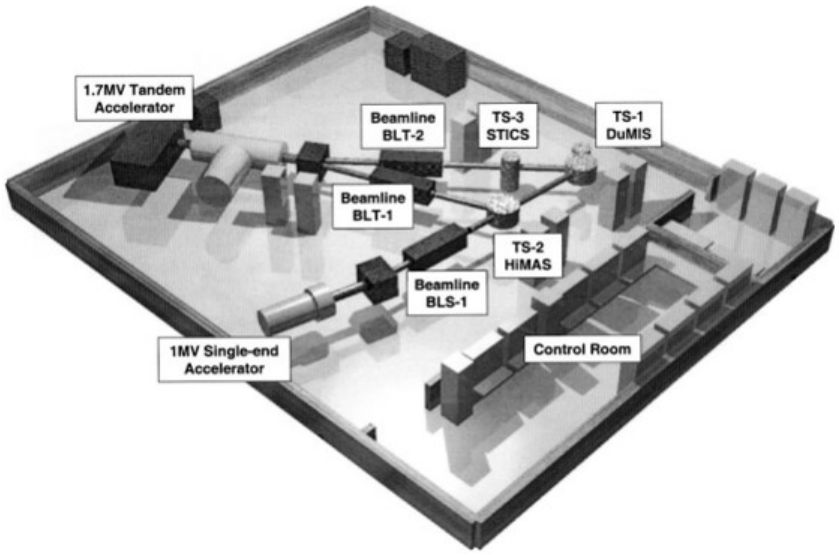


Figure 2.2: An illustration of the DuET facility set-up. Taken from Kohyama et al 2000 [14]

different neutron energy spectra to the fusion energy spectra as shown in Figure 2.1. This results in lower damage levels than would be seen in a fusion power plant. It does give the neutral particle input at energies high enough to begin cascades of damage, however the rate of damage production and the rate of transmutations will be different to those expected from the fusion neutron spectrum. The neutron cross-section of each element responds differently with some neutron capture easier at lower energies [13] resulting in very different damage accumulation. Other artificial neutron sources are also available, although these facilities have neutrons with energies < 0.1MeV or very low fluxes which again produce damage structures dissimilar to fusion neutrons.

The other method used to investigate radiation damage is ion implantations. Heavy ions at energies less than a neutron simulate some of the effects of a neutron by acting as a Primary Knock-on Atom (PKA) within the lattice: where a neutron bombardment would knock an atom off its lattice site initiating a cascade of different atoms being displaced from their initial lattice site, the heavy ion acts in the same way as the initial atom having been knocked off. It is also possible to implant with potential transmutation elements, and with light ions like helium, another waste product from the fusion reaction, as well as being produced as a waste product in trasmutations. This method is seen as a much quicker and cheaper way of simulating damage within materials than that of the long fission neutron campaigns. An example of an ion implantation facility is DuET, which is a multi-beam materials interaction facility at Kyoto

University [14], and an illustation of this facility set up is shown in Figure 2.2. Damage induced by ion implantation is at much higher dose rates of order 1×10^{-3}dpa/s [15] compared to dose rates of around 1×10^{-7} dpa/s in HFIR [16]. The dose rate can be seen to effect the amount and type of damage in a material, so this must be taken into account when looking at these types of studies, although it is often not included in the descriptions of radiation studies.

2.2 Silicon Carbide for Fusion Applications

One of the biggest unanswered questions remaining in fusion power production is an engineering one: how can a power plant which can withstand the environment the fusion plasma produces be built? With this in mind many traditional engineering materials are ruled out due to their high activation elements, or low heat tolerances. Silicon carbide is being used in many varied non-nuclear applications, from ceramic composite armour [17] to high performance car disc brakes [18] and electronic devices [19,20] to uses in jet engines [21] and optics for space telescopes [22]. In these uses it has demonstrated high temperature strength, creep resistance, oxidation resistance, radiation tolerance, chemical and mechanical stability [23, 24]. It is these properties along with it's low neutron cross section which prove its suitability as a nuclear material.

In designing a fusion power plant it is imperative to look at the safety concerns, and have designs which reduce the risks of both prompt and latent radioactive release during an accident, during maintenance, and especially activity levels post shut-down. Given these requirements the only materials suitable for being used within the first wall as defined by Eurofusion are C, Si, Fe, V, Cr, W and Ta. A silicon carbide composite in the blanket would have the lowest activation levels of these elements, with levels being below the 10 mSv/hr level for remote handling within an hour of shut-down, and below the 0.025 mSv/hr hands on limit within 10 days of shut-down [25]. This is clearly an advantage over Tungsten, the current favoured material and the material being used for divertors in ITER, which would take 2 months to cool down enough for even remote access in the plasma chamber.

Currently various forms of silicon carbide and silicon carbide composites are being considered for use in the EU's TAURO, the USA's ARIES-ACT [27] and the Japanese DREAM magnetic confinement power plant designs [28] as well as the USA's HAPL internal confinement power plant design [11], especially in lithium breeder blanket models. In addition to this, various forms

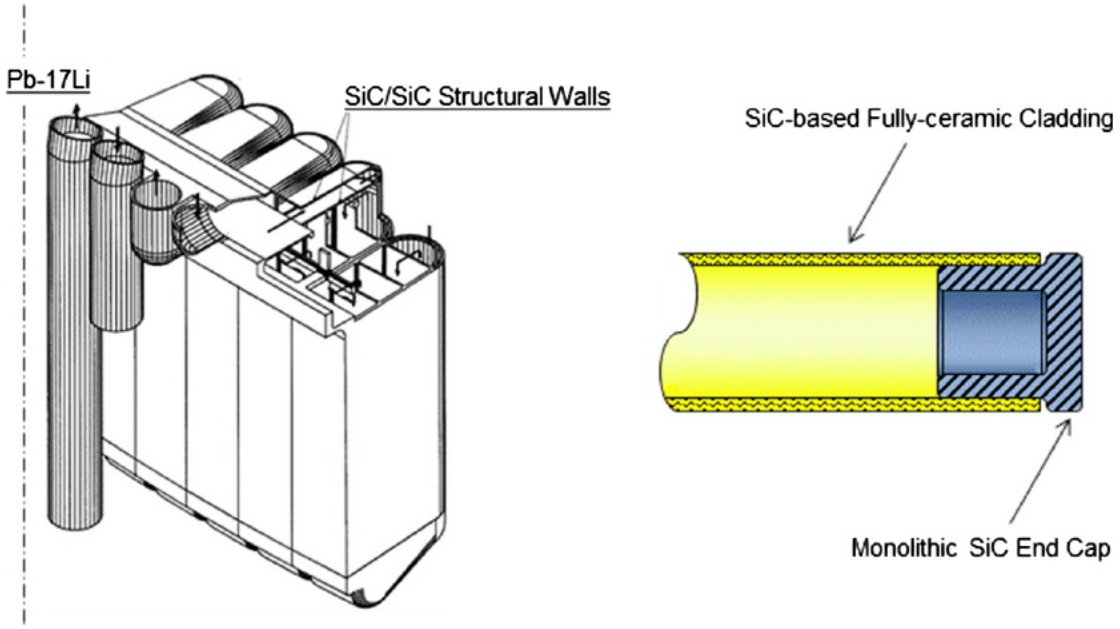


Figure 2.3: A concept scematic of a TAURO blanket desgin (left) and the end plug section for a LWR fuel rod (right). Taken from Katoh et al 2014 [26]

of silicon carbide are being designed for other nuclear applications: in fission namely TRISO coatings [29] and Light Water Reactor (LWR) fuel rods [26]; and for use in IFMIF as a heating component for the high flux test module [30]. Figure 2.3(lhs) shows a schematic of a concept design for the Pb/Li breeder blanket design for TAURO, which is also similar to designs in DREAM and ARIES-AT, giving an idea about the geometries required for these designs, mainly cylindrical or slightly squared cylinders, with more complex designs around the liquid Pb/Li cooling systems [32]. An example of a recent design is shown in Figure 2.4 [31] with the Flow Channel Insert (FCI) being made out of SiC; the FCI is required as an insulator in higher temperature designs to isolate the metallic wall from the liquid breeder and protect it from corrosion. Figure 2.3 (rhs) also shows a design for a LWR fuel rod design using SiC technologies, giving a good representation of the different proposed uses of SiC

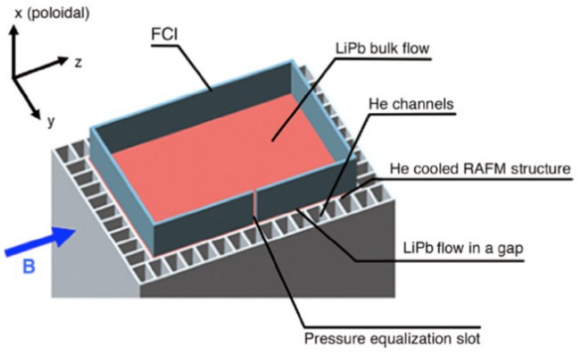


Figure 2.4: Schematics of the poloidal DCLL duct with a SiC FCI and helium-cooled structure. The FCI sits loosely inside the RAFM duct forming a thin gap with the duct walls. Both the gap and the space inside the FCI have the flowing LiPb breeder/coolant. The FCI may have a pressure equalization slot or holes. Taken from Konishi 2017 [31]

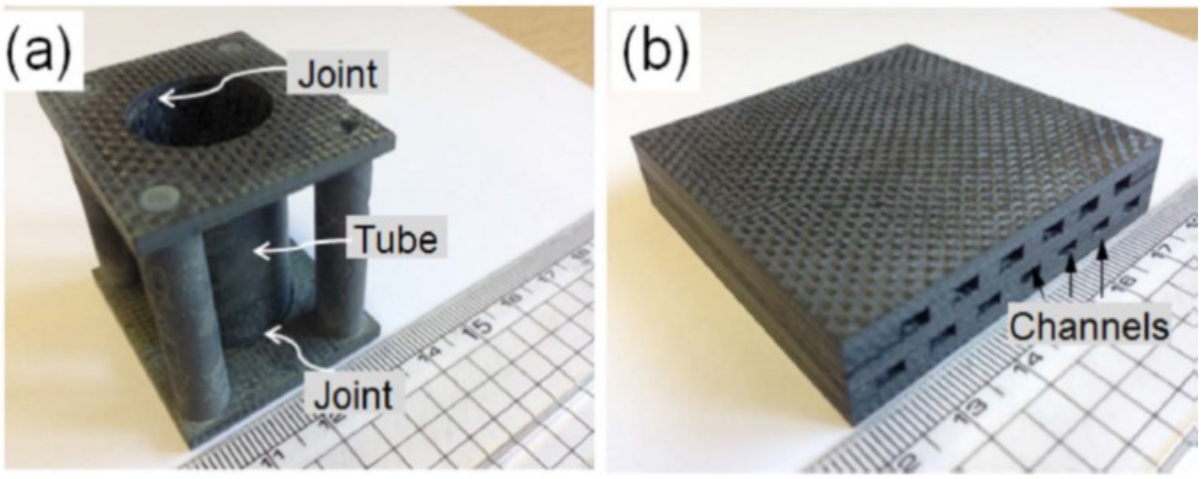


Figure 2.5: Complex assemblies produced by joining: (a) tube-flat and (b) flat-flat SiC/SiC. Channels in the dual layer multi-channel structure are marked by arrows. Taken from Sharma 2017 [36]

and SiC composites. Some of these designs are nearer term than others, SiC is already being used for fission Tristructural-isotropic (TRISO) fuel cladding [33], but looking at the fusion technologies, the FCI designs and technologies are much closer to term than ideas using SiC as a first wall or blanket component concepts, where SiC becomes structural like those seen in Figure 2.3 [23, 32, 34]. The advances being made using SiC/SiC for fission purposes, especially fuel cladding, is helping with fusion designs [10], where long thin tubes of nuclear grade material are now easily being produced [35]. An example of a more complex SiC/SiC architecture is shown in Figure 2.5, where fission-like designs were used for proof of concept [36].

Given the complex design requirements for any SiC component, both with their intrinsic mechanical and thermodynamic properties and with their geometry design requirements, it is even more important to understand the underlying material properties and the effects of radiation damage on these properties. Without this fundamental understanding the development of nuclear grade materials becomes even harder, and understanding why the harsh fusion environment effects the intrinsic properties becomes impossible.

2.2.1 SiC Material Properties

Silicon carbide's basic properties are very difficult to define, as the many different phases and production methods are seen to greatly alter its intrinsic properties. SiC was first discovered synthetically, however it can be found as a naturally occurring ceramic and was given the name

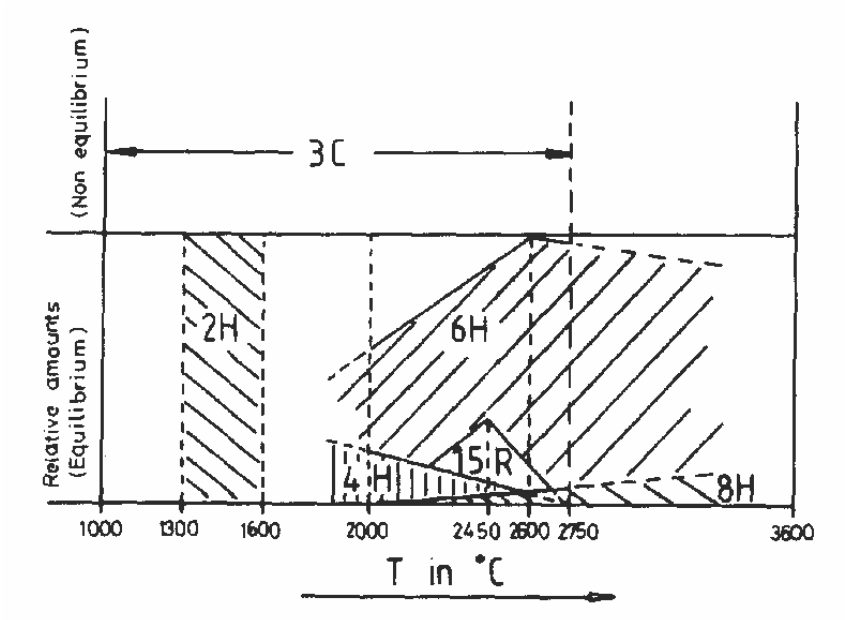


Figure 2.6: Phase stability diagram of SiC polytypes. Taken from Jepps 1983 [39]

moissanite, after H. Moissan who found the first naturally occurring SiC in the Canyon Diablo meteorite in 1904 [37]. The majority of naturally occurring SiC has been extra-terrestrial in origin, as it is incredibly rare on earth (but abundant in space) it is generally seen as a synthetic material [38]. SiC is fundamentally a strongly covalent material with all SiC polytpes being covalently bonded primary co-ordination tetrahedra, but it is also a slightly ionic material due to the differential eletronegativity between the Si and C atoms, making it a material suitable for electronic devices as well [29]. In a single crystal form it is commonly spilt into generalised hexagonal and rhombic forms as α-SiC or it's single cubic form β-SiC. The cubic 3C-SiC is the only sequence that shows cubic symmetry, and all other polytypes are classed as α SiC [29], although 6H-SiC is the most prevalent hexagonal form. An accepted phase stability diagram is shown in Figure 2.6 [39]. The stability of any of these forms of SiC is generally seen to be very dependant on temperature, with 6H-SiC seen to be the most stable across the widest temperature range of the α-SiC polytypes. While 3C-SiC is found to be stable up to 2373K, just below the decomposition temperature of 2818K [29] some studies deem 6H-SiC to be more stable as phase transformations in 3C-SiC can easily be triggered under deformation [40].

The fabrication of SiC is again something which can greatly affect it's intrinsic and extrinsic properties. There are various fabrication methods currently used for the synthesis of SiC, ranging from more traditional techniques like the direct conversion method of Reaction Bonded

SiC (REFEL) [41], through various sintering methods and hot pressing methods to more modern methods like Chemical Vapour Deposition (CVD) [29] and Nano-powder Infiltration and Transient Eutectic-phase (NITE) processes [42], as well as varied nano-engineering methods. Many of the more traditional forms of SiC production form materials inherently unsuitable for nuclear applications due to sintering additives, residual silicon and high levels of porosity. The CVD method is most commonly investigated for potential nuclear applications due to its low temperature production without the need for any sintering aids as well as its production of inherently pure, stoichiometric and highly crystalline material [29], however it is slow and relatively expensive to produce.

A comprehensive analysis of the different material properties of the various forms of SiC are given in Snead's 2007 handbook [29], which is itself heavily cited in the literature. All SiC fabrication methods and polytypes are seen to be stable to 2545 ± 40°C [29] with theoretical densities at room temperature of 3.215g.cm^3 for the most common polytypes. No significant differences have been seen between hot pressed, sintered and CVD materials or α and β polytypes when looking at their elastic moduli, where $E_0 \approx 460$GPa at room temperature, however variations in elastic moduli are likley to be seen at elevated temperatures [29]. An example of sintered α-SiC from Munro's 1997 study shows a reduction in elastic modulus from $415GPa \pm 3\%$ at room temperature to $392GPa$ at 1000°C and to $380GPa$ at 1500°C calculated from resonance techniques [43]. Values of Poisson's ratio are seen to vary between $0.14 - 0.24$ [29, 44]. Differences between fabrication methods can be seen with hardness values, which nominally vary between $20 - 30$GPa with outliers to those values being mainly due to excessive sintering agents, or free carbon or silicon within a given material [29]. Fracture toughness values for different forms of SiC do not seem to vary widely between material types, with $K_{IC} = 2.8\text{MPa}\sqrt{m}$ being quoted for both α-SiC and β-SiC, where increases in fracture toughness are seen with increasing temperature, however β-SiC shows a much greater increase than α-SiC [45], despite this there are variations in quoted values for fracture toughness measurements depending on the experiment and method of calculation with room temperature values often up to $K_{IC} = 3.3\text{MPa}\sqrt{m}$ [45–53]. From these basic understandings of the monolithic forms of SiC it is clear that the purest forms of SiC, with a highly crystalline and stoichiometric structure are likely to be best for transferring to nuclear applications, and these specifically are produced by the CVD method, although

the author believes that material from the NITE process may also be a likely candidate, if the sintering aids in these materials can be tailored for damage tolerance, or the materials are used further away from the first wall.

2.2.2 SiC Composites and their Properties

The suggestion to use SiC/SiC composites rather than any monolithic form of SiC seems to have initially come about in an attempt to ensure a stronger material by arresting cracks or deflecting cracks at the matrix or interphase in an otherwise very brittle material, cracks which would otherwise lead to catastrophic failure [54]. This would be mitigated by producing an advanced composite which would incorporate high strength whiskers, platelets or fibres into a fully ceramic matrix [55]. In addition it was thought that deterministic design approaches would be possible due to the hoped for increase in toughness because of the reinforcement with strong fibres [56].

SiC composites proposed for nuclear applications are formed from continuous fibres with an interphase layer between the fibres and a fully densified SiC matrix [57]. The basis for all of these composites are the fibres themselves, and these have already been through design improvements to make them more suitable for nuclear applications. Initial work on SiC fibres produced Nicalon^{TM} and Tyranno Fibre^{TM}, which were produced by low temperature melt spinning of the polycarbosilane (PCS) or polytitanocarbosilane (PTCS) polymer which was then cured at high temperature by either exposure to oxygen or through electron beam curing [57]. This process produced cheap fibres with good mechanical properties and excellent weavability, however they are not purely SiC fibres, due to the oxygen involved in the process. These fibres resulted with 65% SiC content along with 23% O and 11% C [57, 58]. This was not acceptable for a nuclear material so a second generation of fibres called Hi-Nicalon^{TM} were produced, now with a relative oxygen content of below 1%, however these fibres were still nanocrystalline SiC within a C continuum. As discussed in Section 2.2.1, a highly crystalline and stoichiometric material is likely to be best for radiation tolerance. Further work was then done, producing Gen III fibres thought to be more suitable. These commercially available Gen III fibres are: Hi-Nicalon^{TM} Type S; Tyranno SA3; Sylramic^{TM} and; CefNITE^{TM}. Irradiation studies using both Gen II and Gen III materials are discussed in Section 2.3.2. These Gen III fibres are near

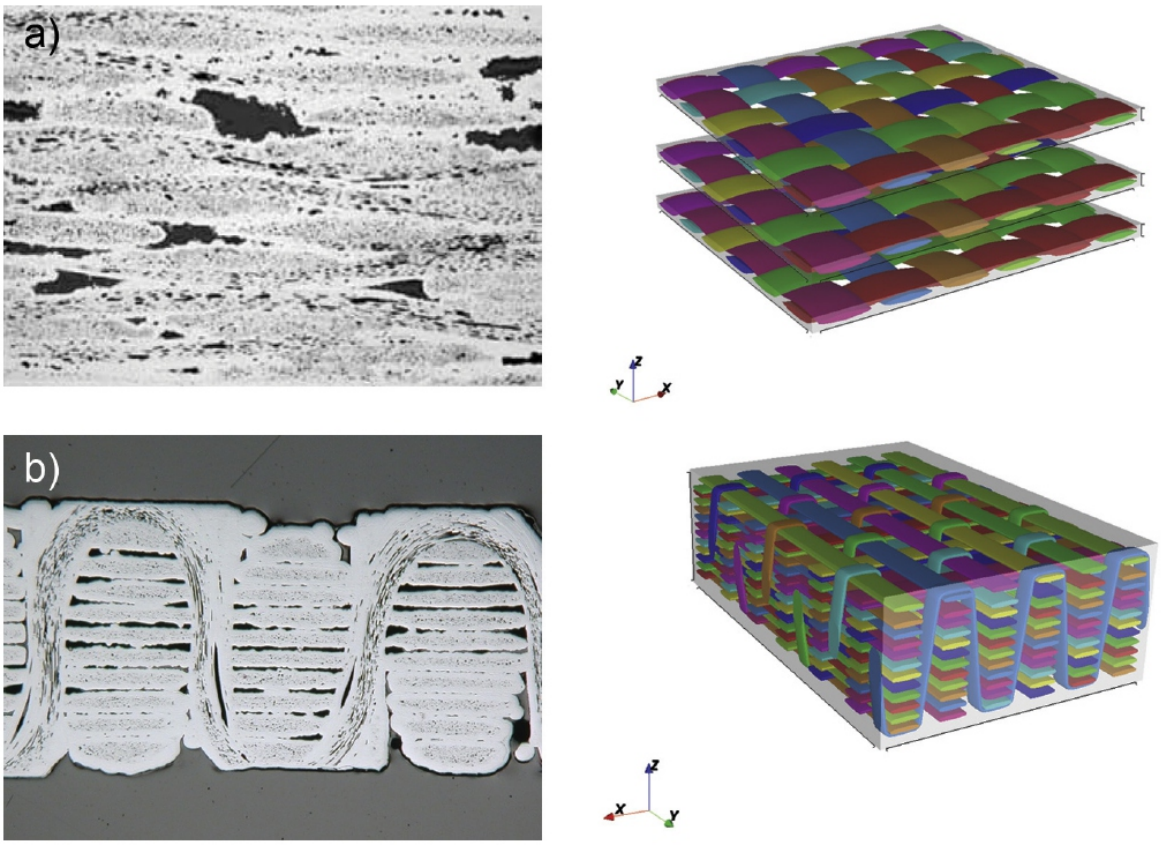


Figure 2.7: Optical micrograph of (a) a stack of 2D fabrics and (b) a 3D orthogonal woven reinforcement architecture densified by CVI and the corresponding model of the reinforcing fibre structure. Taken from Ivekovic et al 2013 [24]

stoichiometric, with even lower oxygen content and are crystalline, however they are sintered in a high temperature process [57].

Having produced these fibres, composites of either a 2D or 3D woven structure are produced, where examples of a composite can be seen in Figure 2.7. To create this composite an interphase is needed which creates an adequate fibre-matrix load transfer, and prevents de-bonding and sliding. These interphase layers can be either single layered, or multi-layered and are applied to the fibres before matrix densification. These layers tend to be either Pyrolitic Carbon (PyC) or boron nitride (BN), or a combination of these with SiC. It is fully expected that the PyC is a better solution, as additive BN is likely to have an even more adverse reaction to irradiation due to its large neutron cross section. Although carbon is also well known to have problems with radiation [57], BN could not be used in a situation where neutron capture is needed in the breeder material, leaving PyC as the better option.

Densification is then performed by adding a matrix material, normally of Chemical Vapour

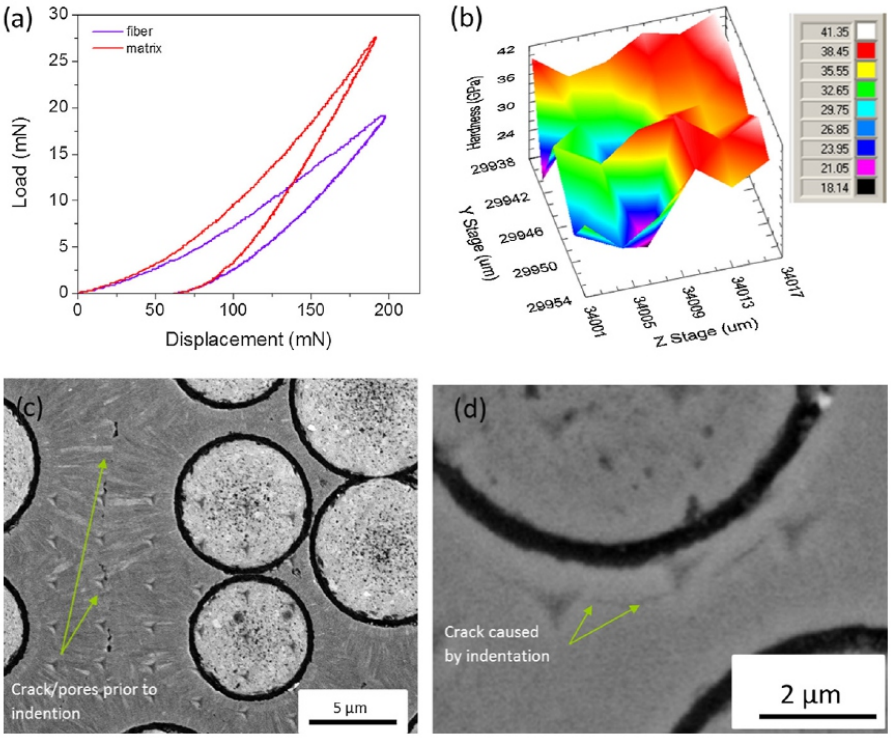


Figure 2.8: (a) Typical load displacement curves obtained from composite made with Tyranno SA3 fibres and densified using the CVI method , (b) 3D plot of the hardness values on this particular fibre and (c) SEM image after indentation. (d) SEM image after indentation for another fibre in the composite. Taken from Frazer et al 2015 [61]

Infiltration (CVI) (equivalent to the monolithic CVD process) or through the NITE or Transient Eutectic-Phase (TEP) process [23]. Other methods have also been used at this stage like a hot press sintering process [59] or a more advance NITE process the Slip Infiltration and Transient Eutectoid (SITE) process [60]. Advances and developments are ongoing including recent developments of Electrophoretic Deposition (EPD) [36]. In the same way as previously discussed it is desirable that this matrix be both stoichiometric and crystalline, and be made predominantly with a single phase, β-SiC.

The majority of tests on these composite materials have been performed to look at their radiation tolerance as discussed in Section 2.3.2, however a study by Frazer et al [61] was able to look at the localised properties of two different composites made with Tyranno SA3 and densified using the CVI method. They utilised micro-mechanical testing techniques to test the individual components in the composite, and showed the fibre was considerably softer than the matrix as shown in Figure 2.8. Work like this enables finer tuning of the composite design due to localised knowledge of areas of weakness within the material. In addition to

this work characterisation studies have been performed to look at some distinctive SiC/SiC architectures, which concluded that due to the complex nature of these materials, development of new characterisation techniques will be necessary in order to understand these materials throughout their active lives [62]. Another growing area of research is into joining techniques and their radiation resistance as required for the production of complex architectures [63, 64]. Examples of such architectures for fission designs are shown in Figure 2.5.

2.3 Irradiation Studies in Silicon Carbide

Over the last sixty years, since the first suggestions were made about silicon carbide's potential suitability for nuclear applications, many irradiation studies have been performed with the aim of looking into it's radiation damage tolerances. Despite this there is much work to be done in understanding the physical foundations and processes of radiation damage in silicon carbide needed to be able to have a comprehensive understanding of the design limiting phenomena [23].

Various radiation studies have been performed: ranging from low energy neutron irradiations, to very high energy ion implantation experiments. Early work by Price [65] began by looking at pyrolytic silicon carbide with fast neutron irradiations, where fast neutrons are anything over 0.1MeV [66]. These fast neutrons were orders of magnitude less than fusion neutrons, at $E > 0.18MeV$, with relatively low doses of $2.0 - 4.2 \times 10^{21} ncm^{-2}$. Most modern work has neutron doses over 0.5 displacements per atom (dpa), with some up to over 70dpa where we consider a neutron dose of $1 \times 10^{25} nm^{-2}$ to represent about 1dpa.

In looking at these various irradiation studies, the vast array of variables becomes very clear, with each experiment looking at different materials, with different types of irradiation, at different fluences, and dose rates, and at different temperatures. Each of these variables is seen to affect the type and level of damage seen within the material, and it is understanding how each variable individually and combined affects the levels of damage which is vitally important. The literature is split primarily by material type before looking at any similarities which may exist between them. With the many various lattice types seen in forms of SiC, they can be divided into a few main categories. The hexagonal forms of α-SiC, the cubic forms of β-SiC, other monolithic and mixed forms of SiC, SiC fibres and SiC/SiC composites.

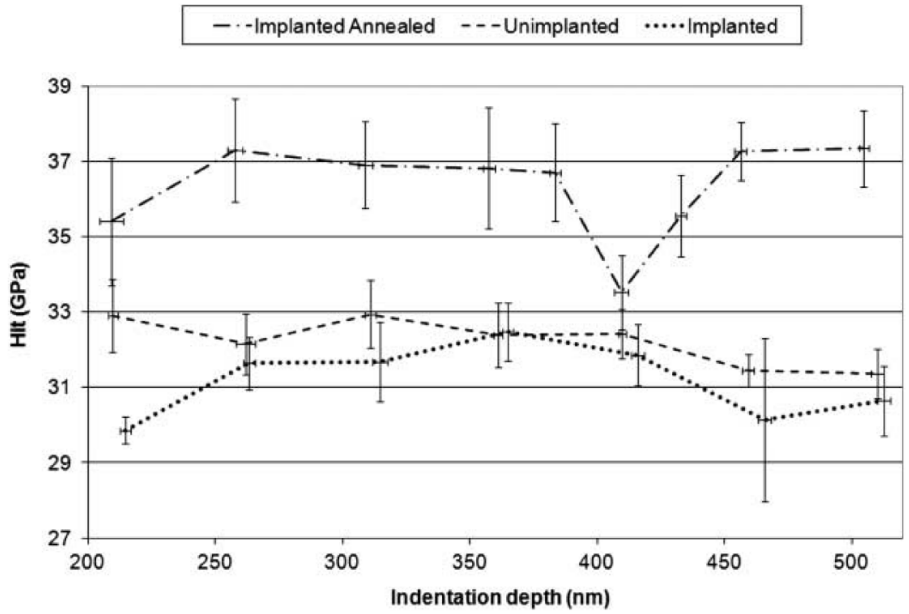


Figure 2.9: Plot of the depth-resolved nanoindentation hardness measurements (Hit) obtained for the implanted and virgin 6H-SiC showing a significant reduction in hardness in the damaged region for the annealed specimen. Taken from O'Connell et al 2012 [67]

2.3.1 Studies in Monolithic Silicon Carbide

2.3.1.1 Studies in α-SiC

The majority of studies in α-SiC are on 6H-SiC and are He implantation studies, often in room temperature conditions with relatively low implantation energies. Multiple publications over the last few years have expanded to slightly higher energies and temperatures, although the focus is shifting slowly as better technology becomes available. There is a clear problem with low energy, low temperature studies as it is well known that implantation temperature and energy makes a large difference in the levels and types of damage seen in the material. These studies do however highlight some of the issues which need to be taken into account, mainly effects of He within the SiC lattice, and not mechanical properties. As He will be present in materials around a fusion reaction both from plasma exhaust and transmutations within the bulk material, especially when carbon decomposes to 3He, different energy He atoms will be present, so these lower energy studies show some of the effects which will contribute to the whole damage profile.

O'Connell's 2012 study looks at the effects of post irradiation annealing [67], as does Shen's 2017 study [68]. Both look at implantations into single crystal 6H-SiC: O'connell's study with

100 keV He ions to a fluence of 1×10^{17} ions/cm^2 at an elevated temperature of $200 - 300$°C; and Shen's study with 400keV ions, to the same fluence but at 400°C. Both studies investigated the effects of annealing post irradiation. O'Connell saw no change in nanohardness, but when annealed post irradiation showed an increase in hardness of 37GPa through the bulk, with a sudden drop in hardness across the peak damage region as shown in Figure 2.9. The hardening effects are thought to be due to the coalescence of point defects during the annealing process preventing atomic plane slipping. The post irradiation annealing was observed to bring out the defects within the lattice, with the high temperature annealing condition at 1000°C giving the He within the lattice sufficient migration energy to properly form He bubbles. Shen's later study looked at the annealling effects in more detail, across a range of durations and at temperatures ranging from $600 - 1400$°C, and showed that evolution of bubble size and development was significantly effected by both annealing temperature and duration. Further investigation of damage in He irradiated material by Han et al 2018 [69] shows that He bubbles are preferentially growing on grain boundaries after an implantation at 1000°C to 0.5dpa. They also observed the preferential growth of loops onto interstitial stacking faults.

The study of radiation induced amorphisation has been performed across multiple types of SiC, although understanding at what threshold it occurs is seemingly very difficult. In Sasase et al's study on a high energy He implantation into α-SiC, no amorphisation was seen, where they had expected it [70], concluding the threshold for amorphisation alters with the energy of the He implantation. In Leclerc et al's study however they saw that the threshold energy density for full amorphisation was $6 - 7 \times 10^{21}$keV/cm^3 after a $1.6MeV$ He implantation [71]. The lack of amorphisation in Sasase et al's study with an implantation of $3MeV$ He to a fluence of 1×10^{17}ions/cm^2 is difficult to reconcile with Leclerc's lower energy study, the lack of a reported implantation temperature could also be an issue, as could dose rate or other variables not discussed in these papers. Further to this, despite these two studies being directly compared in Leclerc's work they both investigate different forms of α-SiC: where Sasase's work is with 6H-SiC, Leclerc's is with 4H-SiC. In this situation it is impossible to tell which change in condition causes amorphisation to occur in one study and not in the other. Additionally O'Connell et al's study was below this threshold energy, and yet saw no amorphisation [67]: it is suggested that in-situ heating during the implantation caused some annealing to take place

re-crystallising the samples, but again it is difficult to conclusively say this is the reason for the lack of amorphisation here, and here implantations were performed at elevated temperatures, whereas Sasase's study was at room temperature. Further studies by Harrison et al 2018 [72] report complete amorphisation from another room temperature He implantation to a quoted at 1.5dpa, this time with an implantation energy of only $20keV$, and is attributed to the lack of interstitial mobility at this temperature. With the vast range of energy implantation used between these studies it is no wonder that an amorphisation threshold is different in each study. Harrison et al's study looks into a wide range of implantation conditions from room temperature to 1200°C and doses up to 5.0dpa and is again on 4H-SiC. They saw a decrease in He bubble nucleation dose from 2.0dpa at 400°C to 0.5dpa at 1200°C. They were also able to conclude that at the highest temperature helium platelets were forming between Basal planes, in contrast to the grain boundary growth seen by Han et al [69].

Looking at neutron irradiation studies in α-SiC, Snead et al 1999 again showed clear amorphisation, and with this amorphisation a reduction in nanohardness from $38.7 \pm 2 - 21.0 \pm 1 GPa$ for the single crystal 6H-SiC and from $36.2 \pm 1.2 - 23.4 \pm 0.6 GPa$ for the polycrystalline sample [73]. This study was a low temperature study (implantation at 53°C) with a neutron fluence of 2.6×10^{25} corresponding to a dose of about 2.6dpa. With this reduction in nanohardness came a similar reduction in elastic moduli from $528 \pm 14 - 292 \pm 45 GPa$ for the single crystal and from $500 \pm 11 - 291 \pm 7.5 GPa$ for the polycrystalline sample. These reductions in elastic moduli are fully expected from the swelling effects seen across many different sample types. Snead et al in their later 2007 neutron irradiation experiment found a direct correlation between thermal defect resistance and the swelling of both β-SiC and α-SiC in the temperature range $200 - 800$°C with a neutron fluence of $0.01 - 4 \times 10^{25}$n/m^2 [74]. In this study they also found the swelling was minimised in the temperature range $1100 - 1200$°C. In a further 2016 study Snead et al looked across a range of neutron doses, and saw at 0.5dpa a 7.8% swelling in a still fully crystalline material, but it became amorphous by 2.0dpa and swelling was maximised at this dose with $\sim 11.7\%$ swelling plateau for higher doses. Swelling effects in α-SiC were also seen by Pramono et al, where macroscopic length increases of $0.59 - 0.74\%$ were seen with varying boron doping levels within the SiC [75]. In addition to these volumetric changes, lattice parameters were observed to have slightly anisotropic expansion. The degree to which the swelling in this

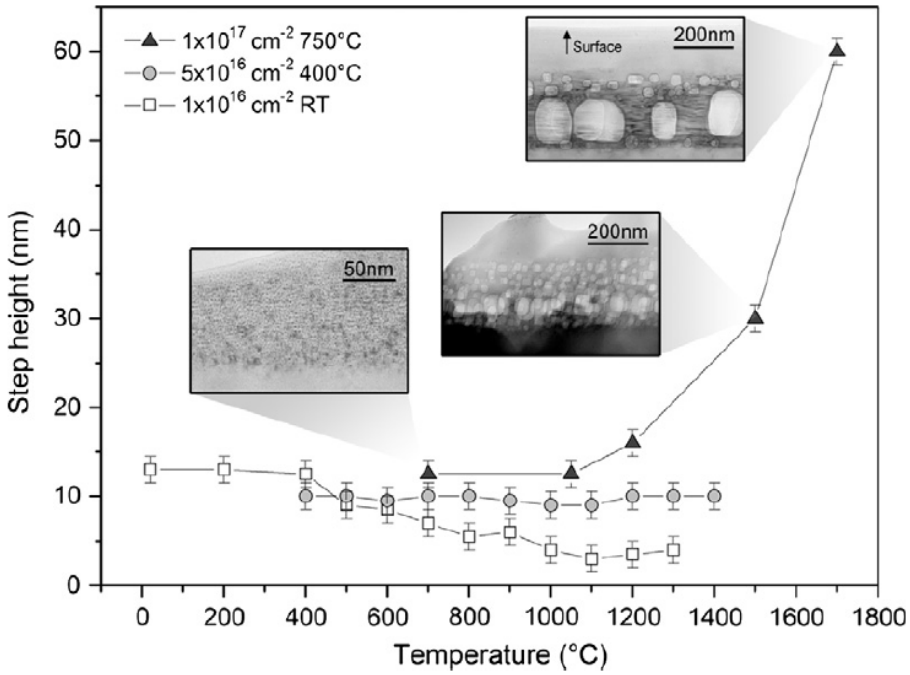


Figure 2.10: Surface swelling evolution of helium implanted 4HSiC under three different regimes by isochronal annealing with XTEM images showing the microstructure of the high regime implanted samples in the as-implanted state (750°C), and after annealing at 1500°C and 1700°C. Taken from Barbot et al 2011 [77]

study can be compared is difficult to quantify due to both the varying B concentrations, as well as the neutron irradiation being performed in a He filled capsule, to a neutron fluence of only 2.8×10^{24} (an order of magnitude less than Snead's study) at 300°C. The anisotropic swelling effects are however likely to be a general α-SiC effect, as hexagonal lattices are well known to tend to anisotropic swelling [57, 76]

A significant amount of work into the effects of various irradiation types on the swelling in SiC has been performed, and Snead et al's various studies are examples of this. In studies with 4H-SiC Barabot et al saw significant surface swelling as effect of He implantations of $50keV$ to about 2dpa [77] as shown in Figure 2.10, with this swelling appearing to be due to the formation of extended defects in the buried zone of high nuclear stopping. Interestingly they found it was partially due to the grouping together of interstitials and vacancies rather than their self-annihilation. Leclerc et al showed, with a higher implantation energy of $1.6MeV$ He, that the primary defects along the ion's path are seeming to cause lattice strains which are helping to cause swelling [71]. Some additional work focusing on the lattice damage, which is seen to cause a lot of the swelling effects in SiC, has been performed by Li et al [78] looking at

Xe implantations at various energies into 6H-SiC. They have shown that in the low dose regime the dominant effect on the lattice expansion is interstitial type point defects, and increased damage levels are seen to cause amorphisation [78]. When looking at the dose level effects on nanohardness they saw a slight increase in nanohardenss when the dose was only 0.11dpa, however when amorphisation was reached a reduction in hardness of about 45% was evident, showing similar results to Snead et al's 1999 neutron study [73].

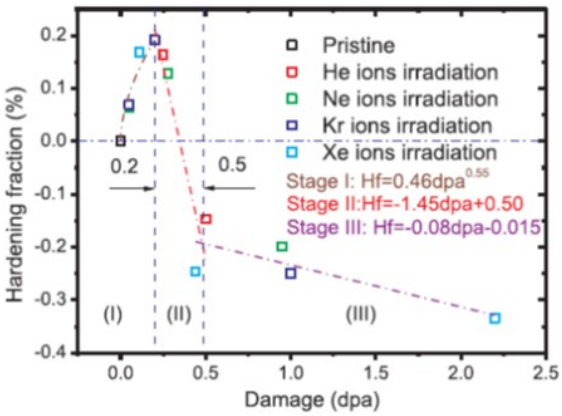


Figure 2.11: The dependence of hardening fraction of 6H-SiC on damage (dpa). Taken from Yang et al 2018 [79]

In a heavy ion study like this, with 3.3-8MeV Xe ions, investigations are made with heavier ions than are likely to be seen within a SiC material type within any reactor. Sawan et al's study looking into transmutation products in SiC lists the transmutation products as Lithium, Beryllium, Boron, Magnesium, Aluminium and Phosphorus [11]. The heaviest of these is less than a third of the atomic weight of Xenon, for this reason the ultra heavy ion studies, despite their ability to add a much larger amounts of damage quickly, are less likely to accurately simulate damage in SiC. Direct comparisons of any of these swelling studies are particularly difficult as they primarily look into the reasons for the swelling and do not give indications of the degrees of swelling seen in these α-SiC samples, and rarely look at the mechanical changes it causes. In contrast Yang et al's 2018 study [79] examines various inert ion implantations to examine the hardening fraction as seen in Figure 2.11, and showed that nanoindentation hardening depended far more on dose than on ion species, although saw different amorphisation thresholds with the different ion species. Chen et al's 2018 [80] study gives an interesting perspective on comparing neutron and self-ion implantations with nanoindentation alongside the use of Finite Element Analysis (FEA), and showed that studies at the same calculated dpa showed larger hardening effects in the self-ion implantation studies than the neutron study. They attribute this difference to ion implantation induced surface lateral stress, and in combination with FEA were able to adjust for this so the ion implantations and neutron implantations matched. Such effects should be

more widely considered when looking at ion implantations as analogies for neutron studies.

In the expansion to dual beam implantations as performed by Wang et al [81], the effects of a Si ion and He ion simultaneous implantation are seen in 6H-SiC, where they show that a simultaneous implantation leads to a higher level of damage within the material than a sequential implantation [81]. This is seen to be because the He is stabilising the defects like vacancies rather than creating further damage when implanted sequential to the heavier Si ions. They are also observing simultaneous recovery of defects in this situation due to a dynamic annealing effect of the He implantation. This dual beam experiment was performed with an 18MeV Si implantation to ~ 0.55dpa and a $2.2MeV$ He implantation to about 35appm. Wang et al's two 2018 studies [82,83] do look at two further dual beam implantations, one with Si and He, and the other with Au and He, looking further at sequential implantations and the effect on microstructure and mechanical properties. The main conclusions from both these works is that the effects are incredibly sensitive to different irradiation environments, and the different sequences of the dual implantation.

2.3.1.2 Studies in β-SiC

Similar to the studies in α-SiC, there are not a large number of studies into effects on β-SiC. Most of the studies are in polycrystalline material, predominantly made through the chemical vapour deposition method (CVD). In addition the majority of these studies are either neutron irradiations of self-ion implantation with Si, in contrast to the predominantly He implantation studies on α-SiC

One of the earliest radiation damage studies in SiC, which is still heavily referenced in the literature, is Price's 1969 work on neutron irradiation in pyrolytic SiC, where irradiations were performed to $2.0 - 4.2 \times 10^{21}$nvt at temperatures ranging from $460 - 1040$°C [65]. This early SiC study was already focusing on radiation damage in SiC leading to macroscopic swelling as already seen in the α-SiC studies. It was found that β-SiC exhibited isotropic expansion, and it was believed that an increase in lattice parameter gave rise to this. Despite the evidence of swelling in this study, no significant change to elastic modulus or modulus of rupture was evident. The degree of swelling here was also minimal with a 1% expansion at room temperature reducing to a 0.05% expansion an 1000°C. This early study is important for showing that these

swelling effects were present, but seems to have severely underestimated the levels in comparison to more recent work. The lack of any mechanical changes due to irradiation has also proved false. Much of this underestimation of effects is likely due to the relatively low doses shown here, and the advances in experimental techniques in recent decades.

Osborne et al's 1999 study also looks into neutron irradiated β-SiC [84]. They show a significant reduction in density at temperatures up to 550°C, which is seeming to plateau with neutron fluences over $1\times10^{25}nm^{-2}$, (1dpa) . They also report an initial increase in hardness with neutron damage, however this hardness effect decreases with increased neutron doses quickly reaching a plateau. The elastic modulus is however reducing with increased neutron doses, until again reaching a plateau. These hardening effects and changes to the elastic modules are very similar to those seen in the α-SiC studies.

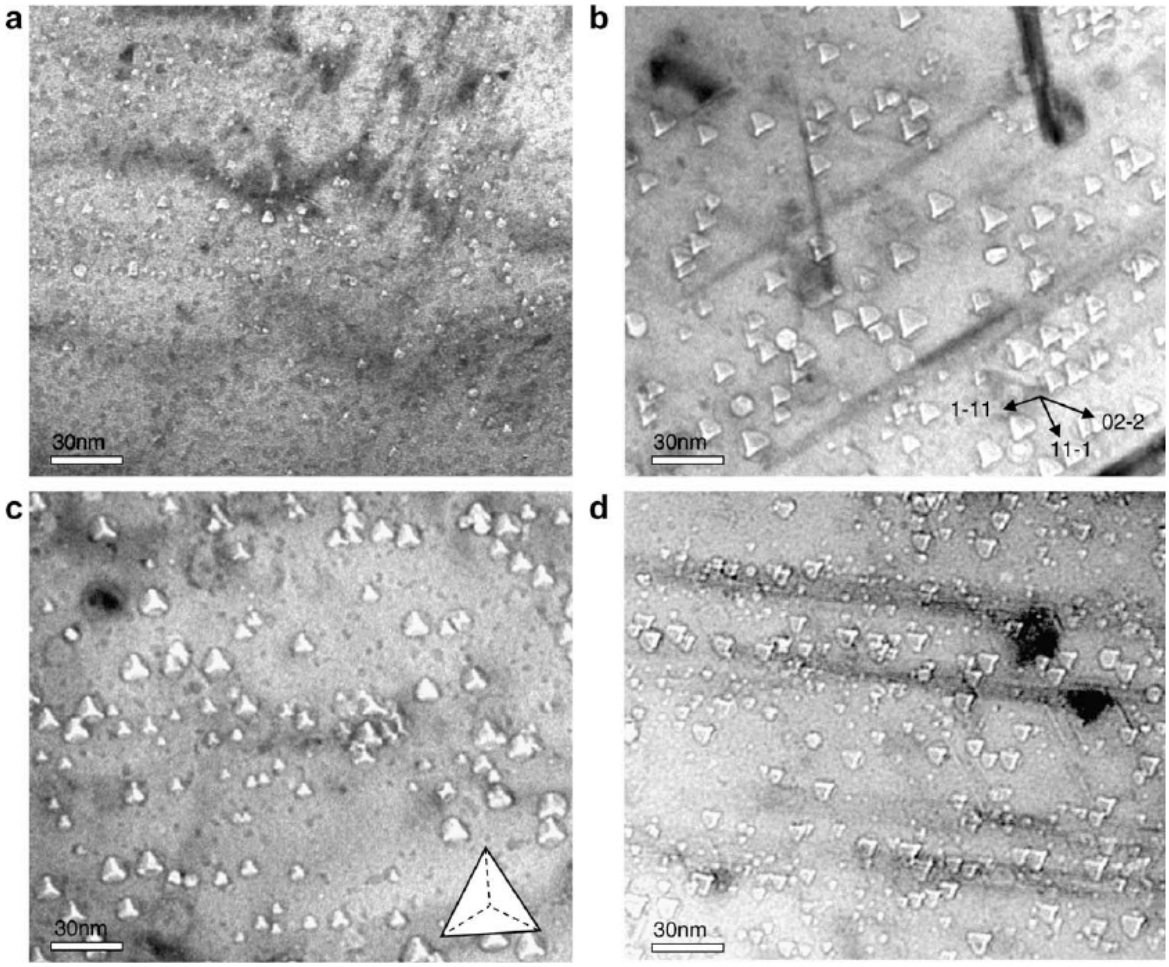


Figure 2.12: Faceted voids in β-SiC irradiated at (a) 1460°C 1.9×10^{25} n/m^2 , (b, c) 1460°C 5.8×10^{25} n/m^2 , and (d) 1460°C 9.6×10^{25} n/m^2. With the beam axis at B 0 11 for (a), (b)and (d) B 111 for (c)). Taken from Kondo et al 2008 [85]

The majority of the neutron irradiation work has been performed specifically looking at the microstructural developments and defect dynamics with irradiation. It has been reported in Katoh et al's 2006 study that defect clusters appearing as black spots and dislocation loops in TEM work are evident with irradiations at 800°C to $4.4 \times 10^{25} nm^{-2}$, and these defect clusters develop into dislocation loops with higher fluences of $7.7 \times 10^{25} nm^{-2}$ [16]. The origin of these black spots has been investigated by Yu et al 2018 [86] with Molecular Dynamics (MD) simulations, and they found that they are likely vacancy rich clusters, which they supported with Transmission Electron Microscope (TEM) studies. This work correlates well with Lin et al's 2017 study [87] which observed the similar effects in ion implanted material coming to similar conclusions about the origins of these black spot defects. In a separate study with neutron fluences ranging from $1.5 - 9.6 \times 10^{25} nm^{-2}$ dislocation loops and small spherical cavities were also seen with temperatures under 1300°C, however with temperatures up to 1460°C faceted voids were clearly visible [85] as shown in Figure 2.12. These faceted voids are very distinctive, and clearly show the Face Centered Cubic (FCC) type nature of this material with two sides parallel to the $(1\bar{1}1)$ and $(11\bar{1})$ planes, whilst the other side is parallel to the $[02\bar{2}]$ direction. These triangular shaped faceted voids show that vacancies are forming naturally in the unit cells. These triangular voids have a larger surface area than a spherical void would so the free surface energy of the faceted surfaces is much lower than that of other surfaces. This then demonstrates that these lattice planes have the lowest surface energy, allowing for stable voids to be created [85]. In addition to this it was reported that cavity formation is likely only to occur with temperatures over 1000°C due to Si vacancy migration beginning to occur at $800 - 900$°C. Faceted voids were also seen in Hu et al's 2018 study [89]

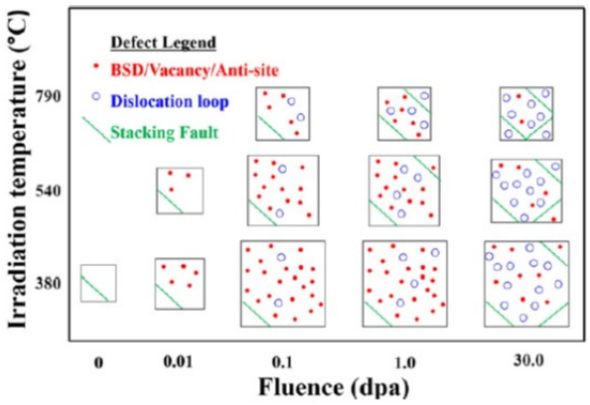


Figure 2.13: Schematic of the fluence and temperature evolution of point and line defects quantifiable from XRD analysis. The BSD/Vacancy/Anti-site defects expand the lattice and cause the XRD peaks to shift to lower two theta angles. The dislocation loops (such as interstitial loops) will cause peak broadening and therefore, the microstrain parameter to increase. The box size represents the macroscopic swelling measured by the length change using a micrometer. Taken from Sprouster et al 2017 [88]

of simultaneous He and neutron irradiation. These studies seem to concur with their findings with these microstructural developments, both in polycrystalline β-SiC. Further to these studies a temperature-dependant diffusion coefficient has shown an activation energy of interstitial migration as 1.5 ± 0.1eV, given work on the temperature-dependant width of the interstitial loop denuded zone [90]. This is despite some migration barriers associated with C interstitials being lower than $1eV$, due to the much slower-moving Si interstitials. More detail of defect developement with irradiation temperatures and doses was investigated by Sprouster et al [88,91], looking at the changes between $380 - 1180$°C and neutron doses of $0.011 - 31$dpa. The best summary of their data is shown in Figure 2.13, and brings together many of the effects seen in earlier works. The effects of these microstructural findings are however not expanded onto a larger scale to look at neutron irradiation effects on the mechanical properties of β-SiC.

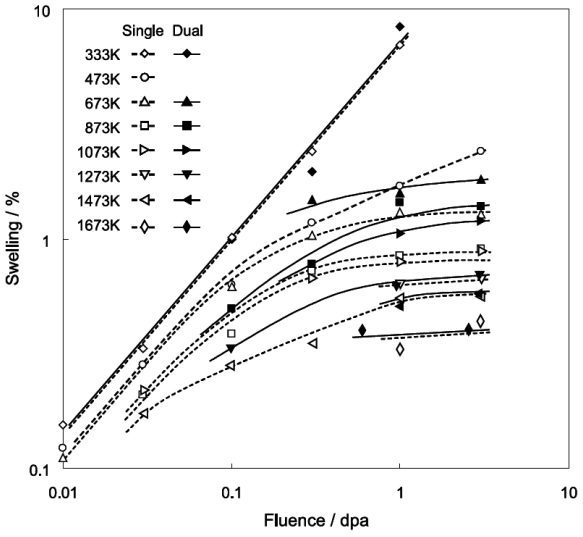


Figure 2.14: Fluence dependence of swelling in β-SiC in a low-uence regime under single- and dual-beam ion irradiation. Taken from Katoh et al 2002 [92]

Looking to heavy ion implantations in β-SiC, in Katoh et al's 2006 study [16] similar defect structures are seen in Si implanted samples as to those in neutron irradiated samples for a 800°C irradiation in both cases, however a higher number density of these defects is evident in the ion implanted material. Similar number densities of defects were seen in the higher temperature (1000°C) ion implantation. Dominant damage features at 10dpa Si ion implantation are seen as dislocation loops, with black spot defects similar to those seen in neutron irradiations seen at lower temperature. These dislocation loops are seen to be increasing in size with higher temperature implantations [16, 93, 94]. A swelling saturation is observed to be dependant on dose rate, with conditions of 1×10^{-3}dpa/s having a higher swelling saturation than 5×10^{-5}dpa/s at 1000°C [93]. A reduced swelling effect is seen with higher implantation temperatures, and a flatter fluence vs swelling profile seen with higher temperatures as well [92], as shown in Figure 2.14. High energy Si implantations have also shown

toughening mechanisms are clear post indentation, with branching, deflecting and tilting all visible within the crack analysis [95]. In addition to the effects described here a 5.1MeV Si implantation to about 20dpa has confirmed the isotropic swelling behaviour in 3C-SiC [94].

Effects of He implantations are seen with the formation of He platelets and dislocations loops post thermal annealing with a 65keV He implantation to 8000appm He [96]. There are however few other purely He implantation studies available in β-SiC. Additional dual beam studies with Si and He have shown the full effects of He to be unclear: the presence of He within the lattice is seen to increase the cavity density in grains at very high temperatures (1400°C), however the presence of this He is not seen to dictate the size of these cavities [93]. Studies looking at defect dynamics from first principles like those by D. Sun et al 2017 [97] on He implanted material and J. Sun et al 2017 [98] on H implanted material are helping us to better understand these types of defects and cavities, and when studied further along with irradiation studies will help understand the mechanisms behind damage formations.

The dual beam implantation method is seen to enhance swelling between 400°C and 800°C, but reduce swelling above this temperature [92]. Low temperature dual beam implantations see no effect of adding He to the swelling. In low dose experiments swelling effects are seen increasing across all temperature ranges to 1400°C [15]. A swelling saturation has been observed at a dose of 3dpa above 400°C and a dose of 1dpa at 60°C with around 1% volumetric swelling shown, which is thought to be down to amorphisation at low temperatures. Looking further into the changes in mechanical properties with a dual beam implantations, increases in hardness have also been observed, with simultaneous implantations enhancing the hardening effects [99]. An increase in fracture toughness has also been observed, with this effect being reduced with higher temperature implantations and with higher fluences. In addition to the Si and He dual beam experiments, a Au and He dual beam experiment has shown slightly different effects, where the addition of an Au implantation has caused no bubbles to be present in the sample, but instead high fluences caused blistering [96].

2.3.1.3 Studies in Mixed Phase Monolithic SiC forms

Most monolithic SiC studies have been either on α-SiC or β-SiC, however some work has been done on more standard commercially available forms, namely studies into irradiated REFEL

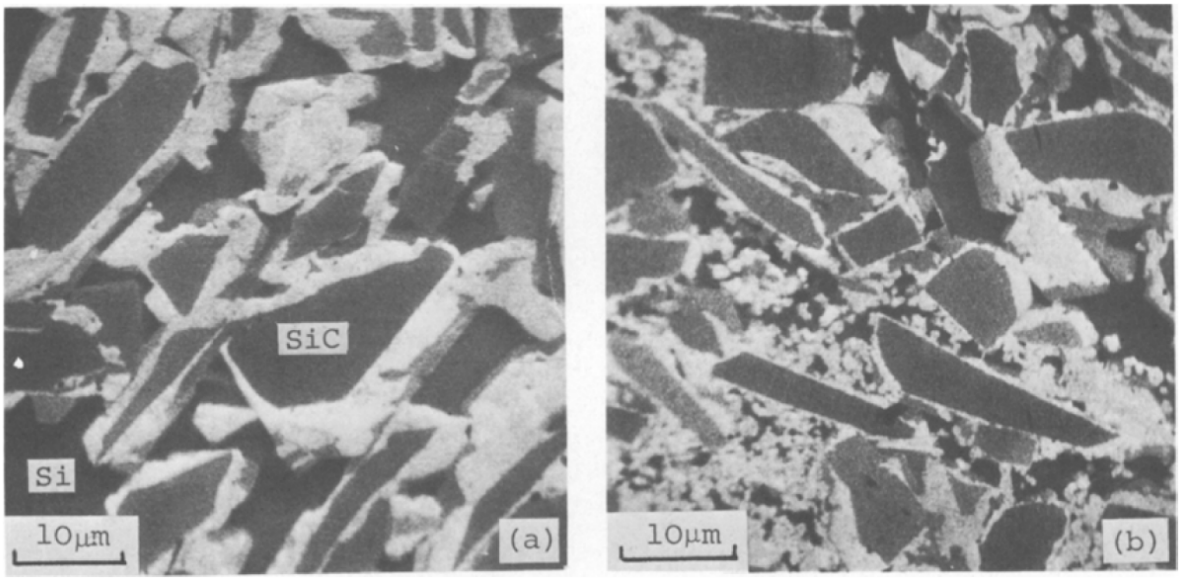


Figure 2.15: Scanning electron micrographs of uncoated polished sections of the REFEL Reaction Bonded SiC. The secondary electron images clearly show the (predominantly lighter contrast) epitaxial coatings on the original a-grits, while (b) also shows some of the isolated regions of fine (β) SiC crystals occurring in the residual silicon. The irregular darker areas in (a) are silicon and this can be confirmed by back-scattered imaging. Taken from Page 1980 [106].

SiC [100] and CVD SiC [54, 101, 102] along with a study into neutron effects on SiC fabricated by the nano-infiltration and transient eutectic phase process (NITE) [103, 104] . In addition to this some nano-engineered SiC studies have also been completed [96, 105].

A neutron irradiation study to a total fluence of 3×10^{21}n/m^2 into reaction bonded SiC was one of the very early radiation studies in SiC, and shows good correlation with more recent studies into more modern forms of SiC. Reaction bonded SiC material has about 10% free Si within it's structure, which will clearly change the macroscopic effects of irradiations on the material [106]. An example of a reaction bonded SiC microstructure is shown in Figure 2.15. It has been shown that the fracture strength and the elastic modulus rapidly drops with initial neutron radiation exposure, however these properties were both seen to recover with increased dose [100]. These macroscopic property changes seem to be due to swelling effects observed at the lattice and macroscopic scale. Many of these changes seem also to be due to internal cracking due to lattice misfit causing internal stress states. It has also been postulated that with low temperature irradiations transformations of β-SiC to α-SiC may occur. This was again seen in Parish et al's 2017 study [107] after a neutron irradiation at 1440°C to the much higher dose of 9dpa. Their investigation showed this transition occurring from Frank loops leading to

stacking faults. Stacking faults in β-SiC take the same form as an α-SiC crystal and act as starting points for transformations to occur.

Nogami et al's 2011 neutron irradiation study into CVD-SiC has shown very similar results to those reported in single crystal studies with increased hardness from doses up to 0.6dpa, which is independent of dose above a saturation point, and which is seen predominantly below 100°C where rapid increases in hardness are evident. However above this threshold temperature very little effect to hardness is seen [101]. This is reported as due to neutron induced defects being more stable at lower irradiation temperatures, and where these defects self-anneal with an increased irradiation temperature. It is also observed that an additional He implantation of 50MeV He to 800appm or 2700appm/dpa post neutron irradiation has no influence on these hardness changes. In addition it is observed that amorphisation within the material is not possible below 180°C. The addition of the He implantation is however seen to enhance swelling effects by stabilising vacancy type defects induced by the neutron irradiation. This then led to a 35% reduction in elastic modulus with a 750°C He implantation, and a 30% reduction in fracture toughness seemingly due to this elastic moduli reduction and increment of crack length under indentation. This fracture toughness reduction was observed in previous works like that of Park et al [99] and it is believed that the vacancy type defects stabilised by the He enhanced this crack propagation. Swelling effects have been seen to be dependant on irradiation temperature, but independent on fluence in Newsome et al's 2007 study [54] with temperatures ranging from $300 - 800$°C at doses of $0.6 - 4.6$dpa. Volumetric swelling of 1.9% was seen at the lowest temperature, reducing to a 0.7% volumetric swelling at 800°C. The effects of this swelling on the elastic modulus in this are significantly less than that seen with the He implantation, with only around a 9% reduction shown. The lack of a He implantation in this latter study is likely the main reason for this difference, although the differences across the neutron irradiation conditions again mean the two studies are very difficult to directly compare. In addition to this volumetric swelling, a reported increase in flexural strength was seen across all temperatures, with the effect increasing with higher doses, but decreasing with increased temperatures. This effect is similar to that already discussed in both α-SiC and β-SiC studies. Swelling effects have been investigated in depth in Katoh et al's recent study [102], where irradiations at 280°C were performed at HFIR with doses in a range of $0.02 - 11.8$dpa. They were able to measure

swelling with incredible accuracy, which allowed them to create a good model for transient swelling in SiC. In contrast to Newsome et al's study, in Koyanagi et al's 2014 NITE study a degregation in flexural strength was observed following irradiations at 830°C to 5.8dpa and 1270°C to 5.9dpa [103]. Terrani et al 2018 [104] have looked further into monolithic NITE material looking at the different effects varying percentage weights of sintering agent make (up to 10%), and saw no behaviour change in studies at $400 - 700$°C to 2&10dpa at HFIR.

The nano-engineered SiC examples of a nano-metric SiC powder investigated with a 4MeV Au implantation [105], and a nano-engineered SiC investigated with both a 65keV He implantation and a 9MeV Au implantation [96], are good examples of whether such nano-engineered materials are more radiation resistant than the more traditional materials. It is seen in the nano-metric SiC that a highly disordered and yet crystalline structure is present under low energy and a low fluence implantation (1×10^{14}ions/cm^2), however the material becomes totally amorphous when the fluence is increased to 5×10^{14}ions/cm^2. Totally amorphous structures are seen for damage over 0.35dpa, due to the material's high tendancy to rebuild locally to maintain inter-atomic geometries imposed by its strongly covalent nature, despite the fact that local disorder accumulates very quickly [105, 108–111]. It is shown that the nanostructured material shows no significant difference to conventional SiC materials seen across the literature. The nano-engineered SiC shows similar radiation damage structures with He bubbles forming at high temperature implantations, and a high density of stacking faults remaining after heavy ion implantation further suggesting it's radiation tolerance.

2.3.1.4 Summary of Radiation Damage in Monolithic SiC

As is clear from the literature discussed, there are a few characteristic radiation damage properties which are consistently seen in all types of SiC, however these characteristics are appearing at different temperature irradiations, different irradiation doses and different dose rates across similar SiC forms and the different SiC forms.

There seems to be no consistent understanding of what any level of damage is doing to SiC. While more recent studies are looking at wider ranges of irradiation parameters, this consistent understanding is still lacking. What is clear is that there are swelling effects which occur in SiC, and some conditions are causing amorphisation. It is also relatively consistently reported that

with some levels of damage hardening effects are seen, often however with a reduction in elastic modulus (likely due to the swelling effects). Despite this, opposite effects are seen under certain irradiation conditions, although mostly when amorphisation is observed. All these effects seem to level off or recover to pre-irradiation conditions at a given threshold in temperature or dose. Many studies look at annealing post irradiation and see re-crystallisation, although neither of these recoveries is seen across the range of even similar studies. There seems very little understanding of the mechanisms behind this, specifically with reference to particular doses or dose rates. This is despite the majority of the work focusing at the smaller scale, particularly with TEM studies looking at He effects and defect types, although recent MD, FEA and other computational techniques are helping to build understanding.

2.3.2 Studies in Silicon Carbide Composites

As discussed in Section 2.2.2 there are many different types of SiC fibres being produced, with different forms of matrix composition, as well as different sorts of interphases. Each of these aspects of the composite is clearly going to effect its response as a bulk to irradiation. Here irradiation studies are divided into neutron irradiation studies, and various ion implantation works

2.3.2.1 Studies of Neutron Irradiated SiC Composites

The early produced SiC composites made with Nicalon^{TM} fibres saw significant degradation under neutron radiation as studied by Snead [112, 113]. This early composite was produced with a C interphase layer with a CVI matrix. When studied post a 1dpa neutron irraditation at 300° with a focus on the condition of the C layer there was a marked decrease in both the interfacial shear strength and frictional resistance to sliding, along with about a 25% reduction in UTS [112]. With the same composite subject to a 30dpa 300°C irradiation and a 15dpa 365°C irradiation large amounts of fibre shrinkage were visible with an increase of elastic modulus from 200GPa to 240GPa and increased hardness of 18GPa to 25GPa shown in the fibres, likely an effect of the shrinkage. The matrix however showed marked reductions in both the elastic modulus and hardness [113]. This mismatch in effects from the fibres and the matrix are likely to have enhanced the problems around the interphase layer. These early composites

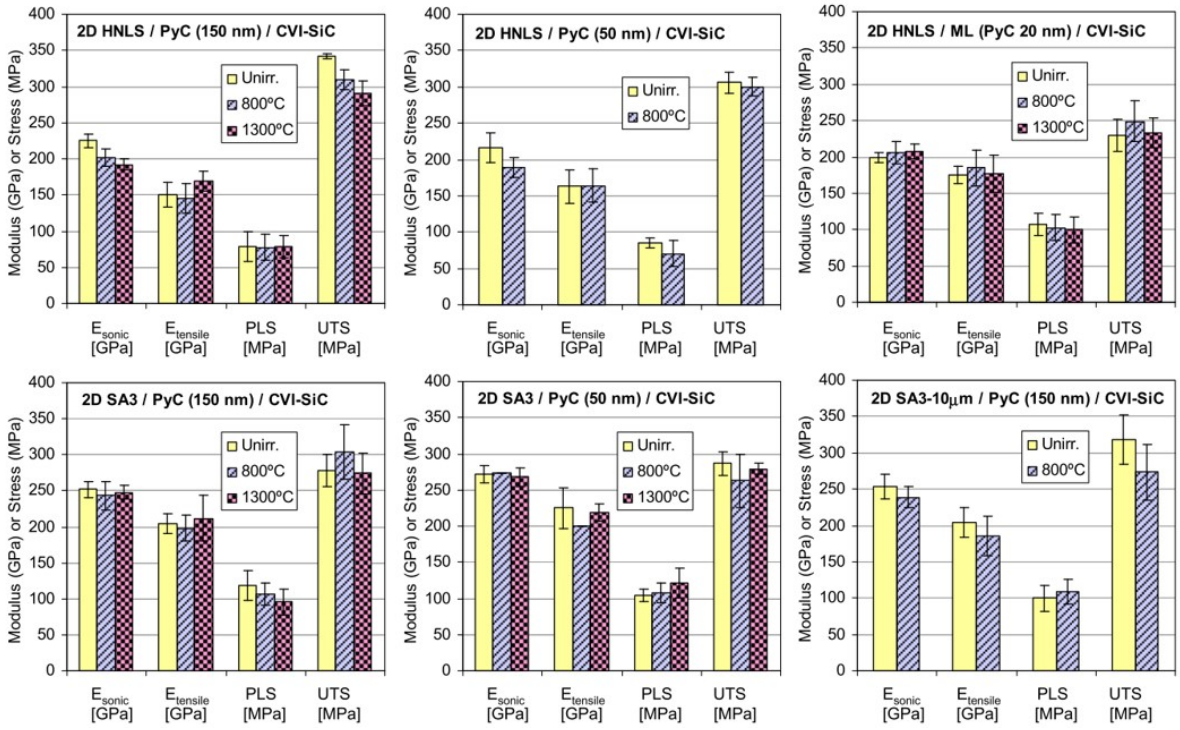


Figure 2.16: Summary of the tensile properties and sonic modulus values in unirradiated and irradiated conditions or composites with varying interphase types. E sonic and E tensile denote Youngs moduli determined by sonic resonance and tensile tangential fit, respectively. Error bars represent one standard deviation. Taken from Katoh et al 2011 [114]

were clearly not mechanically sound, and this in addition to the problems with their amorphous microstructure and the oxygen and free carbon meant these composites were not deemed suitable for any nuclear application [24].

The problems with the interphase layer were already clear in the early work, and investigations into the effects of different types of interphase have been extensive. Katoh et al's 2011 study looked at varying the size and type of interphase layer on both the Hi-Nicalon^{TM} Type S and the Tyranno^{TM} -SA3 fibres with a CVI matrix under irradiation conditions of 5.9 and $5.8 \times 10^2$5n/m^2 at 800 and 1300°C. The study looked at both varying thicknesses of a PyC interphase, as well as a multilayer PyC/SiC interphase [114]. Summaries of the tensile properties of these materials are shown in Figure 2.16, and what is clear is that none of the composites perform in quite the same way under the different irradiation conditions, however it is concluded that any changes under irradiation are minor. Despite this it is believed that the interphase layer may be optimum under the conditions tested, but may not be for higher temperature or higher dose irradiations. The study did conclude that the Tyranno^{TM}-SA3 fi-

bres were seen as particularly stable due to the maintaining of their tensile properties especially under the high temperature irradiation condition. Under similar conditions Ozawa et al found no signs of fracture resistance degradation and no change in crack extension behaviour [115,116] with both studies also using Hi-Nicalon^{TM} Type S and the Tyranno^{TM}-SA3 fibres, but different interphase types and matrix conditions. Koyanagi et al found in their 2014 study, again under similar neutron irradiation conditions, that the interlaminar shear strength was reduced by 30% due to the degradation of the PyC layer [103]. In this study a NITE matrix was used, but the problem was seen again in the interphase, especially at high temperatures of up to 1270°C and a high doses of around 5.8dpa, where the frictional stress at this interphase was greatly increased.

When this interphase degradation is examined at a higher dose of $71 - 74$dpa across a temperature range $300-800$°C the interphase layers are seeing notable shifts in behaviour where the Hi-Nicalon^{TM} Type S fibres are seeing no significant change [117]. Here the interphase is made up of 5 layers of PyC and 4 layers of SiC, and extensive cracking is seen, with a more pronounced degradation visible at the lower temperature as seen in Figure 2.17. Any change that is seen within the fibres is the secondary phase grains appearing larger post-irradiation, and this may cause changes to the mechanical properties of the composite, although it is not investigated in this study. Ozawa et al's 2016 study looked again at uni-directional Hi-Nicalon^{TM} Type S fibres with a PyC interphase in a CVI matrix, at a much lower dose of 1dpa at 1000°C. Again in this study a degradation of interfacial sliding stress was seen, likely inducing a reduction in PLS, however it was concluded that the composite had good irradiation resistance with an increase of UTS by about 30% [118].

The focus in most of these studies has been the problems surrounding the interphase region, although the studies which have looked into the mechanical behaviour of the neutron irradiated materials have generally agreed that there is no significant degradation in properties visible in composites made with Hi-Nicalon^{TM} Type S and Tyranno^{TM}-SA3 fibres [103, 114–116, 118]. Newsome et al's study looked at comparing some of the earlier generation fibre composites made with Hi-Nicalon^{TM} and Sylramic^{TM} with the Hi-Nicalon^{TM} Type S Gen III fibres wit h CVI matricies and multilayer C/SiC interphases under neutron irradiations from $0.6 - 4.6$dpa at 300, 600 and 800°C [54]. This work again agreed that there were no significant effects of the irradiation on the mechanical properties of the Hi-Nicalon^{TM} Type S composite, but did

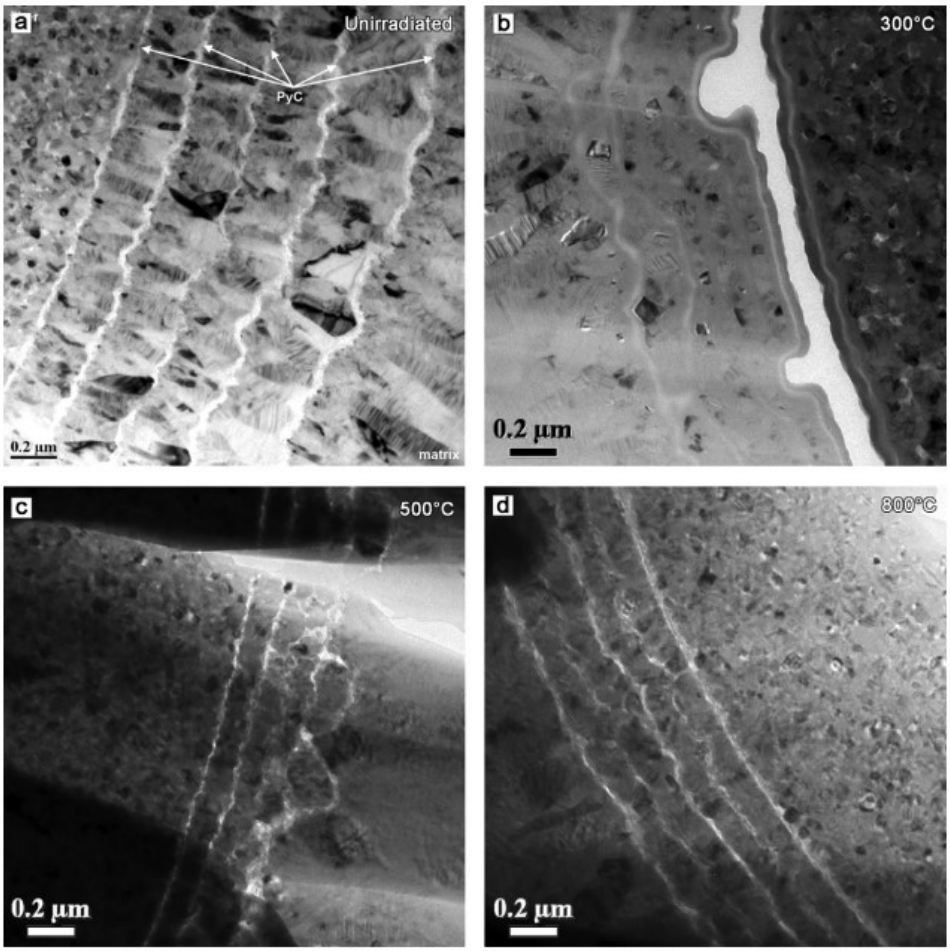


Figure 2.17: BF TEM images of the interphase regions from the (a) unirradiated sample and irradiated samples at (b) 71dpa at 300°C, (c) 74dpa at 500°C, and (d) 71dpa at 800°C. The sample irradiated at 300°C shows the greatest deterioration in the interphase, with a large gap present at the innermost PyC/SiC interface. Dark regions in (c) and (d) are artefacts from the FIB thinning procedure.. Taken from Perez-Berquist et al 2015 [117]

report swelling in the material similar to that seen in monolithic CVD studies. No significant degradation was seen, as the matrix and fibres have very similar compositions so exhibit very similar responses. The Hi-Nicalon^{TM} composite again showed similar swelling effects, however a de-coupling of the matrix and fibre was seen, causing significant degradation in mechanical properties. The Sylrammic^{TM} fibre composite showed the largest amount of swelling and most significant degradation of mechanical properties, most likely due to the boron sintering aids. This significant degradation under irradiation led the work to conclude that the Sylrammic^{TM} fibres were not suitable for nuclear applications. Koyanagi et al's 2017 and 2018 papers look into the mechanical properties of CVI SiC/SiC under both LWR relevant irradiation conditions [119] and with neutron damage up to $\sim$ 100dpa at 319°C and 629°C [120] in HFIR. While post LWR

conditions mechanical properties were observed not to alter, with flexural strength and the quasi-ductile nature of the composite remaining post irradiation, in the higher dose experiments there was a reduction in flexural strength and brittle fracture, failure and fibre pull-out occurred, along with debonding of the fibres and the matrix.

Where multiple annealing studies have been performed on monolithic SiC as discussed in Section 2.3.1, few investigations have been made on SiC composites. In Idris et al's 2017 work [121] they looked that the behaviour of both CVI and EPD composites and found annealing behaviour begun at $\sim 100°C$, the same temperature at which the irradiation had been performed. During annealing both continued to recover until $1200 - 1300°C$ where the EPD sample abruptly fully recovered, while the CVI sample did not fully recover in the range to 1400°C investigated.

2.3.2.2 Studies of Ion Implanted SiC Composites

As discussed in Section 2.3.2.1, the early Nicalon^{TM} fibres showed significant changes under neutron irradiation. Snead et al's 1992 study also implanted this early CVI martix composite with a 3MeV C implantation at implantation temperatures ranging from RT - 900°C and doses of 1dpa, 10dpa and 30dpa [113]. This C implantated sample exhibited significant amorphisation in the fibre, however an increase in the elastic modulus was still seen from 200-230GPa, which is again thought to be due to the densification. In addition the matrix saw a significant reduction in modulus from 400-280GPa. As previously stated these conditions make these composite types entirely unsuitable for nuclear applications. Nogami et al's 2001 study looked into the effects of H, He, Si and C combination implantations to 10dpa on composites made with the Gen II Hi-Nicalon^{TM} fibres with a CVI matrix and PyC interface [122]. The implantation damage here is much more significant than that seen in the neutron irradiation studies, mainly because of the gaseous presence of He and H. A volumetric shrinkage was clearly visible under the heavy ion implantation at 800°C with the addition of H enhancing this effect, however the presence of He is not seen to enhance this swelling effect. As shown in Figure 2.18 the interphase layer used here has sunk beneath the surface, due to displacement damage within the carbon layer. The additional effects of the He and H implantation on this sinkage are not fully known, however effects like this are clearly undesirable in a composite for nuclear applications.

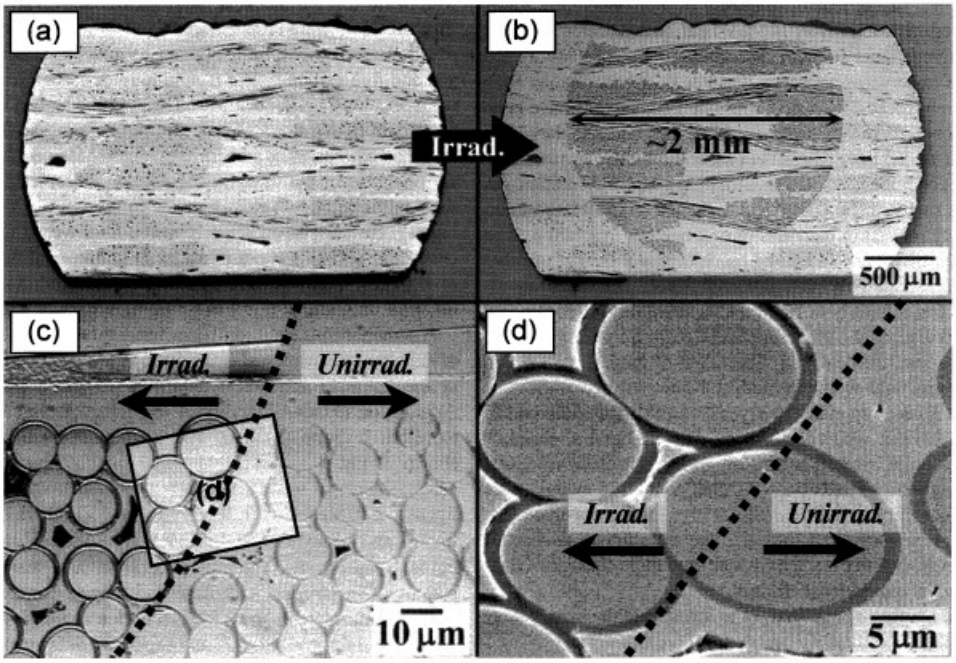


Figure 2.18: Observation of the irradiated surface of a SiC/SiC composite a) An optical micrograph of the surface before irradiation. b) An optical micrograph of the surface after irradiation. c),d):Optical micrograph (c) and SEM micrograph (d) of the boundary between the irradiated and unirradiated regions showning the interphase sinkage. Taken from Nogami et al 2001 [122]

Far more work has been done on the Gen III fibres, especially looking at the effects of dual beam implantations of Si and He. Cavities at the grain boundaries, as also seen in monolithic SiC, were reported in Miwa et al's study on a Hi-Nicalon^{TM} Type S fibre composite with a CVI matrix and PyC interphase [123]. These were appearing with a dose of about 10dpa from a triple beam experiment with 6MeV Si 1MeV He and 0.34MeV H at elevated temperatures of $1000 - 1500°C$. These cavities were enhanced with increased temperature implantations especially near the PyC interphase. The effects were enhanced by the He and H, especially at the lower temperature range, where He was also seen to enhance the cavity swelling. Similar He bubbles in the martix were seen in Duh et al's study [124], with a RT 2MeV He implantation to 10000appm, although no bubbles were seen in either the PyC interphase or the fibres. This study was looking at a similar Hi-Nicalon^{TM} Type S fibre based composite as well as a Tyranno^{TM}-SA composite made again with a CVI matrix and PyC interphase layer. When this was extended to a dual beam 6MeV Si and 1.5MeV He to both 10dpa and 100dpa, no He bubbles were seen in the lower dose implantation, but bubbles were visible in the higher dose implantation. Kishimoto et al also looked at a dual implantation on a Tyranno^{TM}-SA fibre based composites with CVI matricies

and both PyC and C/SiC interphase layers [15]. This study was again to a dose of 100dpa, but with a $5.1MeV$ Si and $1MeV$ He implantation at 1000°C. In this investigation He cavities were again seen, with a He induced cavity swelling of about 0.3% in the matrix, however there was no visible influence of the He on the microstructure of the intherphase. The C/SiC interphase types appeared stable post implantation despite a thinning of the layers, whereas the PyC layer appeared thicker post implantation although no fractures or shrinkage were seen around the fibres. This effect of the thickening of the PyC layer has not been reported in any other studies, although there have been far fewer investigations into the effect of ion implantations than there were of neutron irradiations on the properties around the interphase layer.

A heavy Xe ion implantation has also been performed on just the Tyranno^{TM}-SA3 fibres [125]. This was a 92MeV Xe implantation at 1000°C to 0.06dpa, and was mainly looking at the effects of this ion irradiation on the possible enhancement of creep within the fibres. It was shown that thermal creep within these fibres is negligible, and the irradiation strain-rate shows a linear dependence on the ion beam flux. It was concluded that in such fibres the ion energy loss regime is incredibly important when looking at ion implantation damage, and this principal can be easily extended to all ion implantation studies of SiC fibres and composites. Chai et al's 2018 [126] investigation on $3MeV$ Si implanted composite to 1&5dpa looked specifically at interphase properties again, using fibre push out techniques they saw a decrease in shear strength with increased dpa, due to a disordering of the PyC, and visible interphase cracks. This study links well with the neutron irradiated samples previously discussed.

The composites already discussed mostly have CVI (chemical vapour infiltrated) matricies. Where CVI matrices are pure SiC, the TEP or NITE process introduces sintering agents, and investigating the effect of these is vital. A study by Ho et al [59] has investigated the effects of a 7MeV Si implantation on a SA-Tyrannohex fibre based composite made with the hot press sintering process. This process used Si, Al, C and O in the sintering process with $< 1\%$wt Al. With a dose of around 20dpa at 1350°C voids, dislocation loops and edge dislocations are seen, and it is believed that the alumina present in the composite due to the sintering process is allowing larger voids to form. No direct mechanical properties are measured, but it is postulated that this inclusion is likely to cause additional degradation of mechanical properties, and would therefore be a less suitable technique for producing nuclear grade SiC composites.

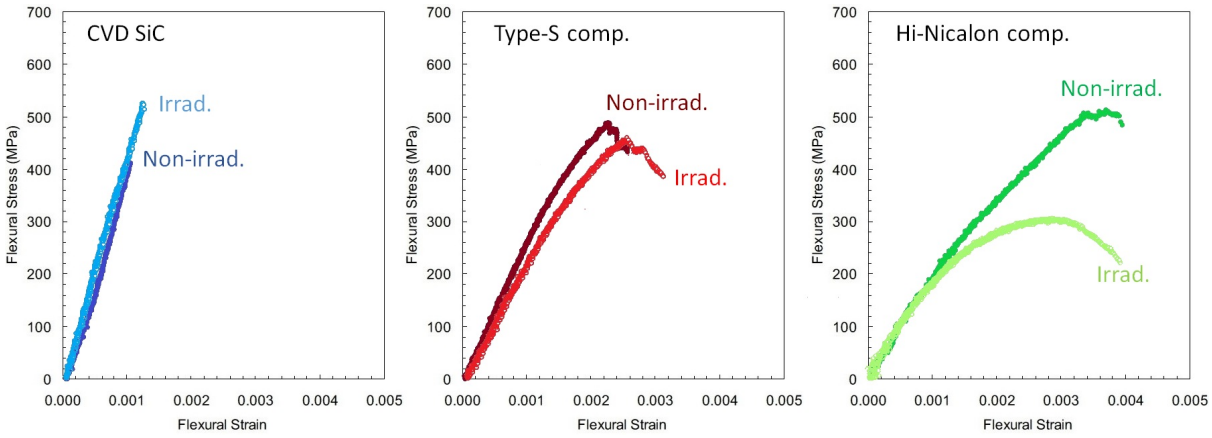


Figure 2.19: Typical exural stress-strain curves of non-irradiated and irradiated (at 800°C) CVD SiC (2.2 dpa), Hi-Nicalon^{TM} Type-S composites (2.1 dpa) and Hi-Nicalon^{TM} composites (2.2 dpa). Data from Newsome et al 2007 [54]

Fitriani et al's 2018 study [127] has investigated the use of non-standard sintering agents under a room temperature $0.2MeV$ helium implantation to a peak of 9dpa. They saw that despite all composites showing typical degradation of properties, the composite containing Sc-nitrate showed no significant change in microstructure, and saw no change in toughness. Further investigations into sintering agent effects with changes in radiation damage are vital for these types of material to become legitimate candidates for nuclear applications.

2.3.3 Comparison of different types of irradiation studies

Across the range of different SiC monoliths and composites there have been varied studies into the effects of different forms of radiation damage. Significant amounts of work have been done specifically looking at He implantations in both monolithic studies and composite studies, particularly looking at the effects of He on cavity formation and bubbles. The problem however is that it is very difficult to directly compare any of these studies across different material types, as one study in α-SiC is done with very different implantation conditions to a study on β-SiC or a SiC composite.

A particularly good example of the direct comparison between the monolithic CVD SiC and SiC/SiC composites was the study by Newsome et al [54]. Across a range of fusion relevant temperatures and varying neutron doses this study clearly showed where there is correlation between the behaviour of the monolithic form to different composite types and where their behaviour is in opposition. An example is with the characteristic SiC swelling. Here all forms

of SiC showed volumetric swelling, with swelling saturations above 1.4dpa at 800°C: 0.7% volumetric swelling in monolithic CVD SiC; 0.8% Hi- Nicalon^{TM} Type-S and; 0.6% in Hi-Nicalon^{TM}. Conversely when tests were performed looking at flexural strength at the same temperature the composites saw degregation in properties post-irradiation where the monolithic SiC saw an improvement as shown in Figure 2.19. It is looking at results like this, where a true comparison between forms of SiC can be seen, where we see that SiC/SiC composites may not be needed to create a more radiation tolerant form of SiC for fusion applications.

O'Connell et al's 2012 study [67] is one of the few to look directly at the differences between α-SiC and β-SiC, although they look at a single crystal 6H-SiC sample against a polycrystalline 3C-SiC. Before any implantations are looked at in this example the simple differences between a single crystal and polycrystalline sample mean that the differences seen are not directly comparable. While neither material showed amorphisation, the He-implanted 6H-SiC had a damage region with a high density of small bubbles and no cracking whereas the H implanted 3C-SiC had a high density of hydrogen platelets and severe cracking along the damage region. It is impossible to tell whether the differences discussed are due to the different ion implantation, different crystallinity or the different SiC polytype.

The investigation of ion implantation in comparison to a neutron irradiation should be more extensive, and there are some direct examples discussed here: Snead et al's 1992 study looking at early Nicalon^{TM} fibre based composites with neutron irradation and C implantation [113]; Katoh et al's 2006 study looking at polycrsytalline β-SiC with Si implantation and neutron irradation [16] and; Nogami et al's study looking at CVD SiC under He implantation and neutron irradiation [101]. The problem with each of these studies is that none of the conditions around the neutron irradiations and ion implantations match, not with the temperature, the dose or the dose rate. For this reason observations in these studies must be made separately, and they cannot be directly compared.

Despite these issues, with very few directly comparable studies available, some generalisations across these varied SiC studies can be made. In all cases radiation damage induced amorphisation causes a reduction in all observed mechanical properties, up to a 48% reduction of nano-hardness [73]. However these amorphisations tend to appear in low temperature low dose implantations, so would be unlikely to occur within a nuclear fusion environment where

most fusion SiC designs are looking at operating temperatures of $600 - 1000°C$, although it does appear to be a transition zone for other material properties. In monothinic SiC studies an initial increase in hardness and reduction in elastic modulus is observed, where these effect are reduced with increasing temperatures and doses, again these effects therefore may not be relevant in a fusion environment. Finally SiC/SiC composites are showing very little degradation under irradiations with Gen III fibres, although any problems which are occurring tend to be due to the carbon rich interphase layers. More in depth mechanical tests are however required to confirm this.

2.4 Nanoindentation

As already seen in the SiC radiation studies discussed, nanoindentation has been utilized for studying radiation damage. Nanoidentation has become an incredibly useful tool across all fields looking at changes in mechanical properties due to radiation damage, especially when that damage has been produced using ion implantations. This is due to the shallow damage ion implantation is able to produce in materials [128, 129]. Details of the technique have become well known and are briefly discussed in Section 3.1.

2.4.1 Nanoindentation for ion irradiation studies

Nanoindentation is commonly used for various small scale applications like MEMS and studies on thin films, as well as for radiation studies across many different materials, whether in tungsten studies like those performed by Gibson [130], or various nuclear appropriate steels like the Fe-Cr Alloys studies by Hardie [129]. Characterisation of irradiated materials using various micromechanical techniques are being used, utilizing the nanoinindenter to look at various small scale mechanics, especially using microcantilevers [128,131]. Where thin films have a distinctive layer, and the analysis for coating systems is well known [132], the situation becomes much more complex when looking at radiation damage, as the damage layers vary in structure throughout with levels of damage and added material from the implantation varying with implantation depth. There is no clear distinction between the implanted layer and the bulk material underneath and this means that additional mechanisms need to be considered when evaluating such studies.

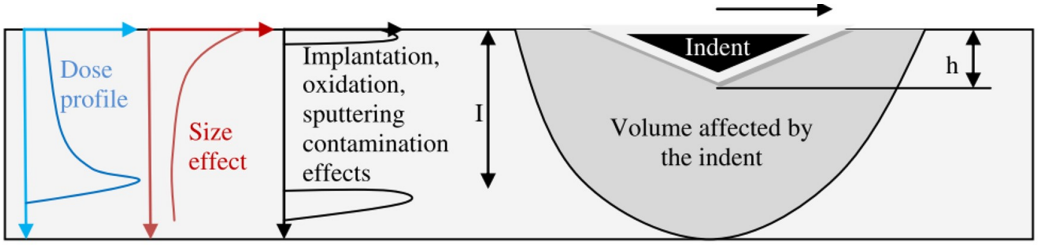


Figure 2.20: Effects to consider during nanoindentation of an ion irradiated surface. the changing dose profile, indentation size effects, contamination, all within the total material volume affected by the indentation test. Taken from Hosemann et al 2012 [134]

In SiC, the majority of nanoindntation studies performed on radiation damaged samples concern TRISO particle fuels like that by Rohbeck [133] and that of O'Connell [67] previously discussed. The issues associated with the lack of boundary between implanted and unimplanted material doesn't exist in these studies as the SiC layer on the TRISO fuel particle is a thin layer in in itself and the whole depth of the layer is damaged by ion irradiations.

Hosemann et al [134] have produced a comprehensive investigation on issues to consider when using nanoindentation on ion beam irradiated materials, which is summarised in Figure 2.20. The effect of these are less dramatic in brittle materials like SiC where a smaller plastic zone develops around the indent, however it is clear that even during the depth profile of a nanoindentation various different radiation damage induced effects will be in play.

Nanoindentation developed out of a need to investigate things at a smaller scale than were traditionally performed with Vickers Hardness tests, and along with this techniques for measuring mechanical properties were adapted to suit this smaller scale field. In traditional indentation models such at the Hertzian Contact theory for spherical contact a basic understanding of the elastic/plastic behaviour and stress fields were obtained. Looking forward to the Berkovich indenter tips generally used in nanoindentation analysis techniques were developed to obtain good data for hardness and elastic modulus, as well as looking at things such as fracture toughness. Predominantly used in modern nanoindentation systems is Oliver-Pharr analysis [135–137], where instead of having to directly measure the indentation contact area post indentation, a contact area can be calibrated from details of the indenter tip and indentations into known materials, and analysis us not constrained by tip geometries. In this way data can be quickly and efficiently collated. With advances in machine technology like the introduction of Continuous Stiffness Measurement (CSM) [138] more refinements have been made [139, 140], and depth

dependant data throughout a single indentation has become possible.

2.4.2 Indentation Damage Mechanisms

Nanoindentation can be simply used as a tool to obtain hardness and elastic modulus data, however there are a variety of important mechanisms occurring during indentation that can also lead to understanding of fracture toughness and crack formation.

Even the sharpest of Berkovich indenter's has a rounded tip at some scale where the Hertzian contact model can be applied to look at the onset of stresses on the surface of the material [139], this is incredibly helpful as under the Hertzian model elastic and plastic behaviours can be separated out. Fracture under this situation in a brittle material like SiC occurs when maximum Hertzian stresses or flexural stresses are equal to bulk strength. This then gives a critical load for surface 'cone' cracks and subsurface radial cracks [52]. Once this beginning phase is over the true effects of the geometry of the Berkovich indenter comes into effect: cracking can occur, as can dislocation nucleation, which is both stress and thermally assisted. Schuh et al [141] have investigated how dislocation nucleation relates to the onset of plasticity materials especially looking at 4H-SiC: plastic flow can occur, moving material out of the way of the indenter tip and creating pile up. They saw how point defects are capable of carrying significant amounts of plastic strain, and that dislocation loops grow from atomic sized regions where the lattice buckles due to the compressive stress of the indentation load. Whilst some deformation mechanisms are not directly linked to the load displacement curves produced during indentation, Schuh et al did link 'pop in' events to various deformation mechanisms: discrete strain accommodation; formation of cracks; shear bands and; breakaway of dislocations from pinning points.

Turning to the 2011 work of Zhao et al [142] on the onset of plastic deformation and cracking behaviour in 3C-SiC, where dislocations and microcracks are expected. They found that plasticity occurred when the maximum shear stress exceeded the threshold of shear strength. Slip was seen on the {111} planes, and the region nearest the tip was most highly deformed, with a high concentration of shear bands created to accommodate the deformation. This was described as sue to the fact that the intersections of the fault surfaces have concentrated stresses, and cracks would be preferentially initiated at these points, as also described by the Cottrell model. In 2011 Bhakhri et al [143] also looked into mechanical behaviour of SiC, where they concluded

in a similar way that the orientation of indents relative to a primary slip plane, in SiC the basal plane, is of larger influence on the hardness and deformation of SiC than the presence of a grain boundary. They also noted that with the complex nature of a Berkovich indenter tip, non-uniform deformation is seen, which involves multi-axial stress states in the deformed material.

It is clear that fully understanding the stress states in a brittle material like SiC is not simple. In Ostojic et al's 1987 study [144] they looked at the effects of the two extreme types of indenter tips: a blunt tip and a sharp one. A blunt tip, as previously mentioned can be approximated to a Hertzian cone, where the load is distributed over the whole contact area as a compression stress. With elastic deformation tensile stresses move to the surface of the material outside the contact regime, with compression stresses occurring below. This tensile filed moves out until a flaw is found in the material at which a crack is formed. As the load is increased this crack can propagate all the way around the spherical indenter creating a Hertzian cone of fracture. When the load is removed some of these cracks then close again. The other extreme is the ideal situation of a perfectly sharp indenter tip, where all deformation is essentially plastic. Plastic deformation begins at the tip and spreads with the corners of the indenter, with the tensile zone adjacent to the contact with the tip. This produces cracks along the corners of the indenter tip down through the material. In reality indentation has a mixture of these two modes, with the elastic and plastic regimes and different areas of tensile stress on the surface. In Zhao et al's study [142] none of these 'cone' type cracks were seen in 3C-Sic, leading them to believe that cracks were initiated from the centre of the deformation region.

Nawaz et al's 2019 study [145] looking at effects in 3C-SiC thin films at elevated temperatures describes how the work done in indentation is equated to the energy consumed in the making of the indentation impression. They also describe how planes with lower inter-planar spacing, i.e. those with higher atomic densities are more susceptible to slip, and cleavage failure can occur. Alvarado-Rivera et al's 2011 study [146] also looked into hybrid thin films, this time focussing on fracture toughness and energy dissipation. As with many of these other studies they used 'pop-in' events to look at what mechanisms were occuring. They describe how crack formation implies a stess singulatiry which is averted by plastic deformation beneath the indenter point until the contact is large enough to support the load. A first 'pop-in' event is seen to represent

the critial load when a flaw in the deformation zone becomes unstable leading to the formation of radial cracks on the tensile planes. Some of these cracks below the surface close on unloading, as previously described by Ostojic et al [144], however these leads to an opening up in the residual tensile field at the surface as the contact area recovers the elastic component, opening up surface cracks in the material. Surface stress effects are made even more complex by any sort of microscopic residual stresses as seen in Tandon et al's work [147], where cracks were seen to bridge across areas with residual stress, and in some cases after an incidence of ions no cracking was observed. In contrast Datye et al's 2018 study concluded that in 6H-SiC cracks were extended on the removal of the indentation load due to a residual stress field.

There are a variety of stress states seen to be occurring in these studies, and as Guo et al [148] said in their 2020 study on fracture toughness, there is a great uncertainty in the stress field under the indenter. The deformation zone is incredibly different to metals [149].

2.5 Conclusion

Although there have been various studies into radiation damage effects in Silicon Carbide, we still lack a basic understanding of the mechanisms behind radiation damage effects due to the fact that it is a semi-conductor ceramic and not a metal. The traditional models used to investigate the damage in metals have traditionally been transferred across for use in ceramics like silicon carbide, however it is clear they are not adequate. Significantly within ion implantation studies is the influence of electronic stopping within the material: metals do not have large amounts of electronic stopping but ceramics do [125]. With all the microstructural studies available more computational models are being explored to allow for a clearer understanding of the various behaviours in both unirradiated and irradiated SiC [150–159]. Few if any studies are actually comparable against each other, with so many variables in these radiation studies.

At no point within the history of the literature is it clear why SiC/SiC composites are considered more suitable than any of the monolithic forms which are equally well investigated. Despite this, the advanced composites do appear to have good radiation resistance at the small scale although there are still clear problems associated with these materials. For this reason this work first focusses back on the basics of commercially available monolithic SiC materials, to try and establish a base point for what these materials can give in a radiation environment.

Following on from this monolithic and composite material was produced and put through the same radiation testing and evaluations to look directly and what sort of advantages are clear, or not.

The main issues throughout the literature appear to be an inconsistency with results, and no cohesive narrative to be able to adequately compare any of the materials to see which is likely to perform best within a fusion environment. This has led to broad generalisations being put forward in many recent review articles on the subject, with many conclusions simply being that we need to improve our basic understandings of the foundations of radiation damage in SiC for all basic material properties [10, 23, 24, 31, 160–163].

This project aims to directly address these deficiencies by doing a group of irradiation studies across a single material, so that the true effects of dose and temperature can be observed, alongside this some of these irradiation studies will be done an a variety of material, including some produced for this project, to look into the exact nature of differences and changes these different variables make.

With SiC still being a widely considered material for fusion and fission applications it is vital that a cohesive understanding be developed. It may be the case that advanced SiC/SiC composite designs are not required as part of the solution for a fusion power plant design. Instead a simpler and cheaper monolithic SiC design may be possible. The problem remains that further direct comparisons between different SiC forms radiation tolerances needs to be fully investigated in fully fusion relevant regimes. There is also a significant lack of mechanical property investigations in all fields, especially looking at fusion operational temperatures.

Whilst investigations into microscopic behaviours of these materials is vital to understand why they behave the way they do, first it must be established how they behave at larger scales. For this reason this project focusses on micromechanics, to delve fully into the mechanical properties of these SiC materials, and how they actually respond to radiation damage. Whilst irradiation studies have been performed across a myriad of elevated temperatures, for us to be able to use them as functional engineering materials, investigations as to how their properties change whilst in those elevated temperatures is vital. For this reason this project utilizes high temperature nanoindentation, to try and establish what operational temperatures will do to the materials, and how the damage caused by the radiation will change.

2.6 Research Goals

This thesis aims to look specifically at the effects of ion irradiation damage on the mechanical properties of silicon carbide, as well as enabling direct comparisons between different materials and different irradiation conditions with the knowledge of other irradiation effects being constant between studies. In particular the following studies are made:

- Chapter 4 focusses first on the direct comparison of mechanical properties between different commercially available SiC monoliths under the same silicon ion implantation. Following from this study, a single form of commercially available SiC is further investigated over a limited range of Si ion implantation and a Ne ion implantation including under fusion relevant temperatures, allowing investigation of the effects of radiation damage similar to those expected from a fusion reactor.

- Chapter 5 focusses on the fabrication and testing of monolithic and composite forms of TEP SiC, allowing for changes in fabrication variables, especially sintering agents, to be investigated. The best of these materials were then assessed under Si ion implantations to evaluate mechanical properties over a range of irradiation conditions including under fusion relevant temperatures.

- Chapter 6 focusses on testing of SiC at elevated temperatures, allowing for mechanical testing to be performed at fusion in-service temperature conditions on a Si ion implanted SiC material.

Chapter 3

Experimental Techniques

The work carried out in this thesis has been performed using various techniques. The principle techniques used here have been Nanoindentation, Scanning Electron Microscope (SEM) and associated analytical techniques, Focused Ion Beam (FIB), ion implantation and Raman Spectroscopy. SEM is a standard technique so details will not be given here [164], but the other techniques will be discussed, looking at their background theory, technical specifications, operating procedures and known experimental problems.

3.1 Nanoindentation

Nanoindentation is a widely used technique where an applied load is directed through a tip with well known mechanical properties into the surface of a material, the response of the material itself can indicate its unknown mechanical properties. The manner in which the material is deformed can allow hardness and elastic modulus to be calcuated, as well as observations about fracture mechanics, and fracture toughness; as well as other observations about the characteristic behaviour of the material, like if pile up or slip is occurring. By more detailed observations with other techniques it can be used to evaluate how dislocations are formed and how they move with added loads. Some of these effects can make acurate calculations of hardness and elastic modulus more difficult, as pile-up for example changes the contact area of the indenter tip with the surface, and contact area is vital for hardness calculations. Nanoindentation can be incredibly site specific, whether for a surface location, or for a minimal depth to be studied, which makes it ideal for thin film, materials with varying microstructures and radiation damage. It is difficult to be accurate with soft materials. One of the principle limitations of any nanoindenter, is the software with which data is accumulated. With high levels of sampling within a given load change, a single indentation can have incredibly large amounts of data associated with it. This means that most software discretises this data internally before giving 'summary' data to the user. The basic data retrieved from any nanoindentation is that of load and displacement. These can then be used to calculate material properties, aspects such as strain rate can also be

directly measured and controlled.

All room temperature nanoindentation in this work was performed using an MTS Nanoindenter XP (MTS NANO, Oakridge, TN, USA). A schematic of this system is showed in Figure 3.1. The indenter tip is controlled by the load shaft through the coil and magnet assembly. This system allows a known load to be applied at all times while displacement is measured by the capacitance gauge. A maximum load on $500mN$ can be applied through the system with a maximum displacement of $0.5mm$. The available force resolution is $50nN$ with a depth resolution of $0.01nm$. Indentations in this project were performed with a constant strain rate of $0.05s^{-1}$.

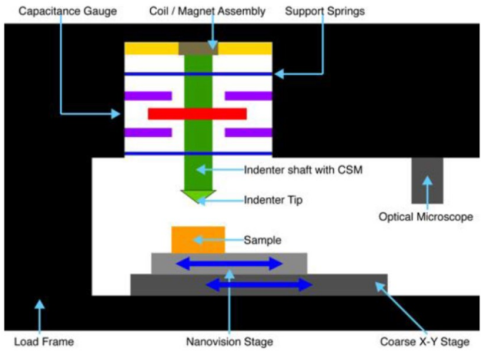


Figure 3.1: Schematic showing the MTS Nanoindenter XP

A user automatically sets the system for depth-control, however it is a load-controlled system where a Proportional-Integral-Derivative (PID) controller provides a rapid feedback loop to allow a constant displacement rate: an applied load causes a measured displacement. For the displacement rate to be kept constant the PID controller adjusts the loading rate as required.

Continuous Stiffness Measurement (CSM) is used throughout all indentations on this equipment allowing for accurate hardness and elastic modulus data to be taken through the whole depth of an indentation [138, 140]. The CSM is achieved by a small sinusoidal curve being overlaid on the load signal with a harmonic displacement target of $2nm$ and frequency target of $45Hz$. This method is effectively running multiple load-unload test cycles with increasing depth, however with the high frequency of the oscillation all drift effects become negligible. This creates a far better system for high definition collection of material properties with varying depth.

3.2 Nanoindentation Data Analysis

Data from the NanoXP is initially in the form of load dependant displacement curves, these were than analysed using the standard Oliver-Pharr method [**?**]. Modulus data is obtained from the slope of the load-displacement unload curve, while hardness is calculated my the maximum load over the total contact area. As the machine uses CSM these calculations are performed

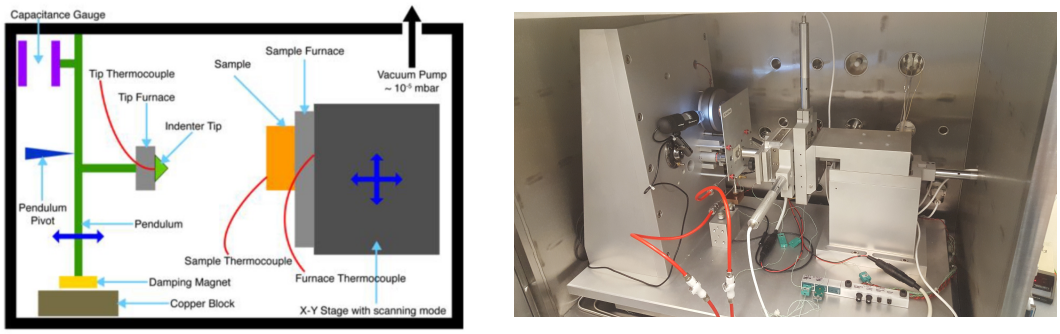
continuously during each indentation run allowing for depth defined data collection and analysis.

Both hardness and modulus results vary depending on the geometry of the indenter tip and drift in the system, the modulus data is also effected by frame compliance. Accurate tip geometries were calculated regularly during indentation testing by using fused silica as a calibration sample, meaning the contact area was known for any indentation depth. Frame compliance was corrected for by making sure modulus data was size independent outside of any surface effects of the calibration material. Thermal drift was generally not a problem in room temperature tests with indentation runs not started until drift fell below $0.05nms^{-1}$, although additional vibrations caused by doors slamming and other external factors did add to drift and noise in the system that could not be mitigated for. Indentation runs which exhibited fluctuations due to these external vibrations were removed from data sets as anomalous results.

3.3 Hot Nanoindentation

Where nanoindentation itself has become a widely used technique, expanding its utility into higher temperature regimes is still relatively new. The aim is to be able to understand the real behaviour of materials, at operational temperatures, and how those mechanical properties change with heating or cooling. Such experiments are mostly performed in vacuum, although some are performed with inert gasses, and these experiments take days if not weeks to perform, where equivalent data at room temperature can be obtained in hours. The technical challenges of this techniques will be further discussed in this work. On top of similar limitations to room temperature nanoindentation, performing nanoindentation at elevated temperatures has additional limitations. Mostly to do with not being able to directly check the location of each indentation or array between data sets, as the microscope is not usable at elevated temperatures. Additionally there are more aspects which can influence the behaviour of the machine with drift. As is expected at higher temperatures, there are additional problems with making sure the sample is firmly attached as most adhesives cannot perform at high temperatures. In addition both the material and the indenter tip itself will likely expand as temperature increases, so locating the surface for beginning an indentation becomes more of a challenge. Also additional mechanisms within the material, and its response to load, will be occurring at higher temperatures.

The hot nanoindentation system used in this project was manufactured by with MicroMaterials Ltd (Wrexham, UK) and mainly developed at Oxford and is now sold as the NanoTest Xtreme. The basic nanoindentation system runs in a similar way to room temperature systems with the sharp indenter tip being driven intro the surface of a material under a known load and displacement. However the hot nanoindentation system is mounted with horizontal indentation occurring from a pendulum system. A schematic of the system along with a photograph can be seen in Figure 3.2. This horizontal indentation system is preferable for the high temperature system, with better temperature control available reducing convective heating, along with allowing easy access for the cooling system for the shield plate which protects the pendulum system (seen in the photograph in Figure 3.2b). The arc of the pendulum for indentation is small enough over the depth of indentations to be effectively a straight indentation, so load-displacement data is identical to that collected from the Nanoindenter XP room temperature system. The big difference between the two systems, however, is that the hot nanoindentation system does not allow for CSM indentation, so indenets were made using series of load-partial unload cycles as fully discussed in Section 6.2.3.



(a) **(b)**

Figure 3.2: Schematic (not to scale) [130] and photograph showing hot nanoindentation system.

Samples were carefully mounted onto a furnace using a high-temperature chemical set cement (OMEGABOND^{TM} 600), along with a thermocouple placed next to the sample for sample surface temperature measurements during the experiment. Samples were carefully placed to have good thermal conduct with the furnace, and the cement could not protrude about the height of the sample so as to avoid contact with the indenter surround in-situ.

A diamond Berkovich tip was used for all experiments in this work. Once a tip had been installed into the machine in depth tests were performed to confirm the depth signal was re-

sponding properly with the movement of the pendulum. The voltage across the depth signal capacitors was also adjusted to $\sim$ 9V for the room temperature tests. Before experiments on samples were made calibrations were done on tungsten and fused silica samples to obtain an accurate Diamond Area Function (DAF) and good calibrations for hardness and modulus results. Microscope to indenter calibrations were also performed along with a record of the distance from the indenter plane to the microscope plane to ensure the stage would not move with excess force into the indenter tip when switching between the microscope and the indenter. Once the sample on the furnace was placed into the machine accurate notation of the sample location was needed as the sample could not be moved back to the microscope once sample heating had begun.

Before heating could occur the whole system was pumped and purged with N_2 then pumped with a turbo pump to a vacuum of 10^{-5}mbar. Tests were not made until the vacuum had stabilised which took $\sim$ 12 $-$ 24hrs. While the system was under vacuum it could not be touched, or the vacuum pumps would destabilised as the whole system is on a platform to help reduce vibrations from disturbing load-displacement data collection.

Once a stable vacuum was obtained the system could be used at temperature. Before heating was perfomed the sample was moved $\sim 500\mu m$ from the indenter tip to prevent thermal expansion causing impact and damaging the tip. The furnace which heats the sample was PID controlled heating element and the indenter has a fixed power heater. These are set to the desired temperature and again left to fully stabilise before any experiments were performed. True stabilisation could be checked by observing the signal display for the load/depth controller, if there was a large variation in the output signal the indenter and stage were not stabilised. Although the system had heated the two heating elements to the desired temperature the actual temperatures of the sample and the tip were likely to vary slightly from this. Identical temperatures were required for both the indenter tip and the sample surface: as in a vacuum there is no convective heating helping to equilibrate the system. Test indentations had to be performed to accurately confirm a true equilibrium of temperatures. If the sample and indenter tip were not in equilibrium, conductive heating would occur between the sample and the indenter tip causing high amounts of thermal drift in the indentation. By ensuring a true temperature match between the sample and indenter tip no computational modelling of the contact was

needed for accurate drift correction [165,166]. This process of thermal matching is described in depth in Section 6.2.2. In addition to thermal matching, tests had to be performed to ensure the pendulum was stabilised along with a confirmation of the depth signal in the same way as performed when the indenter tip was installed. The voltage across the capacitors was also adjusted to ensure the depth signal was normalised. With increased temperature the required depth signal voltage is reduced due to the effects of the increased temperature on the behaviour of the indenter tip and shaft. At this stage indentation runs at temperature were performed.

The majority of the methods used in these hot nanoindentation experiments were developed by J. Gibson [130].

3.4 Hot Nanoindentation Data Analysis

The MicroMaterials software which runs the operation of the hot nanoindenter performs standard Oliver-Pharr [135] nanoindentaion analysis in the same way as the room temperature systems to produce hardness and modulus data. Along with this thermal drift and drift at peak load values were given. These were then output to a MATLAB script developed as part of this project for collation and further analysis, allowing for more in depth probing of the results. Temperature measurements were not collected by the MicroMaterials software so were manually attached to each indentation array. Further discussion on calibration techniques are discussed in Chapter 6.

The hot nanoindentation system produced all moduli results as reduced moduli. For completeness and better comparison to room temperature data, a proper conversion of reduced moduli to elastic moduli was required. In the work by Oliver and Pharr [**?**] these relations are given, and as contact stiffness measurements are possible with this machine as outlined by Wheeler et al [167] these are applicable to the hot nanoindentation studies here. Reduced modulus is easier to calculate from the raw data produced:

$$E_r = \frac{\sqrt{\pi}}{2B}\frac{S}{\sqrt{A_p}} \tag{3.1}$$

where the reduced modulus E_r is given from any indentation as a function of the geometric constant B, the contact stiffness S and the contact area A_p. This reduced modulus is a com-

bination of both the indenter and sample's elastic deformation. To then convert this reduced modulus data the below equation was used:

$$E_r = \left(\frac{1 - {\nu_s}^2}{E_s} + \frac{1 - {\nu_i}^2}{E_i} \right)^{-1} \tag{3.2}$$

where ν_s and ν_i are the possions ratios of the sample and indenter tip respectively and E_s and E_i are their respective elastic moduli. At elevated temperatures this becomes more complicated as both the indenter and sample have temperature dependent moduli. The elastic modulus of the indenter tip, diamond, to any given temperature T (in °K) was estimated using Wachtmans Equation 3.3 [168]:

$$E = E_0 - CTe^{-\frac{T_0}{T}} \tag{3.3}$$

here E_0 is the elastic modulus at 0K, T_0 is the elevated temperature (in °K) where the elastic modulus approaches a linear relationship with temperature, and where C is an exponential fitting factor. This is an empirical formula derived based on understanding of how, as temperature is reduced, the Youngs modulus curve decreases from a constant value at high temperatures to zero at absolute zero. The exponential form of the equation is related to the degree of excitation of the vibrational modes, given as a Boltzmann factor. It has been used to estimate changes in elastic modulus with temperature in various fields, and at this stage is the best way of evaluating the changes to known materials with temperature. Using diamond elastic parameters given by Wheeler et al [167], elastic moduli across the temperature range for the indenter tip were calculated using Equation 3.3. Sample elastic moduli were then calculated for in this work using Equation 3.2.

3.5 FIB Milling

FIB techniques have been widely used since about 1993 [169] for various purposes, from micro-machining to preparation of Transmission Electron Microscope (TEM) lift-outs. The system used in this project was a Zeiss Auriga Dual Beam system similar to most modern commercial systems.

Modern FIB's tend to use a liquid gallium metal ion source with accelerating voltages of

$5-30KeV$. The liquid gallium flows down to the tip of a needle from the reserve where a large potential difference between the needle and extractor electrode extracts a beam of gallium ions. With emission currents of $\sim 2\mu A$ the beam currents of $1pA-16nA$ are defined by the apertures. These beam currents produce a spot size varying from $10nm-500nm$. The ion beam is then rastered over the surface of a material and secondary electrons are collected to form an image in the same way as an SEM system.

The secondary electrons collected to form an image are produced from inelastic collisions of the gallium ions with electrons on the surface of the material. The majority of collisions on the surface, however, are elastic collisions of the gallium ions with the atoms in the material, these elastic collisions displace or eject these atoms from the surface. This process is the primary function of the FIB as when focussed on a specific area, the gallium ion beam will raster across the desired area allowing for sub-micron machining.

FIB milling is an incredibly useful technique for looking at small specific areas, and is especially useful for producing site specific samples for other techniques like TEM. It does however have its problems. With FIB milling there is a balance between how quick you wish to produced something, and how accurate that area is. Higher currents produce much higher rates of damage, not just in the beam 'spot' itself but also in the area around it. Each type of material, polytype and grain orientation with mill at a different rate, as atoms require different amounts of energy to be displaced. This means that in mixed materials having an even surface can become difficult.

In this project the FIB was mostly used to mill cross-sections into samples to observe fracture behaviour beneath indentations. The techniques are similar to those seen in cementitious composites by Trtik et al [170] and Park et al's work also observing cracking behaviour in irradiated SiC [95]. Using these techniques, first a large trench was milled with a high current beam $16nA$ a distance of $5\mu m$ from the desired location of the cross section. This distance was to ensure beam tails and sputtering did not effect observation of the desired location [171,172]. The depth of trenches had to allow line of sight for the SEM at 54° for observation of features. Once trenches were deemed deep enough the FIB was used to gradually remove material approaching the desired location with lower beam currents of $1nA$. Once the desired area had been reached layers were polished with $120pA$ beams to allow for good SEM imaging. This was continued

through a desired width allowing for multiple images to be taken through a cross section.

A big problem encountered with FIB milling in this work was re-deposition of material. During finer milling material preferentially deposited back into the trenches obscuring the view of cross-sections. In depth analysis of FIB effects on SiC also show ion beam effect causing swelling in SiC in the same way as seen in radiation damage studies [173] as a big problem with the technique is gallium contamination [174] as stated above. All areas where the FIB had been used to image samples produced optical changes in the material visible with the naked eye, and small amounts of imaging was seen to drastically change the surface of SiC materials studied. Despite this FIB milling was the best technique to observe certain phenomena during this project, and was also used to produce TEM lift-outs. It had been hoped that the technique could also be used for producing micro-cantilevers for further micromechanical testing, however the surface damage caused by the FIB created too many changes in properties to allow for proper evaluation using this method.

3.6 Ion implantation

Ion implantations in this work were performed at the Ion Beam Centre (IBC) National Facility at Surrey University. The facility is a 2 MV High Energy Van de Graaff tandem accelerator which operates at temperatures up to $\sim 800°C$. Here ions are accelerated through the 2 MV accelerator before being focused into the target chamber through a 50mm aperture, hitting the sample perpendicular to the surface. To get even implantation across the surface the beam is rastered across the surface. Four faraday cups at the corners of the sample control the dose and dose rate. During implantation the target chamber is at $\sim 2 \times 10^{-6}$Pa.

The implantations are shown in Table 3.1, with the details of each given fully in Table 3.2 with damage given as calculated in Section 3.7, converted from the doses shown. The samples used in this thesis are discussed in detail in later chapters and are referred to in the same way here. The samples used in Chapter 4 are Direct Sintered SiC (DS-SiC), Hot Pressed SiC (HP-SiC) and Reaction Bonded SiC (REFEL); the samples used in Chapter 5 are C-10-1900-75, C-5-1900-75 and M-10-1800-75.

For the silicon implantations Si^2+ ions were produced from a SO-70 hot penning source using SiF_4 gas. For the neon implantation Ne+ ions were produced from a cold penning ion

Samples	Implantation Date	Implanted Ion	Temperature (°C)	Damage (dpa)
DS-SiC HP-SiC REFEL	Sept - 2015	Si	300	Average 1.49 Peak 2.43
DS-SiC C-10-1900-75 C-5-1900-75 M-10-1800-75	Feb - 2019	Si	300	Average 1.49 Peak 2.43
DS-SiC C-10-1900-75 C-5-1900-75 M-10-1800-75	Dec - 2017	Si	750	Average 1.49 Peak 2.43
DS-SiC C-10-1900-75 C-5-1900-75 M-10-1800-75	Dec - 2017	Si	300	Average 0.149 Peak 0.243
DS-SiC C-10-1900-75 C-5-1900-75 M-10-1800-75	Jan - 2019	Si	750	Average 0.149 Peak 0.243
DS-SiC	Aug - 2018	Ne	300	Average 1.51 Peak 2.42

Table 3.1: Irradiated Materials

source using Ne gas. The implantations used three implantation energies to achieve consistent damage through the implanted layer. The energies were implanted consecutively starting with the high accelerating voltages before reducing to lower energies.

3.7 Damage Calculations

For each ion implantation damage calculations were made using SRIM-2013(Stopping Range of Ions in Matter) [175] using the Kinchin-Pease quick damage cascade model as suggested by Stoller et al [176]. Problems with the 'full cascade' model were discussed by Bratchenko et al [177], showing that it vastly overestimates the displacements per atom (dpa), and that the 'quick damage' model should be used especially when looking at reactor damage. The Stopping Range of Ions in Matter (SRIM) 'VACANCY.txt' output file gives total number of displaced target atoms per Angstrom depth for every incident ion, as a combination of vacancies by direct collisions from the incident ion and by recoils. The total vacancies formed were summed to give N_{Vac}, converted from Angstroms to cm for calculation. This was then converted to a dpa value

Implanted Ion	Implantation Temperature (˚C)	Implantation Energy (MeV)	Implantation Dose (ions/m^2)
Si	300	2.0 MeV	6×10^{15}
		1.0 MeV	4×10^{15}
		0.5 MeV	2×10^{15}
Si	750	2.0 MeV	6×10^{15}
		1.0 MeV	4×10^{15}
		0.5 MeV	2×10^{15}
Si	300	2.0 MeV	6×10^{14}
		1.0 MeV	4×10^{14}
		0.5 MeV	2×10^{14}
Si	750	2.0 MeV	6×10^{14}
		1.0 MeV	4×10^{14}
		0.5 MeV	2×10^{14}
Ne	300	1.45 MeV	9.37×10^{15}
		720 KeV	6.07×10^{15}
		350 KeV	3.71×10^{15}

Table 3.2: Irradiation Conditions

using Equation 3.4, where Γ_r is the total fluence of incident ions, and the atomic density of SiC is $\rho = 9.64 \times 10^{22}$atoms/cm^2.

$$N_{dpa} = \frac{N_{Vac}\Gamma_r}{\rho} \tag{3.4}$$

Displacement energies for SiC are reported at many varied values as seen in Table 3.3 with variations even across the common polytypes which causes wide ranges in dpa calculations. The standard provided values in SRIM are E_d = 28eV for carbon and E_d = 15eV for silicon, and these values were used for preliminary investigations. To be more consistent with other group members and with a majority of the literature [72, 178] values of E_d = 21eV for carbon and E_d = 35eV for silicon were then used. There was considerable difference between peak dpa found for these two different sets displacement energies with a peak dpa of 3.8 for the SRIM provided values and a peak dpa of 2.4 from the values used in the calculations in this project. This represents a big problem with this method to give accurate dpa values especially with the wide range of values seen in Table 3.3, it does however give a good estimation of dpa and depth range of damage and along with the exact fluence values is the best possible way of quantifying the damage induced in the material.

Polytype	Displacement Energy Si	C	Direction	Technique	Ref
6H	$< 30, < 60$		$[000\bar{1}]$	TEM	[179]
6H	30-35		Average	RBS	[180]
6H	$51 < E_d < 71$	< 58	-	PAS	[181]
6H	20		[0001]	PAS,EPR	[182]
6H	$< 43, < 85$		Average	PL	[183]
6H	19	18	$[000\bar{1}]$	PL	[184]
6H		22	Average	PL/MCL	[185]
6H	97		[0001]	TEM	[186]
6H	$35 - 120$	$24 - 64$	Across all directions	MD	[178]
4H	21	18	$[000\bar{1}]$	PL	[184]
3C	106	100	[110]	TEM	[187]
3C	23-38 [188]	54-90	Across various directions	TEM	[189]
3C	25		[001]	PAS,EPR	[182]
3C	18 , 35	22	$[\bar{1}\bar{1}\bar{1}]$	CL	[190]
3C	$36 - 135$	$21 - 71$	Across all directions	MD	[178]

Table 3.3: Literature Values for Displacement Energies in SiC

From the calculations a full depth profile prediction of the dpa for each ion implantation was produced. The high dose silicon implantation profile is shown as an example in Figure 3.3. A peak dpa for this implantation was given as 2.43 with an average of 1.49 dpa throughout the damage layer, with the damage expected to be within the first 1.32μm from the surface. Silicon ion implantations were also done with a 10× lower dose for good experimental comparison. The neon implantation was matched as closely as possible to the high dose silicon and the dpa comparisons can be seen in Figure 3.4a where the peak dpa is 2.42 and the average dpa through the damage layer is 1.51.

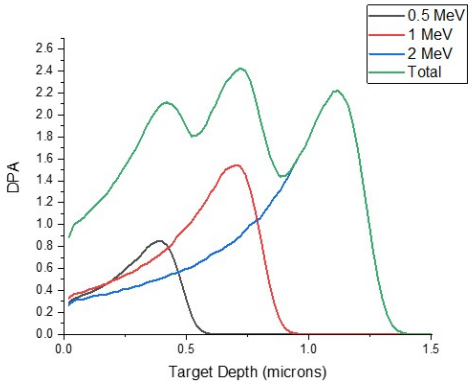
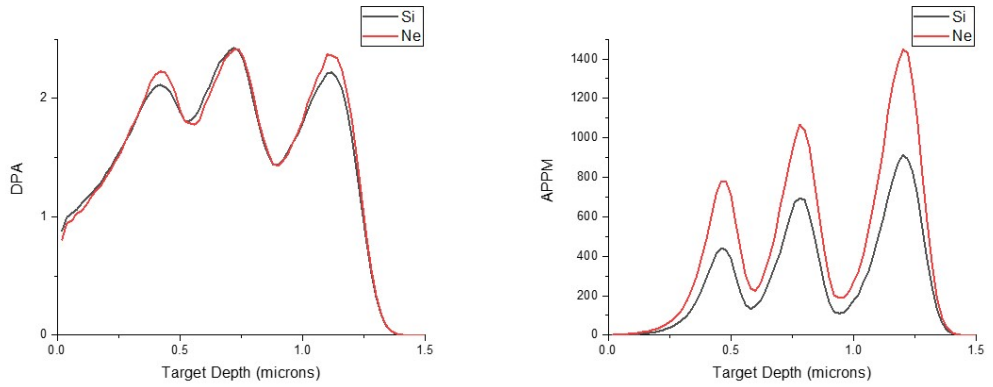


Figure 3.3: Depth profile showing predicted dose from high does silicon implantation, showing the separate individual energies and the combined total profile

In addition to dpa calculations SRIM was used to calculate how much additional Si and Ne was implanted into the samples to confirm that it was not sufficient to cause additional damage, in addition to being able to identify the location of the Bragg peaks. The 'RANGE.txt' file



(a) dpa **(b)** atomic parts per million (appm)

Figure 3.4: Depth profiles showing comparisons of high dose silicon and neon implantions for calculated dpa (a) and appm (b).

from the SRIM output provides the total number of incident ions per unit depth, N_{ions}. Using Equation 3.5 the total additional ions in appm (N_{appm}) was calculated.

$$N_{appm} = \frac{N_{ions}\Gamma_r}{\rho} \tag{3.5}$$

An average of 276 appm Si through the damage layer was calculated, with a peak of 914 appm Si resulting from the high dose implantation. For the neon implantation an average of 442 appm was calculated through the damage layer with a peak of 1447 appm. The full depth profile of both compared can be seen in Figure 3.4b. Where the damage profiles from the dpa calculations in both the Si and Ne match well, the higher fluences of the Ne ions needed to create the dpa result in a big difference in the additional appm of these ions in the irradiated materials. This is clearly one of the inherent problems with ion implantation techniques, whilst we are simulating dpa as a measure of damage in materials, under neutron irradiation there would be no additional atoms added into the structure, and the different types of ions need different total numbers of ions to create similar dpa values. Whilst we can quantify what we are adding in, we cannot separate the damage in the material from changes made by those additional ions.

3.8 Raman Spectrography

Raman Spectrography in this project was done using a JY Horiba LabRAM ARAMIS imaging confocal Raman microscope using both with a twin laser system of $532nm$ (green) and $633nm$ (red).

Raman scattering was first seen by C.V. Raman and K.S. Krishnan and published in 1928 [191] as a new form of secondary radiation seen as a true scattering effect rather than a fluorescent effect. The raman effect is seen where a monochromatic light is incident on a material, the frequency of a small fraction of the scattered light is shifted due to inelastic scattering of the photons by electrons or phonons in the material: the photons interact with the vibrating molecules in the sample [192]. This scattered light is very weak in comparison to Rayleigh radiation so monochromators with gratings are used to disperse unwanted scattered or stray light. The Raman scattered light is then collected on a multi-channel CCD to show its intensity and frequency.

Two types of raman scattering can occur: if the frequency of the incident light is higher than the scattered light, Stokes lines are seen; if the scattered light is of a higher frequency, anti-Stokes lines are seen. Stokes lines show transitions of phonons from a low energy state to a higher energy state and so are stronger than ant-Stokes lines, so Stokes lines are measured in Raman Spectrography [193]. Experimentally the frequency difference between emitted light to the incident monochromatic light is measured, and is measured as Raman Shift [191].

This technique is especially good for looking at various types of SiC. As SiC is a strongly covalently bonded material raman scattering easily occurs and allows probing of the various molecular vibrations in a sample. SiC and Si have a very well defined phonon lattice vibration which interact inelastically with incident light [194]. This then allows for clear and accurate qualitative SiC polytype analysis as well as more in depth quantitative analysis such as microscale residual stresses [195] and material disorder [196]. A positive shift in raman peaks indicates compresive stresses, negative show tensile stresses [197]. This technique has been used across the literature to probe different properties of SiC and radiation damage in SiC [184, 192, 198–202]. Raman can be an incredibly powerful technique, especially for looking at micron dimensions, in a way that X-Ray Diffraction (XRD) cannot [203]. It is however incredibly surface dependant, and defects in the unit cell at the surface of the material can prevent analysis of the material

below. In this project Raman was used as a simple tool for polytype analysis, and the full utility of the technique was not explored.

3.9 Sample Preparation

Samples for the majority of this project were commercially acquired though Goodfellow Ltd (Cambridge, UK) and were Direct Sintered, DS-SiC, Hot Pressed, HP-SiC and Reaction Bonded SiC, REFEL. Each material came in slightly different forms, but each was cut to $1mm$ thick slices with a maximum of $12mm$ in length. In depth characterisation of these materials is seen in Section 4.2. Additional material was fabricated as part of this project as described in Chapter 5. Samples of these materials were also produced with a thickness of $1mm$ for SEM and nanoindentation work.

Once samples had been cut to size they were ground until flat with diamond grinding plates down to a grit size of $15\mu m$ following this they were polished with successively fine diamond suspension in water, originally down to $1\mu m$, however after initial studies this was deemed to be not a good enough surface so later work was finished with $\frac{1}{4}\mu m$ diamond suspension. This surface was then used for ion implantations and other work.

Chapter 4

Room Temperature Studies

4.1 Introduction

With no fusion equivalent radiation source, experiments into radiation damage in fusion relevant materials is varied as discussed in Section 2.3. Self-ion implantation is seen as a good analogy for radiation damage as each ion behaves similarly to a Primary Knock-on Atom (PKA), as well as the technique being a quick, easy and relatively cheap way of creating damage. For these reasons it was deemed that ion implantation would be appropriate for this thesis. The flexibility available with ion implantation allowed different materials to be irradiated at different points through the project as described in Section 3.6, with varying conditions allowing for direct comparisons of conditions and damage on different materials to be made.

The initial work as part of this focused on characterising virgin material, to allow for comprehensive observations of micromechanical properties through nanoindentation of the effect of the ion irradiations. Initial ion irradiation studies were on three commercially acquired materials, Direct Sintered SiC (DS-SiC), Hot Pressed SiC (HP-SiC) and Reaction Bonded SiC (REFEL), however it was later deemed necessary to focus the work just onto DS-SiC so studies into this material are more in depth as some unirradiated material properties were investigated later into the project as further study became necessary.

4.2 Material Characterisation

4.2.1 Polytype Identification and Grain Structure Observations

Initial characterisation of materials was made using microscopy. Generally the grain structures of DS-SiC and HP-SiC were very difficult to observe, however Scanning Electron Microscope (SEM) images are shown in Figure 4.2 which show some of the grain structure features. In comparison REFEL has a very distinctive grain structure where SiC has grown into the silicon substrate from the initial SiC seeds. Figure 4.2c shows a comparison of the

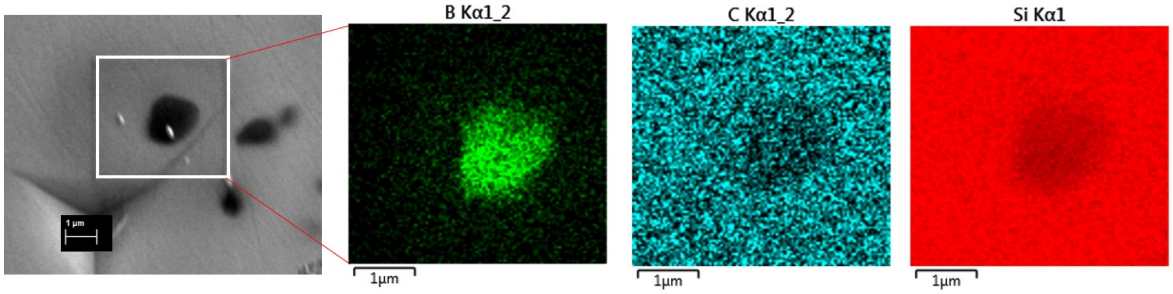
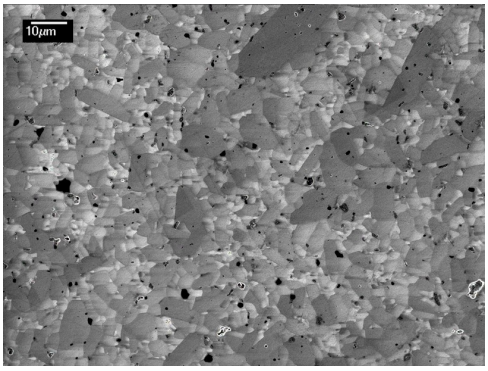
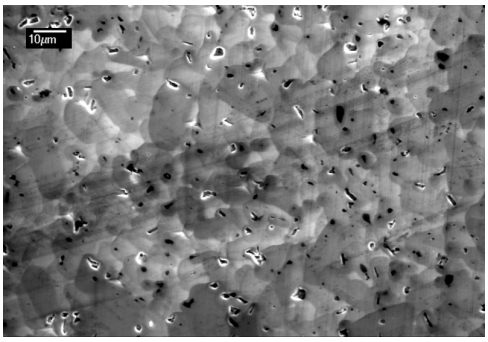


Figure 4.1: SEM image with corresponding Energy Dispersive X-Ray Spectroscopy (EDX) maps showing boron rich area.

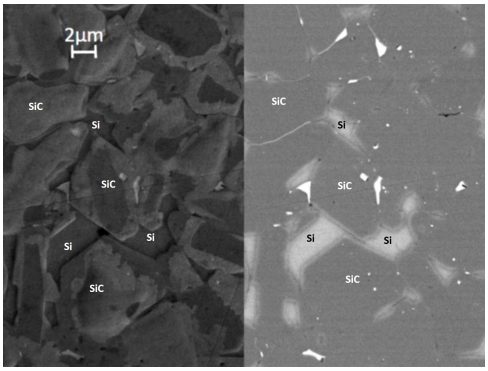
Secondary Electron Image (SEI) and Backscattered Electron Image (BEI) SEM images showing the different forms of SiC surrounded by the pure Si regions clear in the BEI image. It was not possible to do a full grain size analysis due to limitations with contrast in images, however it can be seen that the DS-SiC grain structure is split between grains of $\sim 1\mu m$ and larger elongated grains of mostly $\sim 10\mu m$. It was observed that there were darker grains or inclusions in grains present in the non REFEL which were then investigated, to check for contamination. Under EDX it was found that these were grain remnants of the boron sintering agent as seen in Figure 4.1, which are especially noticeable in later nanoindentation images. These were then able to be ignored as an inherent feature of the material and not additional contaminants. The grain structure of the HP-SiC is far less distinct but is mostly constituted from ovoid grains of $> 10\mu m$, and of a more even size distribution than that of the DS-SiC. REFEL is known to have a much more consistent grain size based on the initial size of the SiC particles before reaction bonding takes place, in this material grains are $\sim 5\mu m$ in width. It was hoped that Electron Backscatter Diffrac-



(a) DS-SiC



(b) HP-SiC



(c) REFEL

Figure 4.2: SEM images showing grain structure of different materials, with a comparison of the SEI and BEI images for the REFEL showing the silicon rich regiemes.

tion (EBSD) could then be used for further grain analysis, however while some grains produced acceptable kikuchi patterns and some produced none at all. This was not a surface dependant effect and prevented the use of EBSD analysis in this project.

One of the problems found when comparing various radiation damage studies in SiC is the various polytypes seen. While there are many techniques for polytype analysis, it was deemed that Raman Spectrography would be the most appropriate for this work. Raman Spectography was performed using a JY Horiba LabRAM ARAMIS imaging confocal Raman microscope on the DS-SiC material as discussed in Section 3.8. It was found that the DS-SiC is predominately a 6H-SiC, however there were traces of 3C-SiC also seen. The raman shift can be seen in Figure 4.10a, where the First Longitudinal Optical (FLO) and First Transverse Optical (FTO) peaks are clear [192, 202, 204–207]. It was also noted that the Raman peaks for the 6H-SiC were slightly shifted showing that the material contained some residual stresses from the manufacturing process.

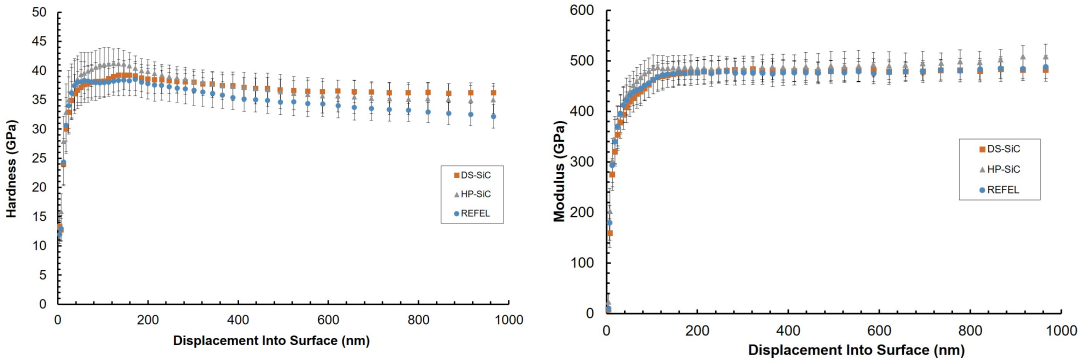
4.2.2 Nanoindentation

Initial nanoindentation hardness and modulus results for the three commercially available materials can be seen in Figure 4.3 and Table 4.1, showing the similarity of the behaviour between each material.

As seen in Figure 4.2c, REFEL has the most complex structure of the commercial materials. The large grains of Si within the material structure made nanoindentation a lot more complicated for this material as, in an array of indentations, some indentations would have part of a Si grain beneath the indenter, either obviously on the surface, or below the indentation but somewhere within the zone of plastic deformation beneath the indenter. An example of this type of indentation can be seen in Figure 4.4, where a low modulus is seen at the surface while indenting a silicon region, before rising to the bulk modulus value. It is expected that

Sample	Hardness (GPa)	Elastic Modulus (GPa)
DS-SiC	36.9 ± 1.7	480 ± 20
HP-SiC	36.5 ± 2.5	490 ± 24
REFEL	34.8 ± 2.1	477 ± 19

Table 4.1: Results from nanoindentation on virgin material samples.

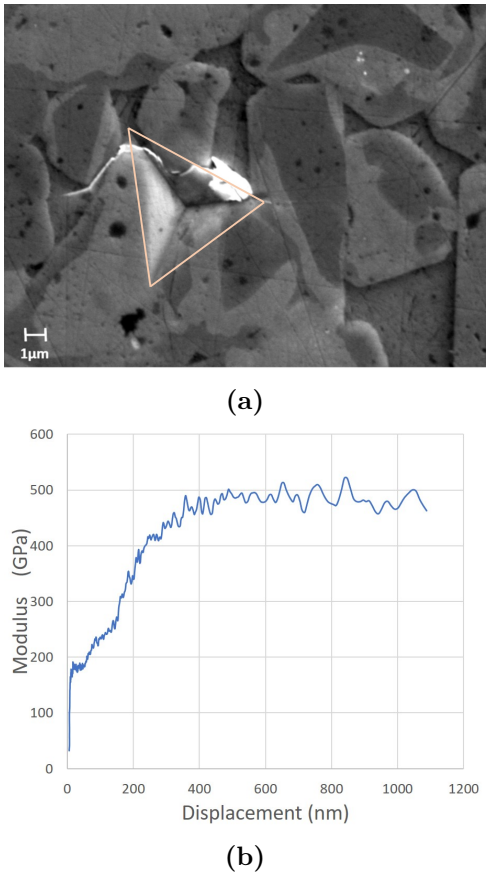


(a) Hardness **(b)** Modulus

Figure 4.3: Hardness and Modulus plots from nanoindentation studies on virgin DS-SiC, HP-SiC and REFEL, showing similarity of properties between commercially available materials. Standard deviations are given as errors.

all indentations in the REFEL material will have some pure Si within the elastic zone influencing the elastic modulus of all indentation data, this makes sense with regards to the bulk nanoindentation results where REFEL is seen to have the lowest hardness and elastic modulus. The indentations where Si is evident within the plastic zone however do not give a good representation of the bulk as the relative softness of the Si dominates the load/displacement curve. Due to this effect any indentation showing signs of a Si domination was excluded from the indentation array dataset. It is clear in Figure 4.3a, that the REFEL hardness is reducing with increased depth, this is likely as the deeper the indentation the more likely it becomes that pure Si is found somewhere within the plastic zone.

The behaviour of DS-SiC and HP-SiC under nanoindentation are seen to be very similar. An increase in hardness is seen at low indentation depths, particularly in the HP-SiC sample, this is due to the surface finish of the materials. For these early studies during surface polishing samples were finished



(a)

(b)

Figure 4.4: REFEL Modulus plot with corresponding SEM image of the indentation (indentation area outlined) showing effect of Si region on data.

with $1\mu m$ diamond, after these initial samples had
been tested it was decided that future material preparation would polish samples to $\frac{1}{4}\mu m$. The surface finish is clear when looking at the indentations themselves. In all these materials, other than this surface effect no indentation size effects were visible.

4.2.3 Nanoindentation Fracture

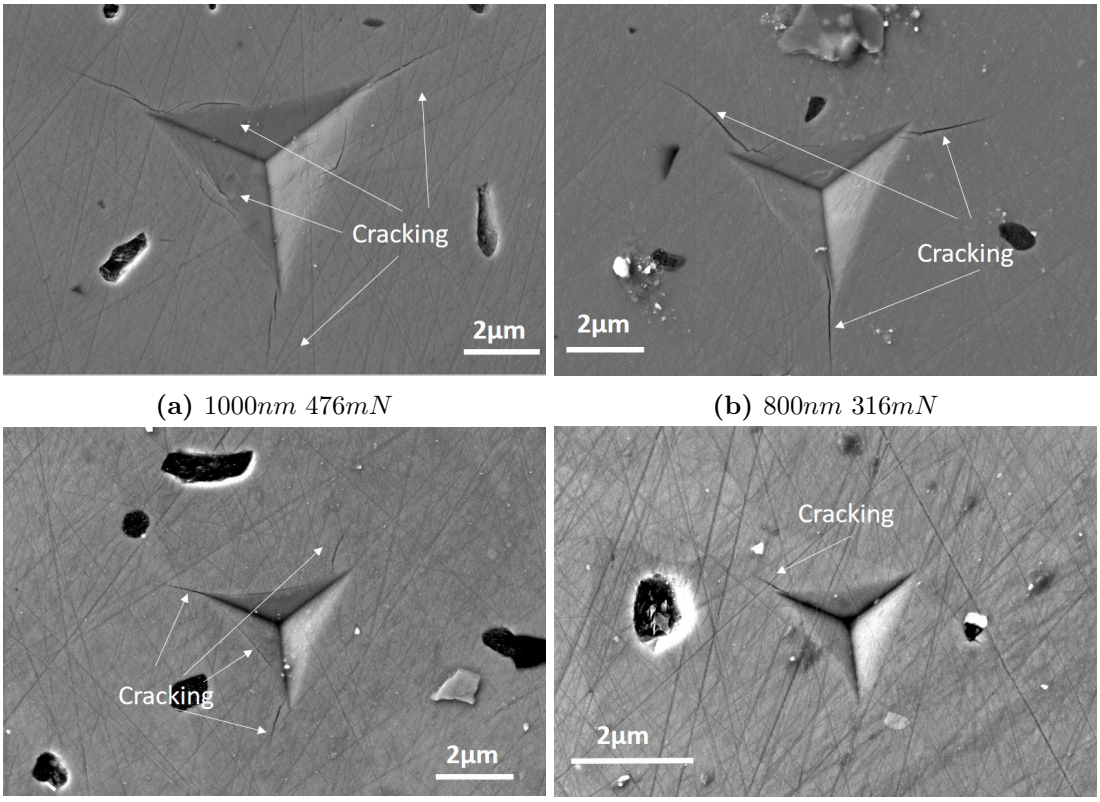
Some interesting effects were seen across all three material types post nanoindentation, namely the fracture behaviour of the material around each indentation. In the load profiles for each material no clear 'pop-in' events were visible however there was fracture around all indentations. The DS-SiC and HP-SiC showed similar behaviour with brittle fracture extending from the corners of the indentations and cracks evident laterally around the indentations and within the indentation surfaces themselves as seen in the DS-SiC example in Figure 4.5a. REFEL showed similar behaviour, however with a more varied and larger grain structure, and the fracture toughness differences between the SiC grains and the pure Si, some of the radiating cracks were often suppressed as seen in Figure 4.4a. Instead material push out is seen where the Si and SiC slip against each other at the grain boundary. Given the load profiles for all materials it was assumed that cracks were being initiated at the beginning of the indentation and there was then stable crack growth for the rest of the load cycle.

One of the simple techniques for calculating fracture toughness uses the measurements of cracks around indentations. The first method used evaluates fracture toughness K_{IC} using linear elastic mechanics [146, 208] (Equation 4.1)

$$K_{IC} = \kappa \left(\frac{E}{H}\right)^{\frac{1}{2}} \left(\frac{P}{c^{\frac{3}{2}}}\right) \tag{4.1}$$

where E is the elastic modulus and H is the hardness evaluated at maximum load P, c is the total crack length and κ is an indenter dependant constant of 0.016 for a Brekovich indenter. Schiffmann et al [209] performed a comprehensive analysis of different methods to determine fracture toughness by nanoindentation and the second method used was chosen as another simple calculation from measuring cracks around indentations [210, 211]

$$K_C = \kappa \left(\frac{a}{l}\right)^{\frac{1}{2}} \left(\frac{E}{H}\right)^{\frac{2}{3}} \left(\frac{P}{c^{\frac{3}{2}}}\right) \tag{4.2}$$



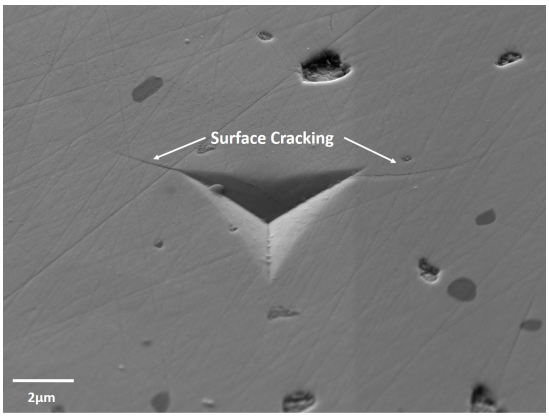
(a) $1000nm$ $476mN$ **(b)** $800nm$ $316mN$

(c) $600nm$ $181mN$ **(d)** $400nm$ $84mN$

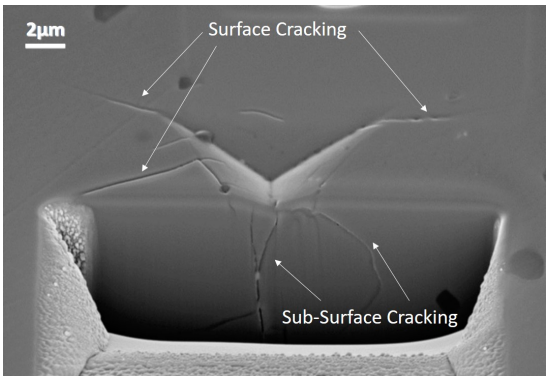
Figure 4.5: SEM images of indentations exhibiting fracture behaviour with indentation depth enhanced to show fracture clearly.

where a is the indentation size from centre to corner and l is the crack length from the corner, here $c = a + l$. From measurements on HP-SiC values for fracture toughness of $1.9 \pm 0.3 MPa.m^{1/2}$ from Equation 4.1 and $3.5 \pm 0.9 MPa.m^{1/2}$ from Equation 4.2. These values are very different, however both fit within the expected values from the literature [45, 48–53]. Despite this most recently acquired values fit more with the value given from Equation 4.2. As fracture toughness cannot be compared to irradiated material (Section 4.3.2), it was decided not to further pursue more accurate values.

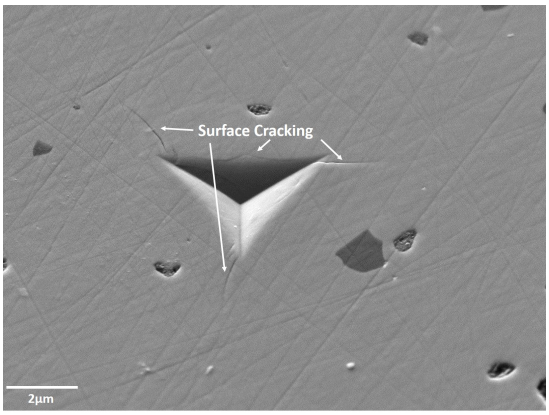
To investigate the onset of cracking around the indentations, further indentation was performed on DS-SiC with indentation depths varying from $100nm$ to the maximum of $1000nm$, in $100nm$ increments. These indentations were then carefully imaged with the SEM. Indentations of $300nm$ in depth ($47mN$) showed no fracture at all, however at $400nm$ ($84mN$) some of the indentations saw small radial fracture from one corner of the indentation. Lateral cracks around the edge of the indentation surface were not seen until depths of at least $600nm$ ($181mN$). Examples of these indentations can be seen in Figure 4.5. This shows that whilst there is no large



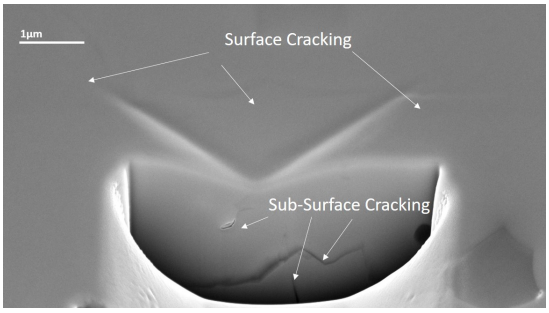
(a) 1000nm indentation



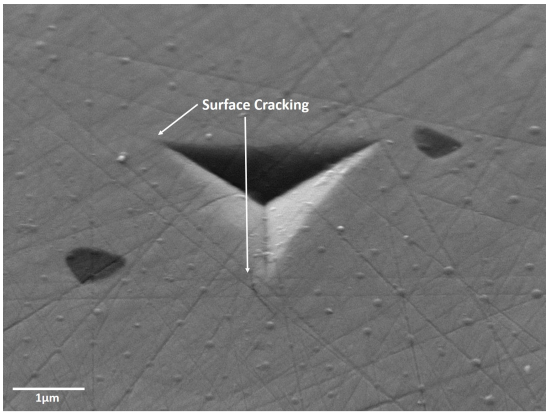
(b) 1000nm indentation cross section



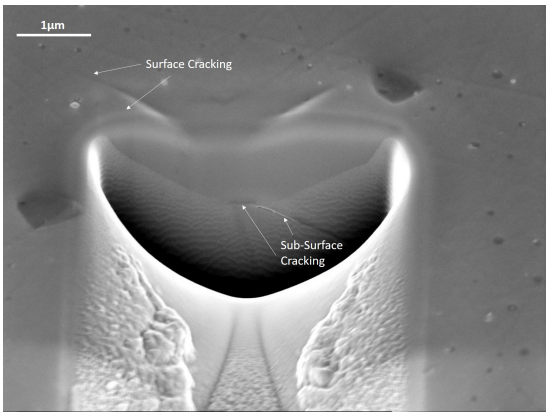
(c) 800nm indentation



(d) 800nm indentation cross section



(e) 500nm indentation



(f) 500nm indentation cross section

Figure 4.6: SEM images of varying depth indentations in DS-SiC with cross sections showing extensive fracture behaviour subsurface.

fracture event happening to initiate a crack, fracture is not being initiated until a certain load has been applied, and from that point there is gradual crack growth with increased load.

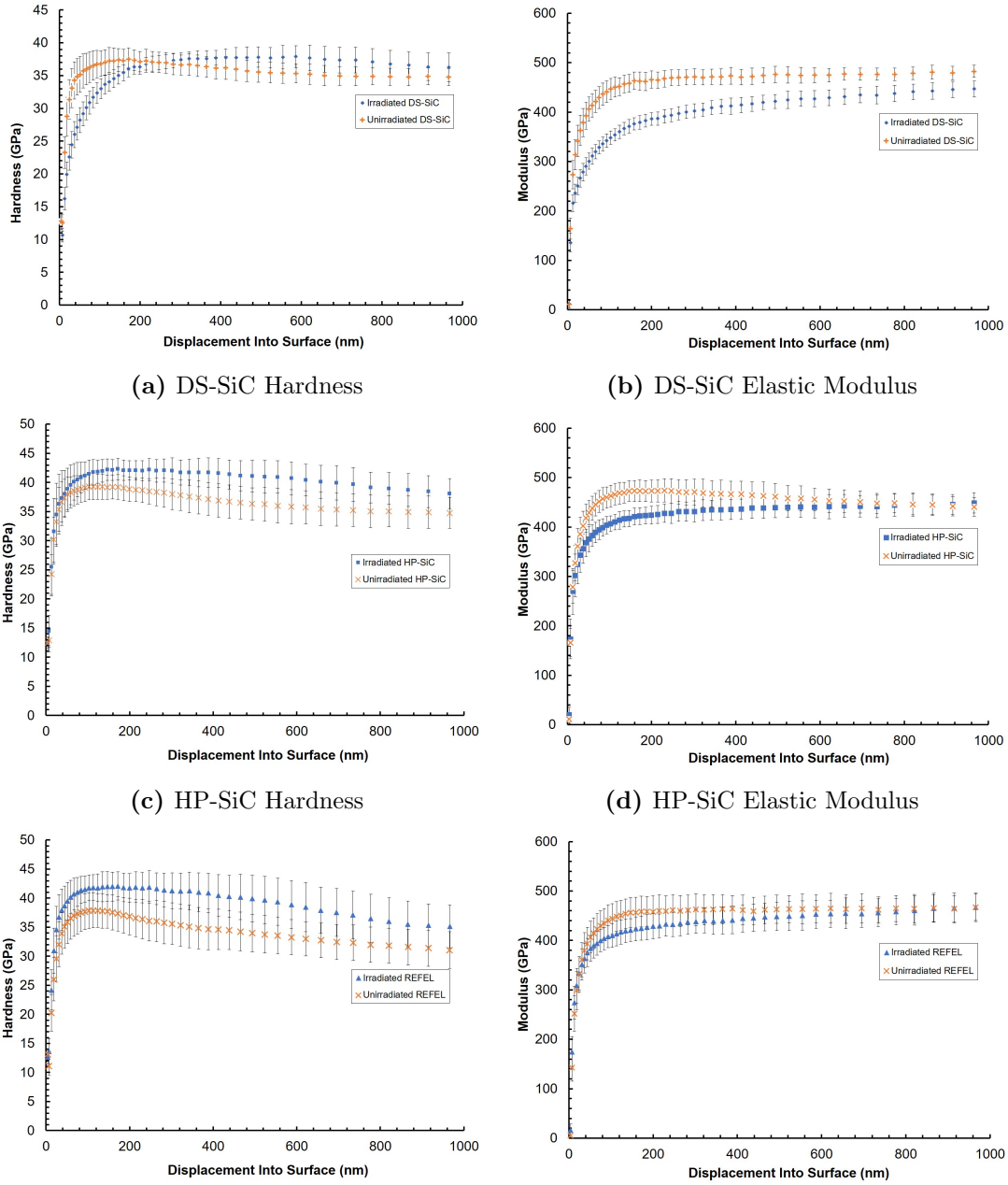
This fracture investigation was developed further by taking Focused Ion Beam (FIB) cross-sections through indentations of $500nm, 800nm$ and $1000nm$ as described in Section 3.5 to be able to observe sub-surface fracture and how it correlated to surface behaviour and examples are shown in Figure 4.6. Cross-sections of $1000nm$ indentations showed complex fracture behaviour occurring sub-surface, with cracks extending past the depth that could easily be observed with sensible size trenches ($> 8\mu m$ deep). This sub-surface cracking is seen to be far more complex than surface fracture, with interactions between cracks, although they do appear to be originating with the surface cracks. Unfortunately the FIB damage causes a complete loss of contrast showing the grain structure, so investigations cannot be more clear. In the process of creating the cross-sectional trench additional surface fracture also occurred, appearing to be a release of residual stress in the material or from the induced stress from the indentation itself. Similar sub-surface fracture was seen in the $800nm, 316mN$ indentation, with only a slight reduction in fracture complexity. The shallower $500nm, 122mN$ indentation also showed sub-surface, however it was much reduced, as would be expected by the less complex surface cracking, in addition grain boundary innteraction can be seen to influence the fracture behaviour like that seen in Figure 4.6d. The depth of cracks were still extending beneath the depths observable with FIB trenches due to the nature of FIB redeposition.

4.3 Silicon Ion Irradiation on commercially available materials

An initial Si ion irradiation was performed on all three commercially acquired materials, DS-SiC, HP-SiC and REFEL at 300°C to a peak of 2.4 displacements per atom (dpa) as described in Section 3.6.

4.3.1 Nanoindentation

Nanoindentation was performed on each sample that had undergone Si ion irradiation, with indentations performed on irradiated material and blanked out unirradiated material, allowing for direct comparison of just the irradiation effects, separately to any effects being held at temperature could have had on the samples.



(a) DS-SiC Hardness **(b)** DS-SiC Elastic Modulus

(c) HP-SiC Hardness **(d)** HP-SiC Elastic Modulus

(e) REFEL Hardness **(f)** REFEL Elastic Modulus

Figure 4.7: Nanoindentation Hardness and Elastic Modulus Plots showing effect of Si ion irradiation at 300°C to 2.4dpa on DS-SiC, HP-SiC and REFEL. Standard deviations are given as errors.

Each material type was seen to exhibit an increase in hardness and a reduction in modulus post ion irradiation, although each changed to a slightly different extent as shown in Table 4.2. A clear trend is seen where either the increase in hardness or the decrease in modulus is dominant. This effect in the REFEL sees the smallest decrease in modulus, most likely due to the areas of pure Si compensating for the lattice swelling in the SiC which causes the decrease in modulus. Simultaneously the defects caused by the irradiation are preventing plastic deformation to the material, and these are more dominant if the elastic properties don't increase to become dominant.

Plots showing the results of these nanoindentations are seen in Figure 4.7. It is noticeable that while the hardness for the materials shows a continued reduction with irradiation through the whole indentation depth, the elastic modulus plots show irradiated modulus trending back to the unirradiated values. This is expected as the irradiation depth was not large in comparison to indentation depth, the hardness values are only affected by the plastic zone, which will still be within the implantation depth at $1\mu m$ indentation depths, however the elastic modulus is affected by the whole of the elastic region which at depths of $1\mu m$ become dominated by the unirradiated bulk material beneath the ion irradiated layer. For this reason the reduction in elastic modulus calculated here will be an underestimation of the radiation damage effect if the whole bulk were to have been damaged.

4.3.2 Nanoindentation Fracture

One of the predominant features of the unirradiated material was the fracture behaviour especially with the increasing radial fracture growth from indentation corners. Indentations in the irradiated material however showed no radial fracture, although some lateral cracks were visible in the indentation surface, and example of which is seen in a DS-SiC sample in Figure 4.8a.

Sample	Hardness (GPa)			Elastic Modulus (GPa)		
	Unirradiated	Irradiated	% Change	Unirradiated	Irradiated	% Change
DS-SiC	35.7 ± 1.4	37.6 ± 1.3	5.38%	474 ± 12	421 ± 14	-11.2%
HP-SiC	37.0 ± 2.4	41.0 ± 2.4	10.59%	464 ± 22	439 ± 20	-5.39%
REFEL	33.9 ± 3.1	40.0 ± 3.6	16.76%	463 ± 27	448 ± 36	-3.22%

Table 4.2: Elastic Modulus and Hardness results from nanoindentation on samples irradiated to 2.4dpa 300°C also giving showing percentage change in properties from the unirradiated bulk. Average values for Hardness and Elastic Modulus were taken for depths of $300 - 800nm$

Clearly the radiation damage is suppressing crack initiation and growth, with this result consistent across all three material types. This result meant that nanoindentation fracture toughness could not be measured for irradiated samples using the methods outlined in Section 4.2.3.

At this stage it was decided to focus continued study just on the DS-SiC: the complex structure of the REFEL and its inherent problems with micromechanics meant that continuing with this was discounted; the HP-SiC and the DS-SiC performed similarly on the indentation work up to this point, however with less HP-SiC material available it was decided that further investigations and future irradiations would be done just on DS-SiC material.

Continuing on with the fracture investigations, cross sections of irradiated indentations were created using the FIB to compare behaviour with that found in the virgin material. Where in the unirradiated study extensive sub-surface crack networks were seen, additional surface cracks appeared due to releases in residual stress as shown in Figure 4.6b. When looking at the irradiated indentations investigations wanted to just show the effects from the indentation as much as possible, for this reason a thick layer of platinum was deposited on the surface, covering the indentation to prevent the release of the residual stress on the surface.

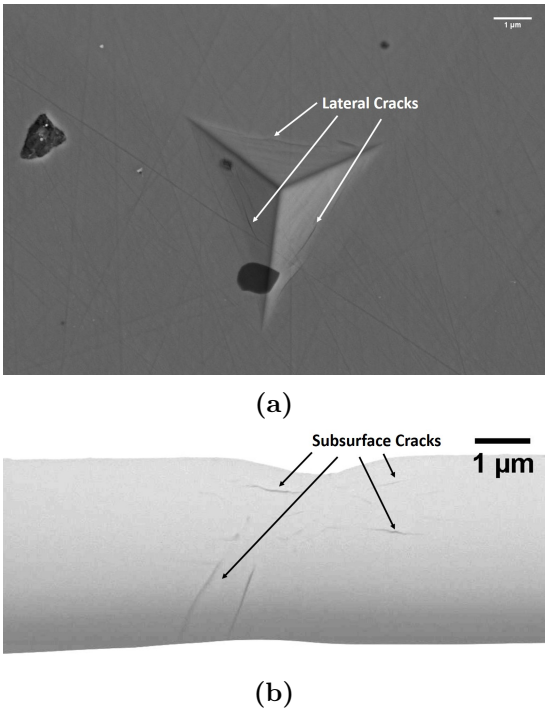


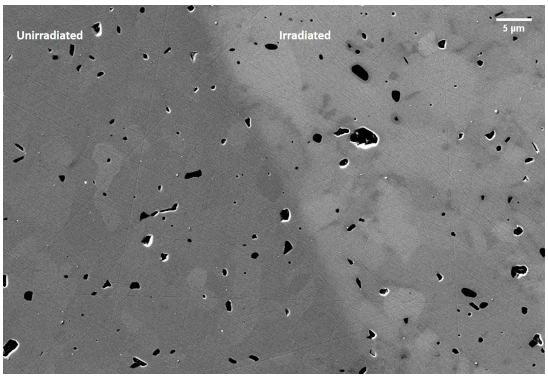
Figure 4.8: SEM images of indentations into irradiated DS-SiC showing (a)surface and (b) subsurface fracture . 4.8b shows a cross-section at 54° tilt of image (a) with a layer of platinum on the surface, it is enhanced to see as much of the microcracking as possible

Extensive fracture networks were still seen beneath the indentation in the irradiated samples as seen in Figure 4.8b showing that complex mechanisms are at work. With minimal fracture, and in most cases no cracking, seen in the thickness of the irradiated layer the fracture suppression from the radiation damage seems more complete. Instead the irradiated layer is acting as a thin film with cracks then extending into the bulk of the material. In some cases cracks were also seen horizontally along the interface of the irradiated material to unirradiated bulk, effectively beginning a delaminating process. The fracture

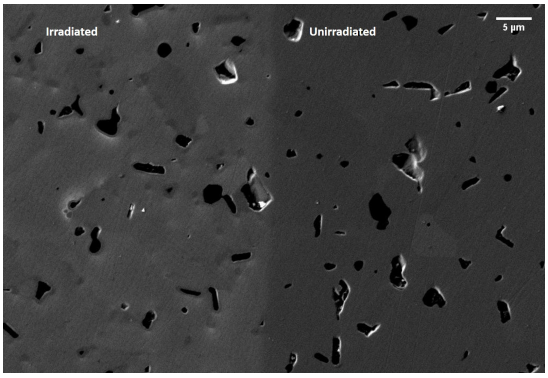
behaviour here is more complex than that seen in the unirradiated material with ragged extentions and branching behaviour seen. Such behaviour is similar to that seen by Park et al [95] in β-SiC. It is clear that the irradiated layer is acting in the same way as a thin film would on top of the bulk, so the stresses built up in the irradiated layer during indentation are dissipated through the bulk causing this extensive fracture behaviour underneath the irradiated material. With cracks again extending beneath the field of view it is difficult to directly compare the true extent of the fracture behaviour between indentations in the unirradiated and irradiated materials.

4.3.3 Damage Characterisation

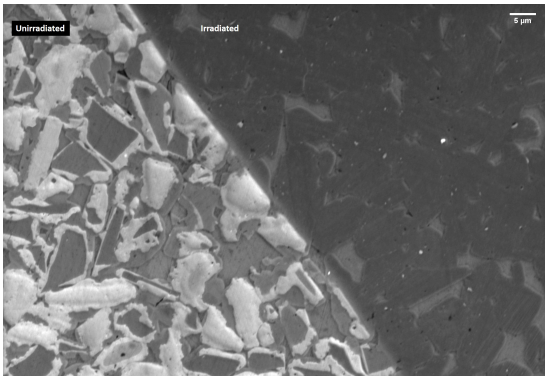
In addition to mechanical testing, further damage characterisation was possible using Raman spectrography. Before even this was necessary, however, there was a clear optical property change visible to the naked eye, with reduction in reflectivity clear between the irradiated section of the samples and the sections that had been blanked out during irradiation and therefore were unirradiated. This optical difference was also clear in the SEM. No grain structures of the SiC material was visible in any of the irradiated material on initial observations, on any of the materials types, with clear boundaries visible as seen in the in Figure 4.9. The REFEL sample is particularly interesting as the ion irradiated section on the right of the image looks very similar to the BEI seen in Figure 4.2c, although it is all a SEI image. The DS-SiC and HP-SiC boundaries are less distinctive, but still clear, and show a reduction in the definition of grains in the irradiated material.



(a) DS-SiC boundary



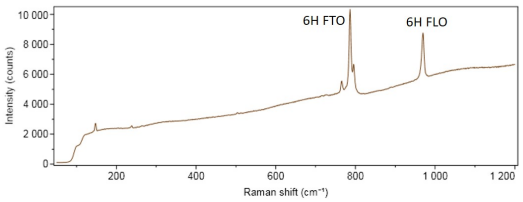
(b) HP-SiC boundary



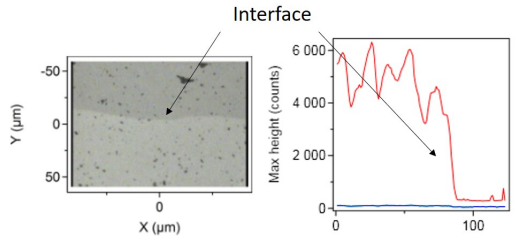
(c) REFEL boundary

Figure 4.9: SEM images of boundaries between the unirradiated and irradiated material.

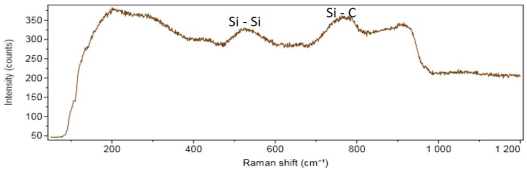
With optical damage clear the next step was to look at the spectrum produced by raman spectrography. With this technique being so useful at identifying SiC polytypes when characterising material it was deemed a good technique to use for looking at effects post irradiation. As seen in Figure 4.10 the Raman signal intensity on the irradiated sample was much reduced, with none of the distinctive SiC polytype peaks visible, instead very broad Si-Si and C-C bonds are seen as well as a broad Si-C peak where the FTO was clear in the unirradiated signal. This seems to imply an amorphisation of the material due to the radiation damage [212–215]. This raman effect is congruent with the literature , however the literature also concludes amorphisation is not expected as the dose and temperature do not match the critical point where amorphisations have previously been seen. It does however fit with observations from SEM images where grains are less visible.



(a) Unirradiated Raman Signal



(b) Raman intensity change across boundary

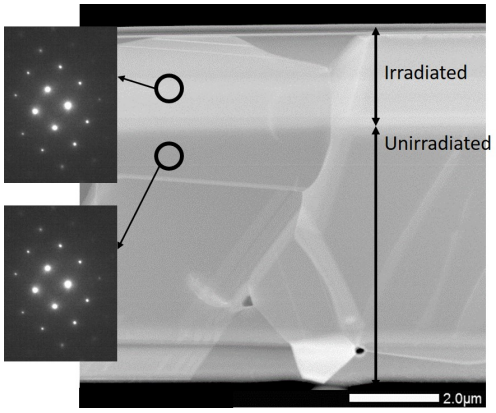


(c) Irradiated Raman Signal

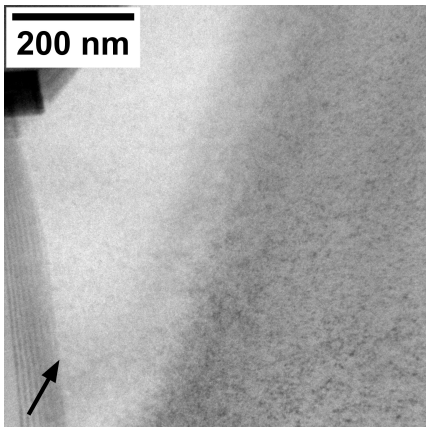
Figure 4.10: Plots showing change in raman signal between unirradiated material and irradiated DS-SiC

With this result not making obvious physical sense along with not being congruent with the literature it was decided that further observations were needed using a Transmission Electron Microscope (TEM). Lift outs were made in a clean area of the irradiated material to a depth which would show both the irradiated layer and the unirradiated bulk[1]. Looking at the first of the lift outs in the Scanning Transmission Electron Microscope (STEM) a distinctive change in electron transmission is seen showing the implanted layer, in the same way as it was seen both optically and in the SEM, however it was clear that this area was not amorphised as all of the grain structures continue into this layer, and there is also evidence of twinning seen in the top irradiated layer as shown in Figure 4.11a. This was further confirmed by taking a diffraction pattern in the same grain in both the irradiated layer

[1]Operation of the TEM was performed by J. Haley and Y.Zayachuck as it was not possible to be trained to use the equipment



(a) STEM image showing grain structure of cross section with difference between irradiated layer (top) and unirradiated bulk. A diffraction pattern from both sides of the interface showing no change in crysal structure between unirradiated and irradiated material.



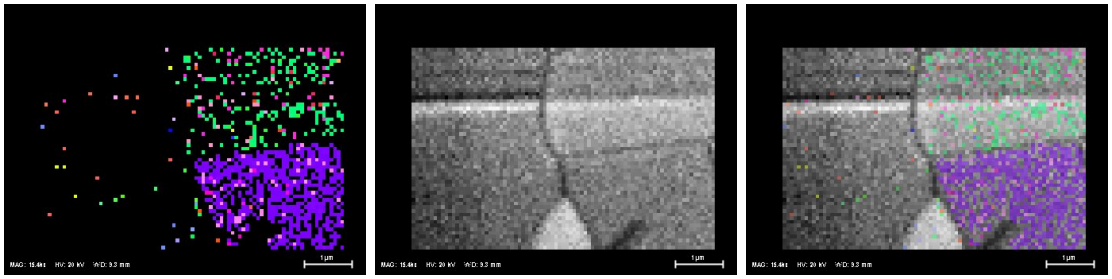
(b) TEM bright field image in $01\bar{1}1$ condition, lhs is unirradiated material and rhs is irradiated showing large increase in defect density

Figure 4.11: TEM images showing boundary between unirradiated bulk and irradiated layer and the changes in properties between the two.

and in the unirradiated layer which is shown to be identical and completely crystalline. This effect was seen to be consistent between multiple lift-outs confirming that another mechanism is in operation causing the anomalous result in the raman spectrography. The clear boundary between the implanted surface layer and the unirradiated bulk meant a true depth of damage was measured as $2.11\mu m$, significantly deeper than the $1.5\mu m$ predicted with Stopping Range of Ions in Matter (SRIM). This likely also means the peak dose is less than the 2.4dpa, as the damage will be spread over the larger distance.

Further TEM investigations were then made, looking to qualitatively investigate the cause for the various radiation damage effects. It was found that there was a large increase in defect density in the irradiated material which is shown in Figure 4.11b, as is consistent with radiation damage studies across all nuclear materials. Quantitative analysis of dislocation densities here was deemed to be outside the scope of the project, but the qualitative images provided insight into the raman results as the increased dislocation density may have been reflecting the light for the raman at a higher rate preventing the laser from penetrating the material to obtain a spectrum.

It was hoped that Transmission Kikuchi Diffraction (TKD) would also help to give further insight into these microstructural changes caused by the radiation damage, however this technique proved unsuccessful with these samples, an example of this is shown in Figure 4.12. In a



(a) IPFZ **(b)** PQ **(c)** PQ and IPFZ

Figure 4.12: Images showing problems with TKD. The Inverse pole figure z-direction (IPFZ) and Pattern Quality (PQ) images and their combination showing how some grains are able to have adequate quality, but others are showing no signal.

similar way to when some initial characterisation was attempted with EBSD some grains gave some signal and other grains gave no signal at all, and even with the grains which gave some signal the signal was not sufficient to provide adequate Kikuchi patterns for any significant analysis. What was seen was intensity in signal shift giving 3 more intense stripes through the material in the irradiated region that seem to correspond to the areas of large Si doping from the implantation as predicted in Figure 3.4b. If a clearer TKD signal had been possible it may have been feasible to use the actual depth of irradiation as seen in the STEM along with the depths of these intensity peaks to correlate the expected atomic parts per million (appm) and therefore calculated dpa to give a better damage profile for the three energy implantations, however with the TKD failure seeming to be intrinsic to the material this was not possible.

4.4 Comparative ion irradiations into Direct Sintered SiC

Additional irradiation studies were carried out on DS-SiC to allow for direct comparison of the effects of radiation damage across a range of irradiation conditions, as well as a comparison of the self ion implanted material with that of a neon ion implantation. With temperature and fluence the varying parameters as outlined in Section 3.6 all other factors were kept as constant as possible.

4.4.1 Nanoindentation

The comparison of these irradiation conditions was focussed on nanoindentation studies. On each sample, arrays of 64 indentations were made both on the blanked unirradiated material and on the irradiated material. Percentage differences between the elastic modulus and hardness

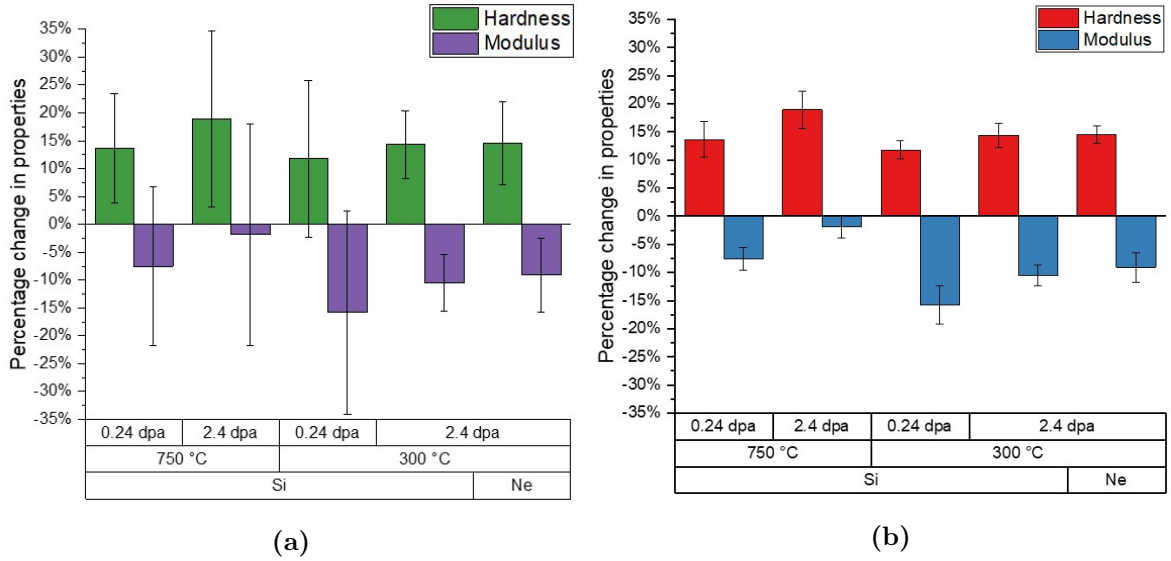


Figure 4.13: Plots showing the relative difference between unirradiated and irradiated materials for elastic modulus and hardness across all irradiation conditions. 4.13a shows error propogated from standard deviations on data sets for each sample, 4.13b shows error as the standard deviation of the mean of those data points between the depths of $300-800nm$ for hardness and $50-200nm$ for elastic modulus.

results showing the effect of the various levels of damage were taken and are shown in Figure 4.13 while absolute mean values are seen in Table 4.3. This also allowed for comparison between the unirradiated samples exposed to the different temperatures for various lengths of time showing slight changes in these properties from the original virgin material. The absolute mean values are taken form depths of $300-800nm$, as are the percentage differences for hardness, however the percentage difference modulus values are taken from depths of $50-200nm$. Where in the results in Section 4.3.1 the elastic modulus gradually tends back to the bulk value due to the whole of the elastic zone influencing the elastic modulus, in some of the implantation condition data sets this is occurring at lower depths after, especially in data further looked at in Chapter 5. To allow for the best possible comparison of data, and as the largest difference in elastic modulus is seen at lower depths, the range of $50-200nm$ was chosen to give a better idea of the effect of the various irradiation conditions on the change in elastic modulus.

In addition to this a further investigation into errors on the change in hardness and elastic modulus were needed for quantifiable comparisons to be made between irradiation conditions. Historically standard deviations as errors on nanoindentation plots have only been seen in the depth hardness or elastic modulus plots, however these seemed insufficient for the comparisons required here. The plots in Figure 4.13, show a comparison of two different propagations of

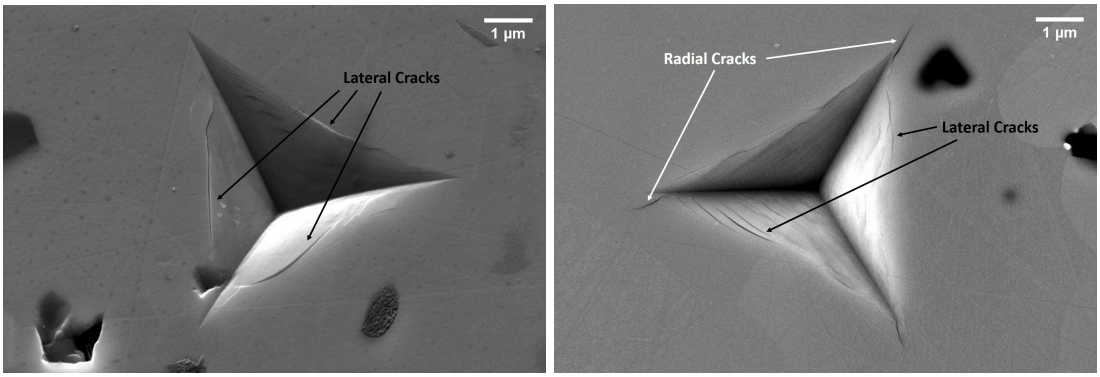
standard deviations on the data. The first method used as shown in Figure 4.13a gives an error as the propagated standard deviation of the average value for the data calculated at each depth. With the standard deviations on these data sets often intersecting between the unirradiated and irradiated data sets for each sample as seen in Figure 4.7, this method gives large error bars on the data, which clearly overestimate the error, but gives a true representation of the variance across all indentations. Figure 4.13b shows error as the propagated standard deviation of the mean of the data points at the desired depths. As the irradiated samples are consistently harder through the whole depth, and the elastic modulus is consistently lower through the depth measured this biases to that conclusion, although overall underestimates the error. The overall trends of the data however are clear and do allow for good conclusions to be made.

It is noted that the 300°C 2.4dpa Si ion irradiation used for this analysis is different to that used in Section 4.3.1, and comes from the latter irradiation run to these conditions. This sample had a better quality surface preparation, and the nanoindentations were run across the same time-frame as the samples it is compared to. While nanoindentation technique improved during the project, these latter indentations exhibited some issues which the earlier ones did not. The same indenter tip was used throughout this project, and while area function calibrations were performed regularly, as the tip became blunter accurate calibrations at for low indentation depths became a problem. This is especially evident in the large standard deviations seen in the data, especially the elastic modulus data.

Silicon Ion Irradiations

Initially looking at the increase in hardness seen, as expected, across all irradiation conditions a clear trend is visible. The increased dpa at both temperatures is causing an increased hardening effect, with the 300° implantations not just showing less of an increase in hardness in total than the higher temperature implantation, but also a lesser degree of hardening with higher dose. The largest hardening effect, that after the 2.4dpa 750°C irradiation, is of $\sim 19\%$.

In contrast to the hardening effects, the modulus trend follows slightly differently. Both irradiation temperatures are showing $\sim 5\%$ more reduction in modulus with higher dose. The effect of the radiation damage at the higher temperature is also having less of an effect than at the lower temperature, at both doses, however the uncertainties associated with these reductions



(a) 750°C 0.24dpa **(b)** 750°C 2.4dpa

Figure 4.14: SEM images of indentations and their different fracture behaviour at 750°C enhanced to show fracture clearly.

in modulus are greater, the trends, especially at low dose, are clear. The trend of the data to return to the bulk values do show some slight changes in rate under different irradiation conditions, however with the problems with error discussed quantifying these changes at this stage is not possible.

Neon ion Irradiation

It was decided that to accompany the self ion implantations a noble gas ion implantation would allow for a good comparison of behaviour without introducing excess silicon so not changing the bonding and structure of the sample, so a neon implantation, matched as close as possible to the silicon ion implantation was performed. This implantation was otherwise in identical conditions to the Si ion implantations, again at the Surrey Ion Beam Facility. In the same way as for all other irradiated samples nanoindentation was performed with results directly compared to the Si ion 2.4dpa 300°C results. It is clear from Figure 4.13 that the increase in hardness and the reduction in elastic modulus are very similar to that created from the Si implantation, although the effects are slightly smaller this effect is negligible.

4.4.2 Damage Characterisation

In the same way as all other irradiated samples, an optical difference was clear between the unirradiated and irradiated areas of the samples, and surface fracture was suppressed under all irradiation conditions. The effects on surface fracture in the 300°C conditions were all

Irradiation Conditions			Hardness (GPa)			Elastic Modulus (GPa)		
Ion Type	Temperature (°C)	Dose (dpa)	Unirradiated	Irradiated	% Change	Unirradiated	Irradiated	% Change
Si	300	0.24	40.3 ± 3.6	45.0 ± 3.5	11.8%	475 ± 29	465 ± 37	−15.8%
Si	750	0.24	37.6 ± 2.9	42.7 ± 1.8	13.6%	468 ± 20	453 ± 14	−7.6%
Si	300	2.4	36.4 ± 1.5	41.7 ± 1.8	14.6%	473 ± 13	444 ± 14	−9.1%
Si	750	2.4	34.8 ± 5.0	41.4 ± 1.8	18.9%	446 ± 53	438 ± 13	−1.8%
Ne	300	2.4	34.9 ± 1.5	40.0 ± 1.1	14.3%	475 ± 11	448 ± 10	−10.5%

Table 4.3: Elastic Modulus and Hardness results from nanoindentation on DS-SiC also showing percentage change in properties from the unirradiated bulk. Average values for Hardness and Elastic Modulus were taken for depths of $300 - 800nm$. Hardness percentage change taken from depths of $300 - 800nm$, elastic modulus percentage change taken from depths of $50 - 200nm$

qualitatively the same, with only evidence of lateral cracks in the indentation surface. In contrast the 750°C samples showed a more visible grain structure in the SEM, the 2.4dpa sample also showed small amounts of radial fracture. A comparison of two 750°C indentations from the different doses are shown in Figure 4.14, showing the small radial cracks extending from the indentation corners in the 2.4dpa sample and the lateral fracture across the indentation surfaces.

In addition a further TEM lift-out was made from the neon implanted sample to make a qualitative analysis of the damage made and see how it compared with the self-ion implanted material. A dark field image is seen in Figure 4.15 again showing the boundary between the unirradiated bulk and the irradiated layer and a similar defect density to that seen in Figure 4.11. No bubbles were obvious in any of the neon irradiated material at this stage.

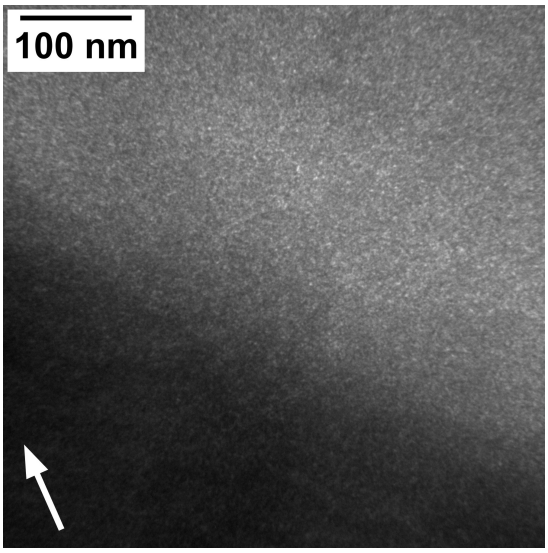


Figure 4.15: Dark Field TEM in $1\bar{2}10$ condition image showing increased defect density in the irradiated layer (top of image) of neon ion implanted material

4.5 Discussion

A vast range of radiation damage experiments into different forms of SiC have been performed in the literature as discussed in Section 2.3, however direct comparison of those studies has always been a challenge. The work here has allowed direct comparison of material irradiated by various ion implantation conditions to allow for such analysis and therefore allow for more accurate conclusions on ion irradiation damage effects.

The various polytypes of SiC complicate studies somewhat, however here three commercially available were studied under the same ion irradiation conditions. The most noticeable result across DS-SiC, HP-SiC and REFEL, was the suppression of crack propagation from indentation corners. Numerous studies into fracture toughness from nanoindentation in unirradiated SiC materials with extensive surface and subsurface cracks evident in both single crystal [216] and polycrystalline material [217] have previously been made. With the unirradiated SiC studies come conclusions about the large volume of material around indentations effected by the plastic

zone with early studies saying the plastic region around an indentation may be > 5 indentation radii [218]. This study found a complete suppression of radial fracture in all material examples except the 750°C high dose example. Tandon et al's study [147] also saw a suppression of surface cracking after ion incidence, postulating that crack nucleation at intersecting shear faults within the deformation zone is still occurring, but the residual stresses on the surface are preventing cracks from opening on the surface. This is in contrast to the study by Park et al [99], where they successfully used fracture from around nanoindentation in dual beam irradiated β-SiC to calculate fracture toughness values, and also Nogami et al's [101] study into polycrystalline Chemical Vapour Deposition (CVD) where similar measurements are made. This was clearly not possible in this work. While further investigations are needed to look further into the cause of this effect it is likely that residual stresses, amplified by the ion implantations, are acting to obstruct crack propagation. As discussed in Section 2.4.2, there are many different mechanisms at play which contribute to crack formulation under nanoindentation. It appears that sub-surface the layer of irradiation damage, with its reduction in modulus, for example from 473 ± 13GPa to 444 ± 13GPa in the 300°C 2.4dpa experiment, is due to increased lattice strain, and acting as a thin film. This then allows for crack nucleation at the interface, and crack propagation from the lateral cracks in the indentation surfaces themselves to be amplified into the unirradiated bulk, the effects of which are clear with the cross-sectional indentation images. Another mechanism is coming into effect with the high dose 750°C irradiation condition, in the 750°C studies there is more energy in the system which is both releasing some of the residual stress though a self-annealing process, and allowing for greater mobilisation of any point defect or vacancy obstructions allowing for some radial fracture to form. The low dose 750°C sample is not at temperature for a long enough period of time for either of these process to take hold as the dose rate of all ion implantations was kept as constant as possible. It does seem that the formulation of fracture is a mixture of what would be expected from the Hertzian contact model, where these de-lamination effects could be seen as the underneath of the Hertzian cone, in combination with Ostojic et al's description of what is occurring under a sharp Berkovich indenter [144], where cracks are initiated at the tip and the corners of the indenter in brittle materials like those in this study. Where cracks are suppressed on the surface it would seem that ion irradiation has induced some compressive stresses in the damage layer, and the tensile

stresses required to nucleate cracking are unable to spread through this regime.

It is well known from the literature that radiation damage creates an increase in hardness and decrease in elastic modulus, and this was consistent in this work, for example the 300°C 02.4dpa experiment showing an increase in hardness by 14.6% and a reduction in elastic modulus by 9.1%. The extent of these effects is known to reduce and and eventually reverse as irradiation temperature increases [101] again due to the self annealing effects occurring during these high temperature irradiations. The consistency of this effect in the elastic modulus in DS-SiC as seen in Figure 4.13 allows this work to fall well within the literature for comparisons with other work. Here it is known that reduction in the stability of the defects at higher temperature is allowing for a reduction in lattice strain, a reduction in swelling, and the smaller reduction of modulus with temperature and duration of implantation, as exemplified by the 750°C 2.4dpa indentation results with a decrease in modulus by only 1.8% . In comparison to this the largest increase hardness was seen in this same test with an increase of 18.9%. This result is less consistent with the literature and perhaps shows the difference here between the cheaper, less dense DS-SiC material obtained for this project and the better denser, purer material used in the literature, mostly CVD SiC. Another difficulty with the hardness values is that none of the studies which look at nanoindentation in the literature are doing so on material that has been purely Si ion irradiated, instead either single or dual beam He ion implantations are looked at. The effect of helium in the material is significant, and changes the defect behaviour considerably with the addition of He bubbles within the damage layer [67,71,93,96,99,101,123,124,219,220]. When helium damaged material undergoes the self annealing process an intrinsic softening of the material occurs. These mechanisms do not occur in this work's Si ion irradiation, instead with the mobilisation of defects and vacancies allowing for a recovery in elastic modulus, they are producing larger defect clusters which is likely increasing the increase in hardness.

It is of note that the unirradiated material having been exposed to the higher temperatures for varying periods of time also exhibited some minor changes in material properties. The elastic modulus and hardness of the DS-SiC were seen to reduce by a small amount with temperature, $\sim 6GPa$ for the low dose sample, only held at temperature for a short time, and $\sim 30GPa$ for the higher dose sample held at temperature for a longer period of time. This effect could be a general effect caused by less accurate calibrations of the diamond area function of the indenter

tip as it became more blunt with use, however the correlation to temperature could point to another cause. As is seen in the irradiated samples a small amount of self annealing is occurring while the blanked section of the sample is held at temperature during the irradiation process. This is changing the intrinsic properties of the material to a small degree. For materials to be used in a fusion relevant environment a better knowledge of their behaviour at temperature, and after being at temperature is required.

It may have been expected that the neon ion implanted material would have behaved similarly to other inert gas ion implantations, namely helium, with the damage it caused the the DS-SiC, however this was not the case. The elastic modulus and hardness changes were almost identical to that of the silicon ion irradiation results from the same 300°C 2.4dpa conditions. This result shows that neon is a good inert analogy for silicon self ion implantations. The hope when implanting with the neon is that the implantation can simulate a better idea of realistic fusion damage with the combination of the heavy ion acting similarly to the PKA, and as a noble gas it can also simulate some of the effects the addition of helium into the system will make, without adding additional interstitials into the material by a dual ion irradiation although this has not been seen in the 300°C study here. At this stage it appears that neon bubbles have not been created during this irradiation, although more in depth TEM work would need to be carried out to confirm this.

In depth microstructral investigations were not possible in this project, due to lack of accessibility to equipment, however the optical change in the irradiated materials could not be ignored. The optical change in all the irradiated material shows an intrinsic change to the sample, in a similar way to the changes seen in elastic modulus. Clear changes to the material surface both optically and in the SEM as well as in the cross sections seen in the TEM were seen. This is likely due to the lattice swelling caused by the induced defects, and the corresponding lattice strains. This optical effect was initially thought to show that amorphisation had occurred, as raman is a depth dependant spectography technique and showed clearer Si-Si bonds than Si-C bonds, however better imaging later in the project showed grain structures still visible on the surface of DS-SiC. The reduction in intensity and broadening of the raman peaks, along with the introduction of Si-Si bonds not visible in the unirradiated material seemed to support a conclusion of amorphisation, however this is not the case. The literature looking at

raman spectrography and the changes in peaks with irradiation often conclude, with identical spectra to those seen in this project, that amorphisation has occurred as seen in Ning et al's work [221]. Instead the defects in the material are preventing the laser light from penetrating the surface of the material fully, and are scattering the light back at a much reduced intensity which only allows the basic bonds in the material to be seen. The Si-Si bond is most clearly seen as the ion implantation has increased the appm of silicon in the material, creating a large number of silicon interstitials, this in turn has effected the stoichiometry of the sample showing the result in the raman spectra. Results like this are also concluded in the literature, with Zang et al [222] concluding similar non-amrophisation effects with comparable irradiations to this work. What is clear however, is that some studies are using these low intensity broad raman peaks to conclude the material is amorphous and this is not always the case [221, 223]. The complementary TEM work taken place in this study allows for a more accurate conclusion to be made, that the vastly increased defect density, along with lattice swelling has caused these optical changes. The optical changes are also less clear in the DS-SiC irradiated to 2.4dpa at 750°C than at the lower temperature, showing a correlation with the lesser effect on the elastic modulus. This correlation gives more weight to the nature of the damage causing this effect. The assumes lattice strains from the defects caused will have changed the vibrational nature of the lattice. The optical nature of any material depends on how the vibrations of the phonons in light are able to interact with the lattice vibrations, with an intrinsic change to the lattice vibrations the refractive index of the damaged material is changed, causing the change in reflectivity of the material surface.

One of the aspects which could not be fully investigated was the statistical relevance of the changes seen here. In an ideal situation an ANOVA two-way type analysis would have been performed, however the way that the data was assembled by the software did not allow for the size of the data set to be obtained. The software automatically produces mean hardness and elastic modulus values across certain depths, with corresponding standard deviations, and further collates data from across different indentation runs to produce the data given to the user. Historically this has not been a problem as work required merely comparing two sets of data, but in this work where direct comparison to see if data sets fall within the same statistical variance it is much more important. This prevents users from being able to perform further

statistical analyses such as the aforementioned ANOVA analysis.

4.6 Summary

This study has shown that effects of Si ion implantations into commercially available materials produce consistent reduction in elastic modulus and increase in hardness. Key results from these studies are numerous. The suppression of fracture in the irradiated materials is of particular interest, how this may relate to the changes in optical properties, and how the defects produced in the material are directly causing these changes.

The materials under the conditions studied here do not become amorphous at any stage, although the increased defect density causes the optical change with a reduction of intensity of raman spectra and a clear boundary between the unirradiated and irradiated material is seen both in the SEM and TEM.

Neon and silicon ion irradiations made under the same conditions appear to produce very similar micromechanical changes in DS-SiC. This similarity between the neon and silicon implantations is also of particular relevance as it could provide better insights into both bubble formation and the effect of silicon PKAs in a single implantation experiment.

Another particularly interesting aspect from this study is how the effects of the ion irradiations at higher temperatures differ from that at low temperature, especially with respect to the fact that self-annealing may have been occurring during the implantation. This is of particular relevance when looking to in service behaviour of materials.

Chapter 5

Material Fabrication and Characterisation

5.1 Introduction

Part of the project allowed for expanding the original remit to allow for collaborative work to take place. Having looked at various commercially available forms of monolithic SiC within the project, and taking into account that the majority of work important in this field focusses on various composites, especially with respect to legitimate future engineering materials for use within the nuclear arena, it was decided that looking into some composite fabrication would be an interesting sideline to the main work.

On the back of this, work was carried out at General Atomics (San Diego, USA) manufacturing SiC composite and SiC monolith using the hot pressing technique known as the Transient Eutectic-Phase (TEP) process. A variety of materials were designed to allow for examination of varying parameters within the fabrication process. These materials could then be used to compare with micro-mechanical properties of material obtained commercially for the majority of this project.

This particular processing technique was chosen to allow for quick material production given the limited time and funds available to spend on this fabrication, and due to the fact that it is one of the techniques that General Atomics is using in the production of test components for nuclear fission reactors. In addition to this, the focus of this project has been on commercially available, cheap and easy to produce material, and material produced using the TEP method falls within these parameters.

5.2 The TEP process

The basic premise of the TEP process is that a fully mixed SiC powder is combined with sintering agents and milled to a fine powder. This powder is then put in casts and placed

between compression plates in a furnace. The combination of pressure and heat then stimulates the sintering process within the material to produce a bulk material. For this reason the process is a slightly more advanced combination of hot pressing and direct sintering, giving a good comparison to other materials used in this project. The process is used across various industries and is being studied widely in the nuclear industry. The technique described here is similar to that described by Dong et al [224] and the same as used by Novitskaya et al [225].

5.2.1 Precursor powder processing

The first stage in any TEP production method, is the preparation of the precursor powder. In this study Aluminium Oxide (Al_2O_3, 99.99% pure, US Research Nanomaterials Inc. TX, USA) and Yttrium Oxide (Y_2O_3, α phase, 99.9% pure, US Research Nanomaterials Inc. TX, USA) were used as sintering agents. Powder in this proportion to a nominal 10%wt was added to a β-SiC powder (99 + % pure, US Research Nanomaterials Inc. TX, USA) at the desired total weight percentage. These powders were then added to the milling media and mixed with a lubricant to create a non-viscous mixture. This was shaken thoroughly and checked to ensure the powder was fully in suspension before being sealed and placed on rollers for at least 24hrs. This milling process ensures an evenly mixed powder, and an even nanoscale particle size.

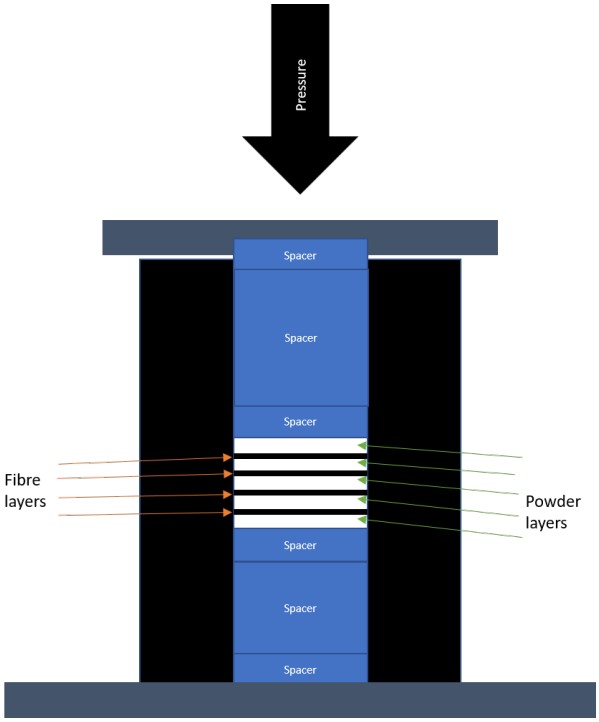


Figure 5.1: Diagram of laying up process in tooling (Not to Scale)

Once the SiC slurry had been milled to produce an even particle size the mixture was placed in an open flask in a slightly elevated temperature extractor space and left so all the lubricant could evaporate. The remaining mixture was then sieved to separate the SiC powder from the milling media. The powder produced can then be used to impregnate SiC fibre weave sheets, and be layered for production of bulk material.

5.2.2 Laying up process

SiC fibre weave sheets impregnated to create a full matrix around the fibres with the powder we had created were provided by General Atomics. Monolithic material was made just layering the produced powder, and the addition of these fibre sheets then created composite material.

Pre-made graphite tooling was used to produce all material for this project. The powder was carefully weighed and layered, ensuring each layer was even. For a monolithic material this was the whole layering process, however for composite material the powder and a cut out of fibre were layered until the desired size of material was made, ensuring each fabric layer was unidirectional. A diagram of this process can is shown in Figure 5.1. The whole process was performed in a fume cupboard to prevent inhaling dangerous particulates.

Any offset of fibre layers at this stage is known to reduce the integrity and strength of the whole material. Once a sample is laid up completely spacers are placed and the SiC layering is cold pressed to $600Pa$

5.2.3 Hot pressing and removal of material

The prepared sample was then ready for hot pressing. It was placed in the hot pressing furnace (OXY-GONE Industries Inc.) carefully aligning the centre of the tooling under the system hydraulics, and lowering the hydraulics until the system was secure. The system was pumped down and flushed with Argon before pumping down to a vacuum of $< 5 \times 10^{-5}$ Torr ($\sim 6.7 \times 10^{-3} Pa$). The system was then ready to be run to the desired program. At this stage many variables were available: controlling the hydraulic pressure; the temperature; ramp times and rates; and dwell times. Some of these parameters are variables used in this work as discussed in Section 5.3. It is whilst at temperature and pressure that the true TEP process takes place, with the sintering agents and SiC particles reacting together to create a solid dense material. For this work a peak load of $\sim$ 40kN or equivalent stress of $20MPa$ was reached.

Once the run was complete and the furnace cooled the tooling was extracted and left to fully cool before samples could be extracted. The samples were then removed carefully from the tooling. At this stage any raised edges were also ground down to make samples safe to handle. The sample material was then ready for characterisation and testing.

5.3 Fabricated Materials

Available parameters of the fabrications were restricted due to the nature of the work taking place at General Atomics. For this reason only the layering of powder (material matrix layers) and fibre weave sheets was performed, along with various programme parameters during hot pressing. It was agreed that $1mm$ thick blank disks would be made for all specimen samples, which would then allow for 4-point bend testing of each type and then be usable for further nanomechanical testing in Oxford.

The first variable to be adjusted for this work was the total %wt of sintering agents to be used. While Yttria and Alumina are compounds containing elements which are inert in most environments, they are not particulally suitable for fusion [25] with possible transmutations being more dangerous. For this reason, while 10%wt is the proportion normally used of sintering agents for other applications, if material with similar properties can be produced with a lower %wt it would be beneficial for fusion applications. With this in mind the principle variable for these samples was made to compare the effect of 5%wt and 10%wt sintering agents.

One of the major aims of this project has been direct comparison of SiC material with these fabricated materials allowing for a comparison of the behaviour of monolithic vs composite SiC. This desire led to two further production parameters being varied, the maximum temperature reached in the furnace, and the length of hold at this temperature (at maximum load). This was deemed necessary as the standard conditions used by General Atomics were different for the composite and monolith materials, with maximum load being for 75mins at 1800°C and 60mins at 1900°C respectively. Here the increased dwell time compensates for the lower temperature used in composite production to protect the fibres. The desire was to test how the matrix in both the monolith and the composite compared with these different production techniques. Samples are labelled by their fabrication variables: M/C (Monolith/Composite)- 5/10(%wt of sintering agent) - 1800/1900 (Temp at max load) - 60/75 (Time at max load).

5.4 Material Characterisation

Using the equipment available at General Atomics, and to give a brief but insightful look into the characterisation of the materials, two main characterisation methods were used to look at all

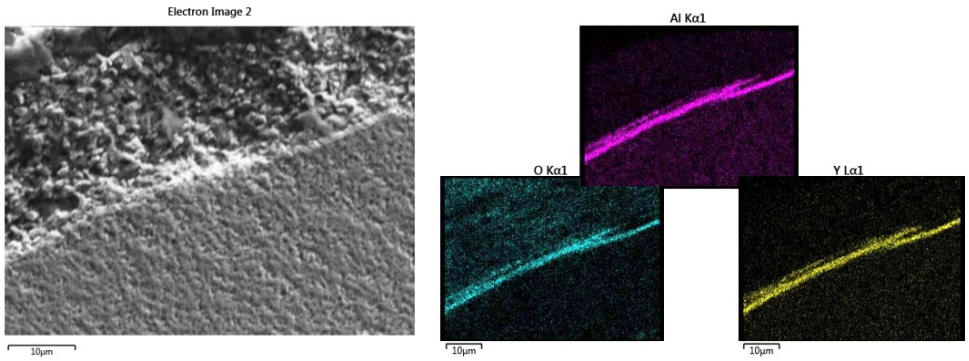


Figure 5.2: SEM and corresponding EDX analysis for sample M-5-1900-60 showing sintering agent remnants

samples produced. These were X-ray Computed Tomography (XCT) and four-point bending. In addition to this Scanning Electron Microscope (SEM) images and Energy Dispersive X-Ray Spectroscopy (EDX) of materials were taken back at the University of Oxford to compliment further nanoindentation and ion irradiation work carried out.

5.4.1 Post process parameters

To start characterisation of the sample plates size, density, and XCT measurements were made. These showed what mass changes were evident due to the TEP process, and also allowed for a comparison of results obtained from the XCT versus traditional methods of density given a certain size and mass. The XCT was able to give a much better insight into these properties and was also able to show some distribution of areas dominated by segregated sintering agents. The first result noted that there was no correlation between material density and any processing variables, including monolithic vs composite material. Consistently across all sample types less dense areas were seen in XCT and correspondingly in SEM images, both showing as white patches or lines. EDX was performed on multiple samples and these areas were all seen to be dense with Aluminium, Yttrium and Oxygen, showing that they are all areas rich with sintering agent remnants. The degree to which these elements were seen varied between samples, but not with a consistency that warranted any quantification of these residual elements.

Further observations from the XCT and SEM are more easily compared separately for the monolithic and composite material.

Monolithic Materials

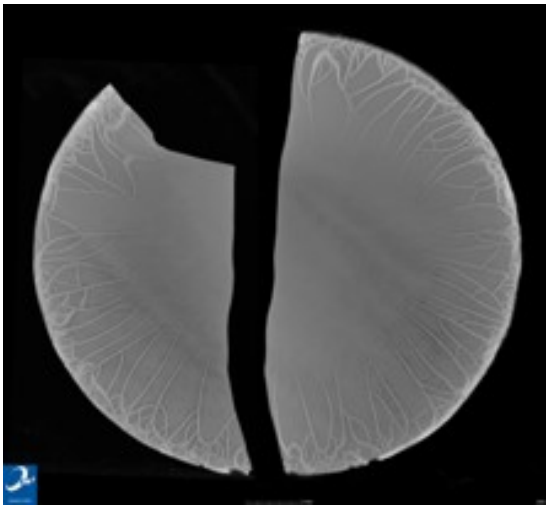
The first thing of note with the monolithic samples was their fragility, there were quite a few which broke in extraction from the tooling and many others broke during cutting and polishing processes for SEM and four-point bend sample preparation. The worst of these was the M-10-1900-60 sample. Looking at the XCT of the large fractured pieces the reason for this is obvious. Figure 5.3a shows large tendrils of remnant sintering agent radiating in from the edge of the disk. These areas were more brittle than the surrounding material, and allowed for crack propagation across the disk. This 10% sample is easily compared to the M-5-1900-60 sample, with its XCT image shown in Figure 5.3c Here very few sintering agent remnants are visible, with just a few in evidence at the very edge of the sample. Despite this the 5% sample also broke in the cutting process. Both these samples appeared to have layered well in production, with even thickness distribution as seen in Figures 5.3 (b),(d) and (f). It was however also clear that the sintering agents were segregating to thin layers on the top and bottom of the disks, as shown by the EDX in Figure 5.2.

Comparing these unsuitable monolithic materials to the M-10-1900-75 sample, we are seeing less sintering agent segregation to the edges, with remnants evenly distributed throughout as seen in Figure 5.3e. This sample is also showing a relatively even thickness across the disk showing a well prepared and layered sample. No further significant differences were seen in the monolithic samples: the 10% sintering agent samples generally showed a larger proportion remnant post production consistently across all other production parameters. Further material characteristics did not correlate to processing parameters.

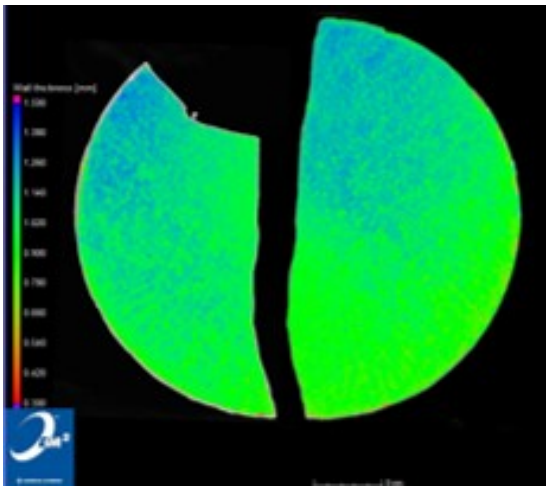
Composite Materials

Composite materials in the XCT all appeared very similar. You could distinctly see where the fibre layers were through the material, allowing for observations where fibre layers were not unidirectional. Example thickness plots and SEM images are shown in Figure 5.4. Consistent across all samples produced at 1800°C was the varying thickness of the material, with some varying by as much as $0.5mm$ across the disk where the maximum thickness was around $1.25mm$. This is clearly a problem, some of which will originate from the laying up process.

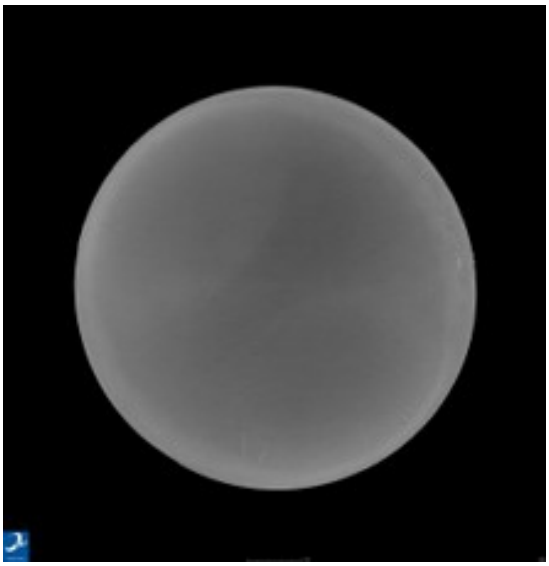
Moving on to look at SEM images a clear problem was found with all samples produced



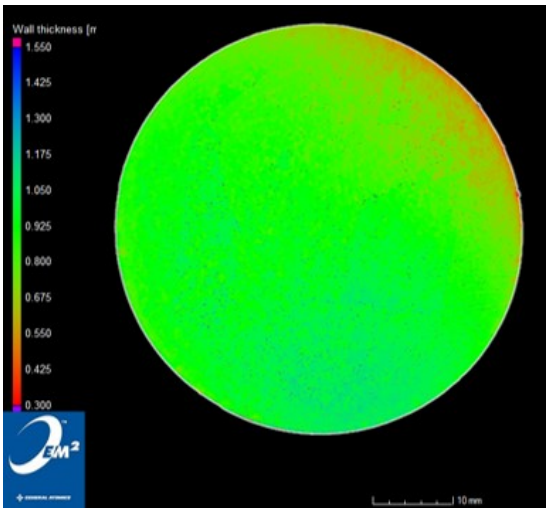
(a) M-10-1900-60 XCT image



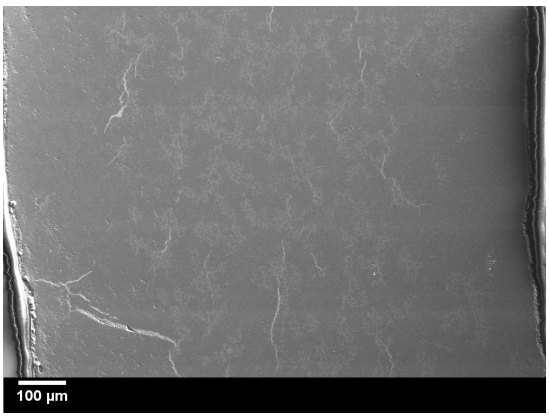
(b) M-10-1900-60 thickness



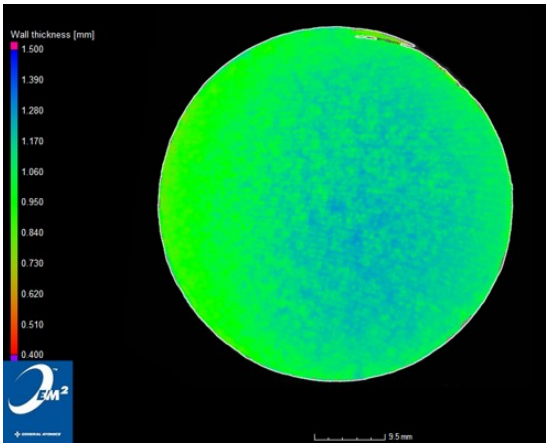
(c) M-5-1900-60 XCT image



(d) M-5-1900-60 thickness

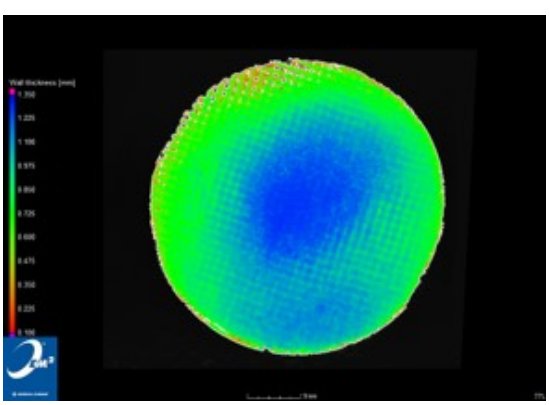


(e) M-10-1900-75 SEM image

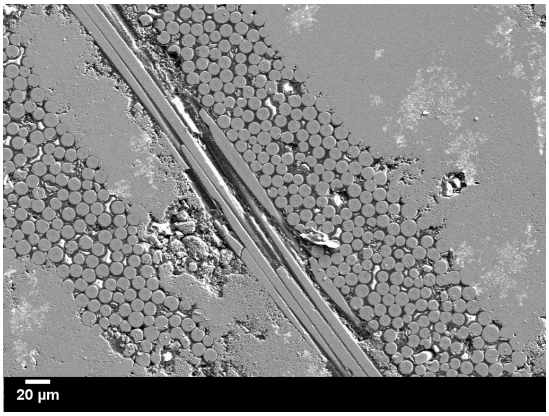


(f) M-10-1900-75 thickness

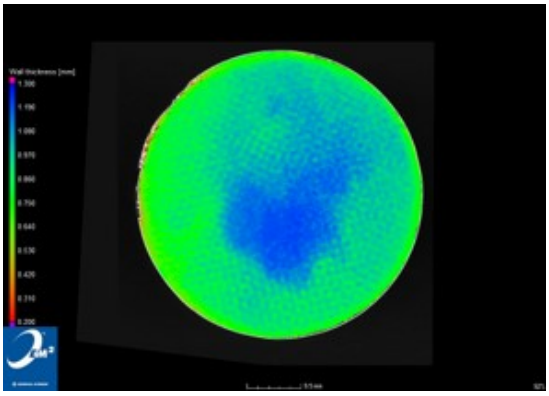
Figure 5.3: Thickness measurements from XCT along with XCT and SEM images showing remnants of sintering agents. Each disk was 50mm diameter, thickness is depicted so blue is the thickest part of the disks.



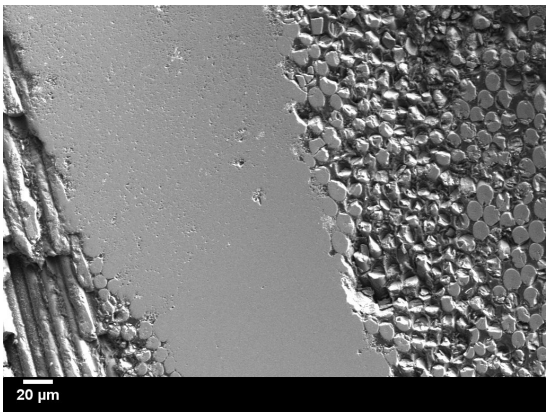
(a) C-10-1800-75 thickness



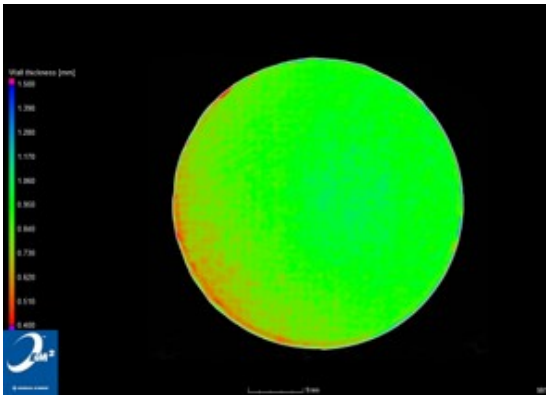
(b) C-10-1800-75 SEM image



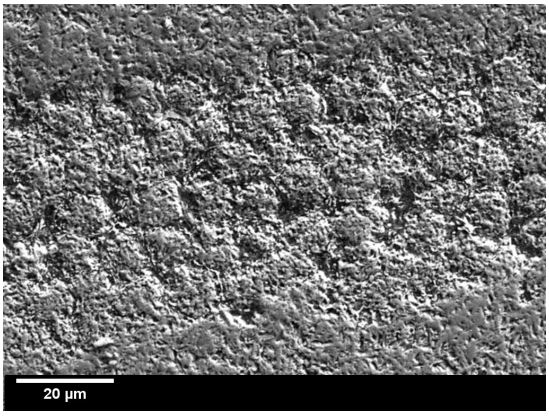
(c) C-5-1800-75 thickness



(d) C-5-1800-75 SEM image



(e) C-10-1900-75 thickness



(f) C-10-1900-75 SEM image

Figure 5.4: Thickness measurements from XCT along with SEM images showing various composite material characteristics. Each disk was 50mm diameter, thickness is depicted so blue is the thickest part of the disks.

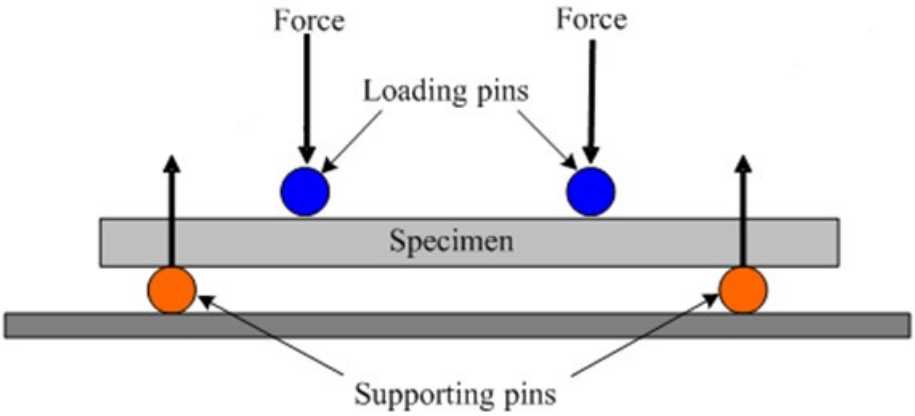


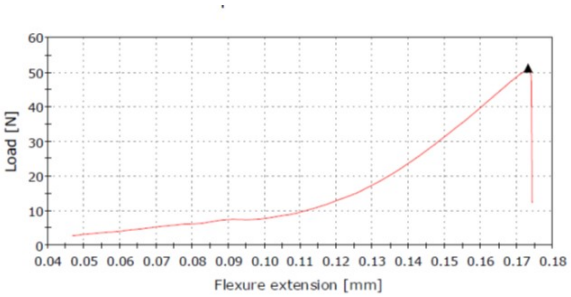
Figure 5.5: Diagram showing set up for four-point bend experiments [227]

at 1900°C, where all definition of the fibres had disappeared, the Pyrolitic Carbon (PyC) and fibre matrix sintering together leaving only shadows of the fibres to be visible in the SEM. These samples also showed less variation in thickness across material disks. As also seen in the monolithic disks, remnants of the sintering agents were seen in the matrix layers of the 1800°C materials, again with more seen in the 10% samples than the 5% samples. The sintering agent remnants were either seen as particles within the grain structure, layers at the surface, or as segregated 'lines' stretching from the fibre layer into the matrix layer, often through the thickness of the matrix layer. These effects were not seen in the 1900°C material showing that the sintering effect of the fibres into the matrix was dominant in the TEP process.

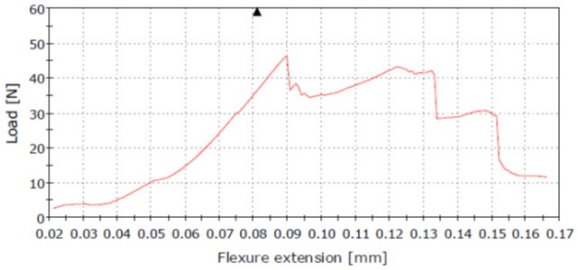
5.4.2 Four-Point Bend Testing

Four-point bend testing was performed to the ASTM standard C1341 [226] for each sample plate produced, as long as it was still intact post cutting (as some samples fractured at various points post the TEP process). Each sample plate was cut into 10 equally sized pieces using a low speed diamond saw (nominally $25 \times 3 \times 1mm$), and a record of where in the plate each 4-point bend sample was taken from was made. The bottom side of each sample was then polished until shiny where possible, down to a polish using $1\mu m$ diamond water suspension. In many of the composite samples the weave layer was too close to the bottom of the sample plates for a perfect polish on the bottom of the samples, as the samples would then have broken though the PyC layer around the fibres and into the fibres themselves pre-testing, weakening the material. The four point bend set-up is shown in Figure 5.5.

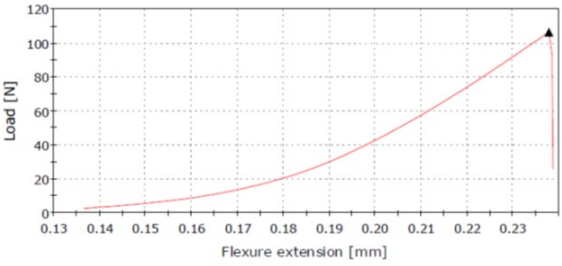
As expected the samples fell into two distinctly different categories for fracture and flexural strength. The first category is the behaviour expected from a monolithic material, where there is a constant increase in flexural extension showing linear elastic behaviour until complete failure occurs. The second category is characteristic of composite materials, where multiple load drops occur, and although there is fracture, complete failure does not necessarily occur. The main thing to note here is, that while all the monolithic SiC behaved as expected, composite samples which had been heated to 1900°C during the TEP hot pressing process did not exhibit normal composite behaviour, with no load drops occurring, and all samples exhibiting complete failure. Example load profiles for a monolithic sample, and composite samples showing composite and monolith behaviour are shown in Figure 5.6. Furthermore some of the composite samples showed a stronger composite profile, of multiple load drops and a higher flexural strength, with the integrity of the test sample remaining post test. In these samples although the monolithic matrix layers of the material had through thickness cracks, the fibre sections did not. Here the fibres were acting as designed, preventing crack growth, and cracks through the matrix layers were not necessarily aligned. Other composite material however did exhibit complete failure, showing fracture through the fibre weave and parallel matrix cracking. Disappointingly these behaviour changes did not correlate with processing variables, leading to a belief that the differences seen were due to the fibre sheet production, where the matrix



(a) 1900°C composite material



(b) 1800°C composite material



(c) monolithic material

Figure 5.6: Plots showing flexural extension with load for four-point bend tests, showing representative characteristics for 1900°C composite material (5.6a sample C-10-1900-75), for 1800°C composite material (5.6b sample C-5-1800-75) and for monolithic material (5.6c sample M-10-1900-75).

around the fibres was not fully densified, however this was not a controlled variable as fibre sheets were pre-provided by General Atomics.

Composite materials are expected to act in the manner as seen in 5.6b, where load drops correspond to failure and de-bonding of individual layers [228]. This sort of behaviour is simply shown using Cox's Shear-lag model, which states that if there is no slip on phase interfaces the fibres redistribute the stresses and strains transferring load for the matrix to the fibre [229]. We thee this by the load first being supported, then falling. The rise again is caused by the deflection of the crack at the interface, impinging the development of a crack though the whole thickness of the material. When de-lamination occurs we again get crack growth [228]. This release or dissipation of the energy in building with the increased external load is proportional to the surface of the newly formed crack [230]. These types of de-lamination cracks are load dependent are do not form in the same way with fatigue cracking [231].

Consistently across all samples, a wide distribution of strength through the 4-point bend samples representing the width of the sample plates was seen. Across all samples there was an average distance of 26% of the load values from the mean load of a samples maximum load, and a mean distance of 36% of extension from the mean extension at maximum load giving a 20% distribution of strength values. This clearly shows inconsistencies with the way the materials were manufactured, and can be expected given the density variations seen, particularly at the edges of the sample plates as seen in the XCT. Weibull statistical analysis could have been used here, however the physical differences across the bend samples for each plate meant that it was not suitable, as there were too many inherent physical properties changing influencing the 'random' nature of composite fracture.

When looking at the whole of the dataset, correlations between the varied parameters and flexural strength were observed. For composite samples there was a small correlation between flexural strength and density of the samples, however this effect is mostly seen because the composites processed with the higher temperature of 1900°C became more dense as the PyC coating the fibres and the fibre matrix were 'absorbed' into the matrix of the material removing the composite structure. Although these samples exhibited greater flexural strength than those with composite behaviour, they completely failed during the four-point bend tests and were not as flexurally strong as their monolithic counterparts, showing they lost the positive

aspects of both monolithic and composite behaviour. Looking at the monolithic behaviours the samples manufactured at the higher temperature of 1900°C were seen to have less scatter in their strength, and exhibit larger flexural strengths, however this was mostly seen in the 5%wt sintering agent samples, as most of the 10%wt sintering agent samples were very brittle and broke either on extraction from the die, or broke during the preparation process for four-point bend testing.

Characterisation Conclusion

Some generalisations about the varying processing parameters, and other materials characteristics are now clear. The first of these is outside the control of this experiment, however has greatly affected the performance of many of the composite samples here: the densification and matrix of the SiC fibre weave sheets. The appearance of the fibre layers as seen in the SEM alone was enough to question how they would perform, and the four-point bend test inconsistencies confirm this. For this reason other than the effect of the higher dwell temperature for the change in flexural performance, the effect of the other fabrication parameters are not obtainable. Looking at the four-point bend results with the basic material parameters, no correlation was seen between flexural strength and any processing parameters, nor thickness or porosity of material.

5.5 Silicon Ion Irradiation

Given the material characterisation performed at General Atomics, the accompanying SEM work, and the restrictions on ion irradiations; it was decided that the most promising of the fabricated material be studied further with nanoindentation and ion irradiation studies. It was decided to focus the ion irradiation study on the best of the composite samples seen: those exhibiting high flexural strength. It was also decided to try and focus this irradiation study on the effects of the different percentages of sintering agents used as these are some of the most critical processing parameters for fusion applications. For this reason composite samples manufactured with variables of 1800°C and 75mins peak load dwell were used. A monolith sample was also included to give a further comparison, the monolith sample used was manufactured with variables of 1900°C and 75mins peak load dwell and 10% sintering agent.

Unfortunately there was not enough space for a 5% monolithic sample for a better sintering agent effect comparison, so these parameters were chosen as the closest to General Atomics normal processing parameters (all 60 minute samples were broken at various stages and not deemed suitable for this study). These samples are referred to by their fabrication parameters: C-5-1800-75; C-10-1900-75; and M-10-1900-75 and were some of the examples used in Figures 5.3 and 5.4.

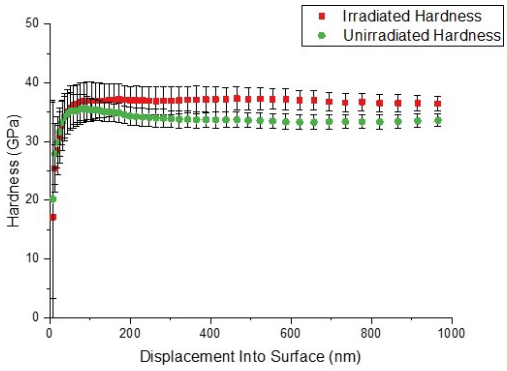
Si ion implantations were performed on these samples as described in Section 3.6. Following these ion irradiations nanoindentation was performed in combination with visual and SEM analysis to characterise the effect of radiation damage on these materials.

5.5.1 Nanoindentation

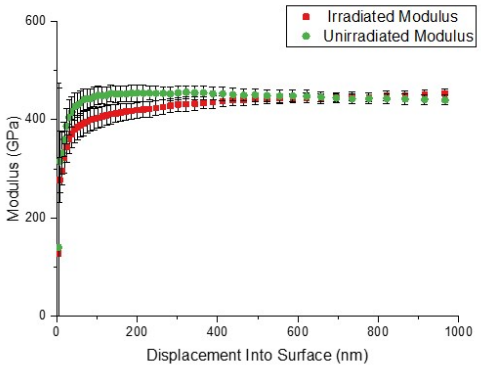
As far as possible nanoindentations were performed in clean material, as homogeneous as possible with few sintering agent remnants within the nanoindentation area. Despite this, on some samples this was not possible, so even before looking at any results from these nanoindentations the inhomogeneity of the samples is known, and is expected to cause some problems. In addition to this one of the samples irradiated at 2.4dpa to 300°C (the 5% composite sample) was too thin to then indentation properly so no data is available for this sample.

Indentations were performed on the covered part of the samples to give unirradiated measurements as well as irradiated measurements for each condition. This ensured that any additional changes made by the temperature of the irradiation conditions could be accounted for. At least 64 indentations were performed for each data set, and following this, indentations which showed significant problems with either load/displacement plots, or elastic modulus plots were discarded, as these represented indentations performed in surface holes, across fibres or through large sections of sintering agent, and were not representative. Data for all remaining indentation runs were then collated.

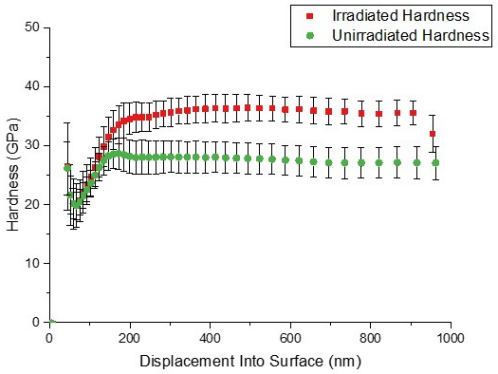
With hardness a property which depended on the just the area of plastic deformation around indentations a constant increase in hardness was seen through the depths of all samples to varying degrees. Average hardness values were taken at $300-800nm$ depth to then allow effects of radiation damage to been seen through percentage changes. While bulk elastic modulus values were also taken at depths of $300-800nm$ percentage changes in the properties were taken from



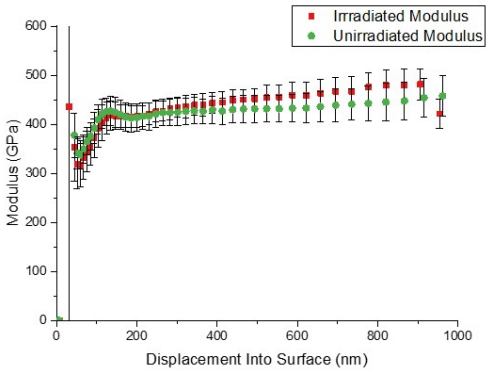
(a) Hardness C-10-1800-75 2.4dpa 750°C



(b) Elastic Modulus C-10-1800-75 2.4dpa 750°C



(c) Hardness C-10-1800-75 2.4dpa 300°C



(d) Elastic Modulus C-10-1800-75 2.4dpa 300°C

Figure 5.7: Example plots showing hardness and modulus data where (a)&(b), show good examples of plots and (c)&(d) give an example of good hardness data alongside a bad example of modulus data. Standard deviations are given as errors.

depths of $50-200nm$. These values are consistent with those used in Section 4.4. The hardness and elastic modulus results as percentage change from the unirradiated bulk are summarised in Figure 6.3 with absolute values given in Table 5.1. Errors given are one standard deviation, which are then propagated to give errors on the percentage change values, those discussed as giving the larger errors in Section 4.4.

It is noted that where some sets of indentation data showed load/displacement plots as expected from the earlier work, others exhibited other non-linear behaviour with depth. Those which exhibited this different behaviour did however show the expected and normal behaviour in hardness. Examples of normal data plots in comparison to these are shown in Figure 5.7. The non-linearity of these plots is likely due to the inhomogeneity of the samples, but could also be enhanced by the area function of the indenter becoming less accurate as the tip indenter tip became blunter.

Sample	Irradiation Conditions		Hardness (GPa)			Elastic Modulus (GPa)		
	Temperature (°C)	Dose (dpa)	Unirradiated	Irradiated	% Change	Unirradiated	Irradiated	% Change
C-5-1800-75	300	0.24	33.8 ± 3.4	38.2 ± 0.5	13.0%	540 ± 45	455 ± 6	−12.9%
C-10-1800-75	300	0.24	28.9 ± 4.8	36.4 ± 1.8	24.5%	407 ± 46	415 ± 17	−0.1%
M-10-1900-75	300	0.24	29.7 ± 1.9	35.3 ± 2.7	16.4%	450 ± 17	443 ± 20	−5.7%
C-5-1800-75	750	0.24	34.4 ± 1.2	38.4 ± 0.4	11.6%	472 ± 8	454 ± 5	−5.4%
C-10-1800-75	750	0.24	36.8 ± 2.8	41.3 ± 2.1	12.0%	576 ± 38	573 ± 23	−6.3%
M-10-1900-75	750	0.24	31.3 ± 1.0	34.6 ± 1.7	10.5%	481 ± 11	474 ± 14	−2.2%
C-5-1800-75	300	2.4	29.0 ± 1.2	N/A	N/A	440 ± 13	N/A	N/A
C-10-1800-75	300	2.4	27.8 ± 2.5	36.1 ± 2.2	30.1%	432 ± 26	452 ± 23	−2.7%
M-10-1900-75	300	2.4	29.4 ± 1.8	30.4 ± 3.4	7.1%	450 ± 14	397 ± 22	−15.7%
C-5-1800-75	750	2.4	29.7 ± 1.9	35.8 ± 1.8	20.2%	422 ± 16	418 ± 9	−5.8%
C-10-1800-75	750	2.4	33.6 ± 1.2	37.1 ± 1.9	10.4%	450 ± 10	440 ± 9	−9.2%
M-10-1900-75	750	2.4	29.5 ± 2.2	33.9 ± 2.7	14.0%	472 ± 21	452 ± 23	−2.2%

Table 5.1: Elastic Modulus and Hardness results from nanoindentation on fabricated samples also showing percentage change in properties from the unirradiated bulk. Average values for Hardness and Elastic Modulus were taken for depths of $300 - 800nm$. Hardness percentage change taken from depths of $300 - 800nm$, elastic modulus percentage change taken from depths of $50 - 200nm$

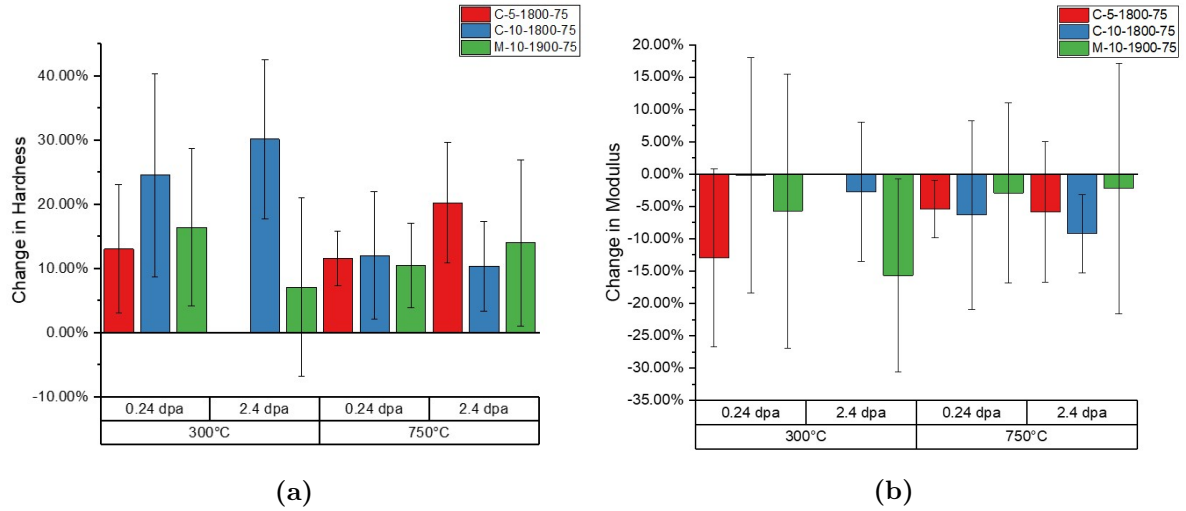


Figure 5.8: Plot showing the relative difference between unirradiated and irradiated materials for elastic modulus and hardness across all irradiation conditions.

Some conclusions can be made about the effect the varying implantation conditions have had on the hardness of the fabricated materials. A general trend that irradiations performed at 750°C exhibit a smaller increase in hardness is seen, and this is especially the case with the C-10-1800-75 sample, however the 300°C 2.4 displacements per atom (dpa) irradiation showed a $\sim$ 30% increase in hardness. The C-5-1800-75 sample is more difficult to draw conclusions on, but where it shows less of an increase in hardness than the C-10-1800-75 sample at 300°C, they show more similar increases in hardness at 0.24dpa 750°C, and the C-5-1800-75 sample is showing a marked larger increase hardness at the higher dose at 750°C. It is clear that in hardness there is a marked difference between the two %wt of sintering agents. Looking at the composite materials elastic modulus, it is harder to make good conclusions, especially with the data dominating errors. Despite this it is clear that at the higher temperature the reduction in modulus is smaller than the reduction seen at lower temperature irradiations, although quantifying this is not possible.

Looking separately at the behaviour of the monolithic sample M-10-1900-75, it is showing a combination of changes. It does not follow the same trends as the 10%wt composite sample, and instead shows a decrease in hardness with higher dose as well as with higher temperatures. The elastic modulus behaves slightly differently with the largest reduction in elastic modulus seen at 2.4dpa and 300°C, and the smallest seen at 2.4dpa 750°C.

The errors shown in Figure 6.3 give the larger estimate of error (known to be an overesti-

mation), as they are propagated from the standard deviations on complete data sets for each sample as discussed in Section 4.4.1. While neither method of error calculation discussed was accurate, it was decided that the overestimation was more suitable for the data here. It is however enhanced by the larger variance in this data set, especially in the elastic modulus data, due to inhomogeneity in the samples themselves. As previously discussed in Section 4.5 an ANOVA type statistical analysis to compare the significance of the data sets would be incredibly helpful here, as distinguishing significance from this data is very difficult. Again, the same nanoindentation software was in use so such statistical analysis was not possible.

Sample	Hardness (GPa)	Elastic Modulus (GPa)
C-05-1800-75	32.6 ± 2.5	478 ± 59
C-10-1800-75	31.8 ± 4.2	466 ± 75
M-10-1900-75	29.7 ± 1.2	463 ± 16

Table 5.2: Average unirradiated values for fabricated materials hardness and elastic modulus with standard deviation errors based to differences between each irradiation run condition.

Unirradiated material properties are summarised in Table 5.2. This shows that the intrinsic properties of C-5-1800-75 give the hardest and largest elastic modulus measurements. We also see that large variations in nanomechanical properties are seen here. Some variations were expected due to the inhomogeneity of the samples themselves. Increased values for hardness and elastic modulus in both the 10% samples, the C-10-1800-75 and the M-10-1900-75, were seen after being in the 750°C ion implantation conditions. While it was not possible to see grain structure contrast in the samples to assess whether this effect is down to grain size, the precursor powder for all sample types was the same, so no difference was expected.

5.5.2 Fracture

Post nanoindentation SEM work was undertaken to observe the fracture in these samples in the same way as was performed in Section 4.2.3. Effects of all ion irradiations were obvious with radial cracks evident on unirradiated samples not present on any irradiated sample as shown in Figure 5.11. Generally no corre-

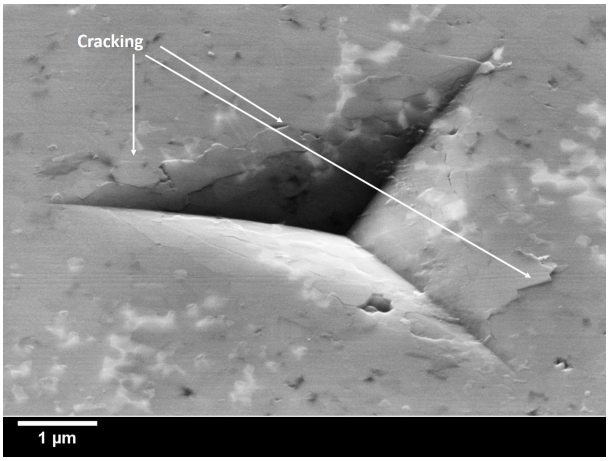


Figure 5.9: SEM image taken with a 54° tilt of indentation into irradiated M-10-1900-75 showing detailed fracture around grains

lation between irradiation condition and fracture around nanoindentation was found, in addition the fracture behaviour in both composite samples are very similar. Cracks within the indentation surface are running along grain boundaries, with slip occurring in some locations, seeing grains along the fracture surface pushed up. This is effect is most prevalent in the monolithic sample as seen in the tilted SEM image in Figure 5.9. The grain structure is clearly defined around this indentation into irradiated material, and twinning is seen within the grain structure. The cracks are running cleanly along the grain boundaries. This is contrasted by the lack of defined grain structure seen post irradiation in the composite samples. With no literature found that looks into the fracture, and suppression of fracture with irradaition on real composite materials this is an important result, especially where these differences are seen between the monolithic and composite materials fabricated in the same way.

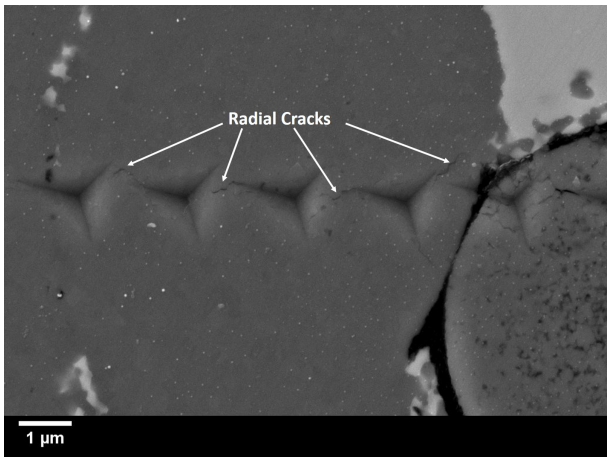
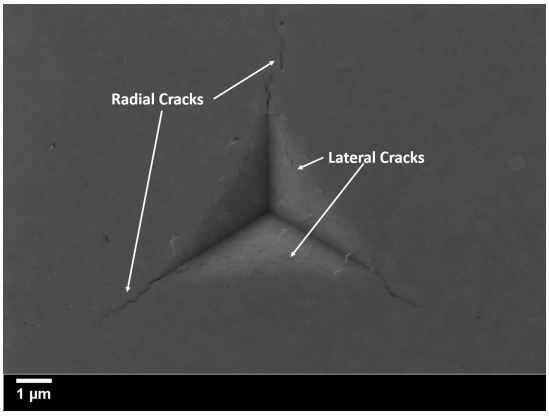
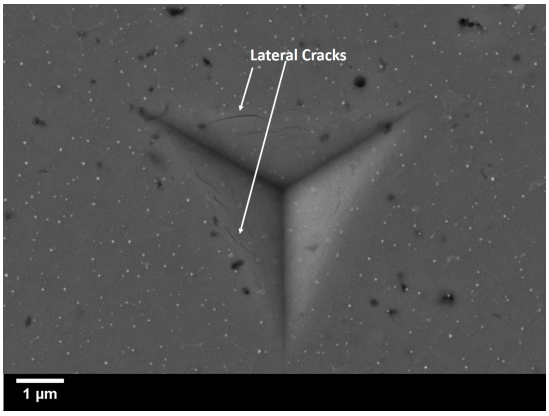


Figure 5.10: SEM image of a line of $300nm$ deep indentations into fibres in C-10-1800-75 showing fracture extending between indentations

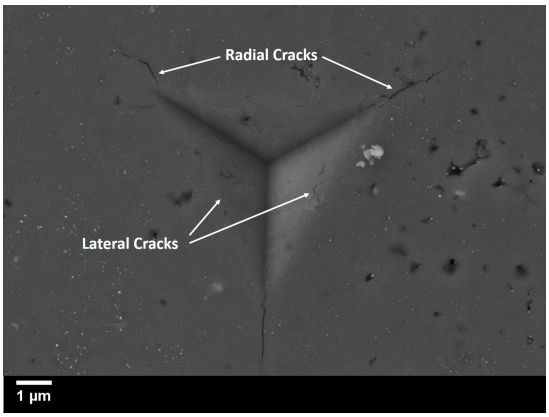
Preliminary tests were performed using smaller indentations ($300nm$ deep) across the composite fibre layers to give a profile of nanomechanical characteristics across the boundary from matrix into fibre and the effect ion irradiation on these characteristics. These tests showed that the extensive fracture seen in larger indentations was also present here, with cracks stretching far enough to influence the measurements in the next indentation test performed in these unirradated tests as shown in Figure 5.10. It is know from the work in Chapter 4 that although extensive surface cracking is not seen on the surface in irradiated samples, fracture networks beneath the surface are still present. For this reason an investigation of this type is not possible without compromising data quality or resolution of the characteristic profile. Whilst this would be an interesting investigation, the variable parameters in this study were not relevant to the fibre layers so was not pursued.



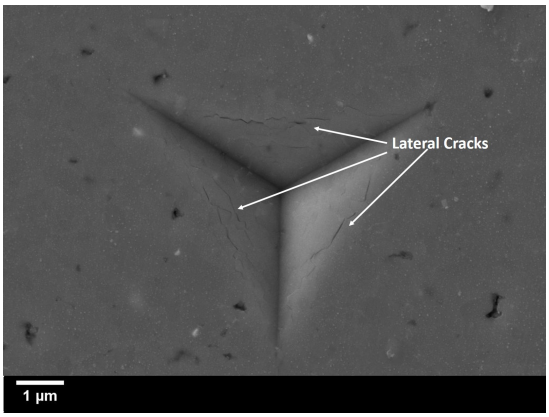
(a) Unirradiated C-5-1800-75
0.24dpa 300°C



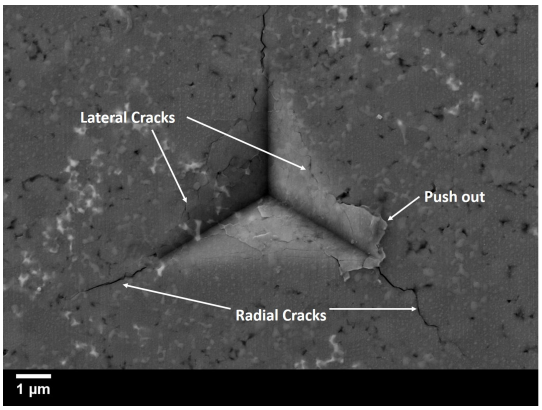
(b) Irradiated C-5-1800-75
2.4dpa 750°C



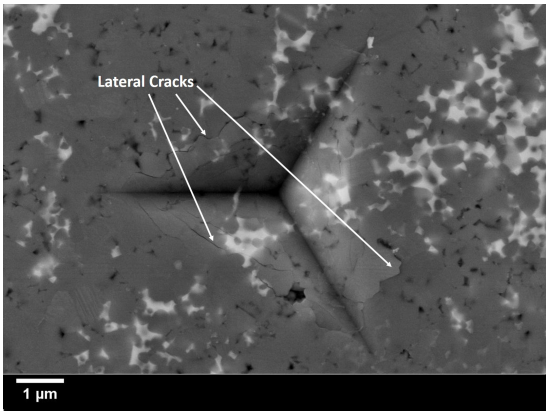
(c) Unirradiated C-10-1800-75
0.24dpa 300°C



(d) Irradiated C-10-1800-75
0.24dpa 300°C



(e) Unirradiated M-10-1900-75
2.4dpa 750°C



(f) Irradiated M-10-1900-75
2.4dpa 750°C

Figure 5.11: Example SEM images of each material showing indentations on unirradiated and irradiated material. No observable difference is seen between irradiation conditions so random images have been chosen but conditions are shown with each image.

5.6 Discussion

Despite initial work and fabrication on these materials showing various problems some valuable results have been obtained, especially with regards to the effects of ion irradiation damage. It is noted that this work can act as a good preliminary study especially with effect of the 5%wt sintering agents on material characteristics. For this work to have been able to draw better conclusions with regard to the macroscopic studies, more sample disks would need to have been produced with each variable set to allow for statistically significant data to be retrieved. A summary of the key results is seen in Table 5.3.

The macroscopic work was enough for some broad conclusions to be drawn. For this study disks of $\sim 1mm$ were produced and this meant that surface effects from the remnant sintering agents were amplified, causing significant problems with the monolithic samples, particularly those produced with an initial 10%wt sintering agent. Generally it would be expected that the 10%wt proportion of sintering agent would produce a denser material increasing its material strength. In this study however, this advantage was dominated by the other effects and often lost completely. This was shown particularly when looking at the composite samples under irradiation. The C-5-1800-75 sample had a density of 85.9%, less than the C-10-1800-75 sample's density of 88.7%, under the 750°C 2.4dpa irradiation condition when a reduction in elastic modulus is seen, this increased porosity has an advantage and means that the degree of reduction in modulus in sample C-05-1800-75 having a much smaller reduction in modulus of 1.11% in comparison to sample C-10-1800-75's reduction of 2.18%. This result fits well with the literature on effects of sintering agents in TEP materials [127,232,233]. This in turn relates to the swelling under irradiation: the porosity is giving allowances for the lattice swelling restricting bulk

Sample	Density	Flexural Extension (μm)	Flexural Strength (MPa)	Unirradiated Hardness (GPa)	Unirradiated Modulus (GPa)	2.4dpa 750°C Hardness	2.4dpa 750°C Modulus
C-05-1800-75	85.91%	76 ± 20	171 ± 20.9	32.6 ± 2.5	478 ± 59	20.28%	-1.11%
C-10-1800-75	88.69%	162 ± 71	162 ± 31.9	31.8 ± 4.2	466 ± 75	10.37%	-2.18%
M-10-1900-75	97.07%	159 ± 44	289 ± 43.0	29.7 ± 1.2	463 ± 16	14.92%	-4.13%

Table 5.3: Summary of results for principle materials, showing results for the 2.4dpa 750°C ion irradiation as the most fusion relevant

swelling. This aspect is especially important when considering SiC as a fusion material. The vast majority of proposed designs use SiC as a structural material, so mitigation of material swelling will be an important factor. With the use of composite materials there is an additional factor to consider, that of relative swelling between fibres and matrix, which has been extensively investigated in the literature with Koyanagi et al [234] looking at its effect on the matrix with a similar radiation study to this work, but at the higher irradiation temperatures of at least 1000K, where the differential swelling is seen to be causing a decrease in axial residual stresses introduced into the material during the Nano-powder Infiltration and Transient Eutectic-phase (NITE) process. This in combination with Koyanagi et al's other work on neutron irradiated SiC [103] shows no significant effects on the mechanical properties at temperatures studied here, but does see degradation in properties tested, in these studies mostly tensile tests, atthe higher temperature of 1270°C. This shift in behaviour between that shown in Konyanagi et al's work and that presented here is likely due to the enhanced annealing occurring at the higher temperatures, in combination with the effect of reaching SiC's early transition points to other polytypes [39]. Konyanagi's work in comparison to this study shows more localised measurements possible with nanoindentation can give further insight into the behaviour of these materials under radiation conditions. This study has however found that while the effects of hardness can be easily observed, the inhomogeneity of material within each sample causes significant problems with observing elastic modulus, especially after irradiation energies which damage such shallow depths.

The biggest problems encountered with both the four-point bend tests and the nanoindentation work was an inherent inhomogeneity in the samples. This has caused increased uncertainty in measurements, some of which are accounted for in the large standard deviations on data sets, but some of these uncertainties were not quantifiable, and must be taken into account in making initial conclusions about this work. Taking into consideration all of the characteristics looked at in this work, much of this inhomogeneity originates from the fabrication itself and the effects of the thinness of the samples as already discussed. The fabrication of these samples was a learning process itself and it was found that samples produced later on were more even and consistent.

It can be concluded that the processing parameters traditionally used in the TEP process

for the production of composite materials is optimal for both proportions of sintering agents studied here, with fibres seen to fully degrade in samples prepared at 1900°C. The production parameters for the monolithic material, however, do not seem so optimised as many of the monolithic materials produced were too brittle to be studied. It is postulated that this was enhanced due to the size of sample material disks made, however with through-thickness tendrils of remnant sintering agent visible in 10%wt samples, some crossing over a third of the width of the disks it is believed that additional mechanisms are at play here.

An interesting effect seen here is that despite the density of the whole disk for the composites being lower than that of the monolithic material, with C-05-1800-75 having a density of $2.75g/cm^3$, C-10-1800-75 having a density of $2.2.84g/cm^3$ and M-10-1900-75 having a density of $3.11g/cm^3$, the matrix layer of the composites are denser as is clear from the fracture study with the nanoindentation. The majority of the composite porosity in these samples is in the fibre bundles. It is noted that it was clear that the matrix bundles were not surrounded by a fully densified matrix as expected, which caused a number of unquantifiable variations with the four-point bend tests. With this aspect of material fabrication outside the control and remit of this project conclusions on these cannot be made. The dense matrix layers in the composite material have given rise to a higher nano hardness and elastic modulus being found for these materials despite lower flexural strengths. C-05-1800-75 has a hardness of 32.6 ± 2.5GPa in comparison to M-10-1900-75 having a hardness of 29.7 ± 1.2GPa. This shows that the monolithic material may be less of an analogue for the composite matrix layers than hoped, and its material characteristic and radiation effects are modified in the composite material. This is likely to be due to the mismatch between material types acting as a sink for defects introduced by radiation damage.

5.7 Summary

In the process of fabricating these materials it was firmly established that temperatures of 1900°C could not be used to create composite materials, as the temperature degraded the interphase entirely and the SiC fibres began to diffuse into the matrix itself. It was established through the fabrication process that producing materials using the TEP method can be incredibly difficult as the parameters for production are a complex balance between the different

material properties required.

This study has shown that it is not possible to fully create monolithic analogues to composite matrix layers due to the different processing parameters required to create usable materials, as well as the enhanced density of the matrix layers in the composite materials in comparison to their whole. It has been found that although the higher 10%wt of sintering agent forms a less porous material, it can also leave large excesses of sintering agent within the material, which is likely to cause problems with transmutations in a fusion device.

Under various irradiation conditions it was found difficult to draw comprehensive conclusions due to varying and contrasting effects after the different Si ion irradiation runs, however the 5%wt composite sample was more consistent with effects on elastic modulus, as its lower density appears to have mitigated lattice swelling which causes the reduction in modulus in SiC.

This work has been a good representative preliminary study into these materials, however further investigation in needed into the effects seen to make comprehensive conclusions about the effects of the sintering agents on their nanomechanical properties under radiation damage. A key result from this work is that inhomogeneity in such materials has caused much larger problems than foreseen, however these problems are likely to be solved with mass production and after such a time these materials could become very promising.

Chapter 6

Hot Nanoindentation Studies

6.1 Introduction

As discussed in Chapter 4 a significant difference is seen in all materials investigated between irradiated and unirradiated SiC, at various temperatures and doses of self-ion implantation. However useful these results are at showing the mechanisms and mechanical changes undergone, and therefore end of life properties, or cool down properties in a Fusion reactor, they cannot give a good indication of behaviour during operation. We know from the room temperature studies there is an increased dislocation density induced by Si ion irradiation at all levels and temperatures, and conclusive summaries that show in all irradiation studies presented in this work this causes an increase in hardness and decrease in elastic modulus.

For better understanding of mechanical properties during operation, tests done at temperature are required to allow for effective use of materials within designs for future fusion devices. Here a study has been performed on a Direct Sintered SiC (DS-SiC) sample implanted with Si ions at 300°C to 2.4 displacements per atom (dpa) as described in Section 3.6. Experiments were performed across temperature ranges to $\sim$ 700°C, a fusion relevant temperature for blanket materials.

6.2 Methods

For the most part, as discussed in Section 3.3, the MicroMaterials hot nanoindentation system runs in the same way as the room temperature NanoXP and G200 systems, and methods for collecting results follow the same lines. There are however a few methodical issues brought about in this system, which had to be addressed before collecting results.

6.2.1 Calibration Methods

As discussed in Section 3.3 the MicroMaterials hot nanoindenter does not run with a Continuous Stiffness Measurement (CSM), so measurements are only facilitated for each load / unload cycle.

This changes the way the machine is run and data is collected, but one of the biggest challenges this causes is calibrating the indenter tip. In preliminary experiments it was seen that an uncalibrated or badly calibrated indenter tip caused results that did not make physical sense, with no match to any literature data. Three methods were used with different preliminary experiments before a full and complete calibration procedure was accepted.

In all cases the calibration indentations were performed, then a method of fitting to a Berkovich indentation curve and known material values was followed to produce an area function for the Diamond Berkovich tip used.

Calibration Method 1

The first method involved an array of test indentations performed on a fused silica test stub. Indentations were made to various depths focussing up to the depth of $1\mu m$.

A Diamond Area Function (DAF) was then produced using the MicroMaterials software using the known values of hardness and modulus for Fused Silica. This method produced a good match for the initial data: the hardness results produced in a test set on unirradiated SiC saw a good trend with temperature, however the modulus results were not acceptable. These factors were enhanced by the early test tip being very blunt. This is demonstrated in Figure 6.1

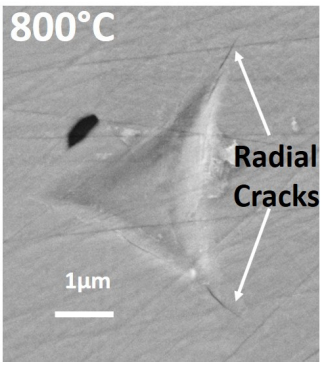


Figure 6.1: An Scanning Electron Microscope (SEM) image of DS-SiC indented at 800°C showing blunt nature of indenter in preliminary experiment

Although this method was repeated on a secondary run with a sharp indenter tip, results did not improve, and a later MicroMaterials software update rendered this method void.

Calibration Method 2

The second method involved arrays of test indentations on both the fused silica and tungsten test stubs. Indentations at various depths to $1.5\mu m$ were produced. The data from this was then sent to MicroMaterials, who fitted it to produce a DAF. Data using this calibration was not deemed acceptable, as hardness and modulus results were unphysically high at all points. This calibration method was therefore discarded.

Calibration Method 3

The third method began with the same indentation arrays on both fused silica and tungsten. These sets of data were then analysed using a two co-efficient fit of a Berkovich general form indenter using the MicroMaterials Analysis software. A method of trial and improvement was then used to get accurate values for both coefficients, using the fused silica data as a mark to optimise its hardness data, and the tungsten to optimise its reduced modulus data. A balance had to be made to ensure both hardness and modulus values fit those expected of fused silica and tungsten.The DAF was calculated using a polynomial function of order 2 calculated using the coefficients of $A = 0, B = 3900$, $C = 24.8$ with an indenter shape geometry factor of 1.

Frame Stiffness Calibration

Once the DAF was performed on collected data, a good frame stiffness correction was required. This value would vary with each experiment according to the manner of cement attachment of the sample to the surface of the hot stage. For this the pre-heating room temperature data was used, again a trail and improvement method was used to match the hardness and modulus values of the DS-SiC sample calculated on this MicroMaterials machine to data previously collected on the NanoXP shown in Chapter 4. This frame stiffness correction was calculated as 0.52 for the set of principle data, and was used across the temperature range. Following the collection of the principle data, it was noted that a re-calibrated data set from a preliminary experiment previously calibrated using Method 2 would bring its data into a sensible range. As the proper procedure was not followed for calibration of the indenter tip in the preliminary experiment, an accurate new tip calibration and therefore frame compliance measurement could not be taken. Despite this the results allowed for good size effect and fracture analysis. This data therefore was partially re-analysed using the fitting coefficients for the principle data set, which gave a good approximation of the diamond area function, as both sets used the same indenter tip. As this was not fully accurate, a proper calibration to obtain a frame stiffness was not possible, so the basic system frame stiffness of 0.4 was used.

6.2.2 Thermal Drift and Thermal Matching

Before data could be taken at any temperature thermal drift measurements were taken and adjustments made to ensure a true thermal matching between the indenter tip and the sample. This is a vital step in the experimental method for hot nanoindentation, as without proper thermal equilibrium between tip and sample a systematic and unmeasurable error is introduced into the system; mostly seen in drift measurements and indentation creep at held loads.

Temperature (°C)		Average Drift (nms^{-1})
20	unirradiated	0·02
20	irradiated	0·03
280	unirradiated	−0·09
280	irradiated	−0·05
480	unirradiated	−0·10
480	irradiated	−0·08
675	unirradiated	0·002
675	irradiated	−0·10

Table 6.1: Average pre and post drift measurements for each data set

After the system has been brought up to the desired temperature the indenter tip is left $\sim 50\mu m$ from the surface of the sample and the system is left to fully stabilise. Once this has been achieved the tip is brought closer to the surface and left briefly to allow for any radiative heating from the sample and stage to settle the temperature of the tip and for an equilibrium to be reached. At this stage a test indentation is performed and the thermal drift pre and post indentation is observed. If this value of indentation drift is over $0.05nms^{-1}$ the temperature of the indentationer is adjusted and further test indentations performed until thermal drift is minimised. In some situations, when thermal drift measurements do not stabilise the system is left for a further $12 - 24$ hours and the process is resumed when the system has settled. The aim is for the indentation drift at high temperatures to equate as much as possible to indentation drift seen at room temperature both in the hot nanoindentation and room temperature nanoindentation machines, which is seen to be $\sim 0.05nms^{-1}$. Drift of the NanoXP system is nominally around this value, although realistically it can vary from $\sim 0.001nms^{-1}$ to $\sim 0.1nms^{-1}$ depending on environmental factors.

Once thermal matching has taken place further changes to the temperature of the system can occur, especially as the tip retracts before moving between indentation locations. This is

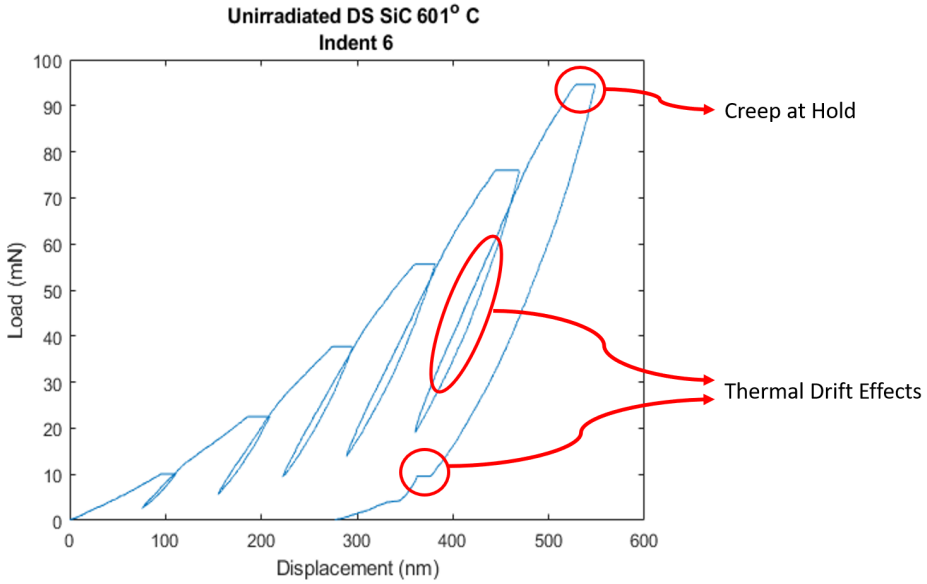


Figure 6.2: An example indentation on unirradiated DS-SiC at 675°C showing the 'pop in' and the end of the indentation and cycle overlap caused by thermal drift. The creep at peak load is also clearly visible.

especially the case at higher temperatures as the small volume of the indenter tip is subject to larger gradients on temperature variance as it moves away from the radiative stage and sample into the relative vacuum. For this reason for each indentation within an experiment a thermalisation time of 2 mins is allowed, although continued stabilisation can be observed during an indentation run, with latter indentations having much lower values of thermal drift. An example of an indentation load / displacement profile is shown in Figure 6.2, this shows how the profile can be significantly changed, especially at high temperature by even a drift of $0.04nms^{-1}$.

The 'pop in' towards the end of the final unload section shows the total amount of thermal drift post indentation; and the cycle load/unload overlap shows a positive drift where the sample is cooler than the indenter tip: a separation of the load/unload curve is seen and a 'pop out' is seen for negative drift. The thermal drift at temperature also increases the creep at each cycle's peak hold, increasing the creep when the indenter tip is higher than the sample temperature. The varying drift measurements for the principle data collection experiment are shown in Table 6.1, and it is interesting to note that minimising thermal drift is not temperature dependant, but often depends on other external and uncontrollable factors. The degree to which thermal drift affects the hardness data is corrected for within the analysis of data, however the larger

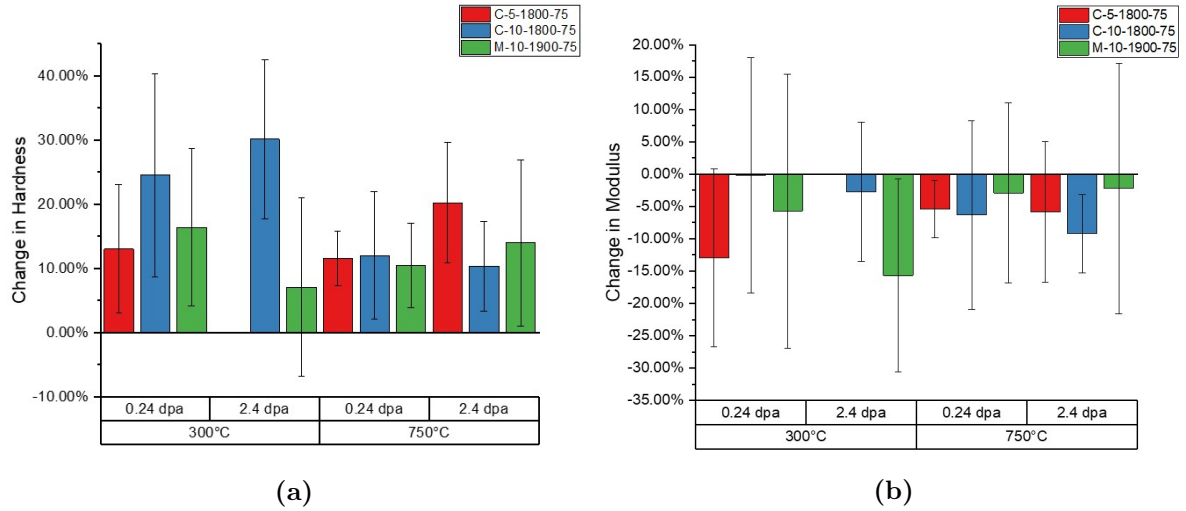


Figure 6.3: Plot showing the relative difference between unirradiated and irradiated materials for elastic modulus and hardness across all irradiation conditions.

the thermal drift the larger the error induced on the hardness measurements, but this error is not fully quantifiable, although is often seen with a higher variance in produced data.

6.2.3 Data collection and selection

Without the CSM feature a major decision on collection of data for this experiment was balancing acceptable data at acceptable depths, whilst still seeing any size effect and change in that with temperature. The length of time each indentation took and temperature stability were also vital factors in considering what form indentations should take, and how many at each temperature should be performed.

Looking at the data collected in the room temperature experiments, it was ascertainable at which point surface effects and size effect were no longer an influence on the unirradiated data at $\sim 200 - 300nm$. Despite this with the ion implantation depth estimated at $1.2\mu m$ it was clear in the elastic modulus data seen in Section 4.3.1 that the bulk was influencing data again at the $1\mu m$ depth of those indentations. These two things together showed a minimum and maximum depth at which we should expect representative values of hardness and modulus. It was felt that it was important to continue to observe any size effect on the data, as this may be a characteristic that is affected by temperature, however it was decided that a maximum depth of $\sim 600nm$ would be sufficient and prevent bulk interactions in the irradiated material. This depth of indentation would also be suitable for observing any change in fracture behaviour

during indentation as shown in Section 4.2, as at room temperature surface fracture was seen at depths $> 400nm$.

It was found in preliminary testing that temperature stabilisation continued and often reached its best after the first couple of indentations, however it did sometimes degrade again during a temperature run if there were external changes including building work, increased foot traffic and other such things which added additional uncontrollable vibrations into the experiments. To minimise these effects it was necessary to only perform indentations overnight, giving a time limit on the number of indentations possible at each temperature. Balancing all of these factors and the need for statistical significance, it was decided that 10 indentations would be performed in each of the irradiated and unirradiated materials in one overnight indentation run. Each indentation would use a load partial unload form equally spreading 6 cycles over the $600nm$ depth of the indentations as demonstrated in Figure 6.2.

Each indentation was set to a maximum depth of $600nm$ with the minimum depth of the first cycle set to $100nm$ An initial indentation load of $0.1mN$ was set with a set loading and unloading rate of $1.5mNs^{-1}$. Analysis was performed with a power law fitting between 100% and 20% of unloading data as advised by the manufacturer using the MicroMaterials software.

Once the experiment was complete some additional data selection was required as occasionally indentations will have been performed on a location with a hole in the material, or when external vibrations were particularly high, causing abnormal load/unload curves. Data also had to be screened for high thermal drift as discussed in Section 6.2.2. All load/unload curves were individually inspected as part of analysis, with data from anomalous runs discarded. Thermal drift measurements were all recorded and data was recorded for each run and screened for within the MATLAB analysis performed.

6.3 Results

As previously mentioned time is one of the largest restricting factors on how much experimental data can be collected. For the preliminary experiment indentations were made at room temperature $\sim 100°C$,$\sim 300°C$,$\sim 500°C$,$\sim 700°C$, however in the principle data set the $\sim 100°C$ temperature run was not possible due to time constraints.

For each indentation set a temperature is quoted and used in these results. The temperature

of the indentation is taken to be the temperature detected by the indenter tip thermocouple. This is deemed to be the most accurate of the thermocouples in the system as it is measuring the smallest volume, and is the only one close to the indentation location and in the indentation profile itself. This temperature is also closely monitored during the thermalisation process, and tends to remain at a steady temperature once thermal drift has been minimised, further confirming its accuracy. Despite this these temperatures may not be fully accurate, with the largest difference between stage temperature and indenter tip temperature seen when approaching the high temperature limit of the machine, which during these experiments has been ~ 700°C. The largest variation of readings from the thermocouples showed the stage at 850°C, the sample at 601°C and the indenter tip at 675°C. It was decided that the sample thermocouple was not sufficiently in thermal contact with the sample in this experiment, and that there may have been some remaining cement dust beneath the sample on the stage preventing a perfect thermal contact between the sample and the stage. This would also explain the higher stage temperatures as the lack of good thermal contact will have prevented efficient sample heating. It is also possible that after years of use the sample thermocouple has become damaged as it is manipulated for contact with the sample and cemented down for each new experiment.

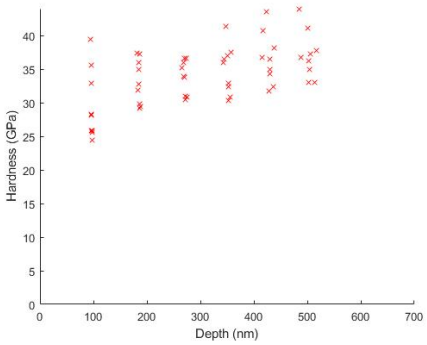
For the primary data set, the temperatures used were: 20°C, 280°C, 480°C and 675°C.

6.3.1 Size Effects

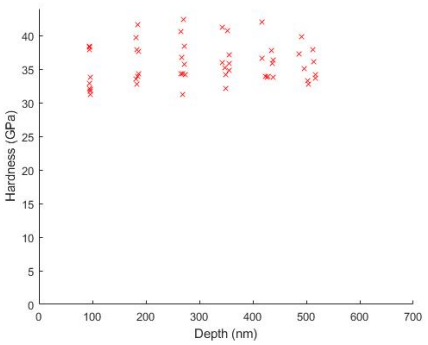
Before any bulk properties could be ascertained, investigations were made into any size effects seen with these indentations. This then allowed for values as close to bulk as possible to be used to give bulk material characteristics.

The cyclic indentation profiles gave varying modulus and hardness measurements at depths for each indentation. Although the software was set to aim for specific depths there was a variation in the depths achieved on each cycle, allowing for well populated plots observing hardness as a function of depth.

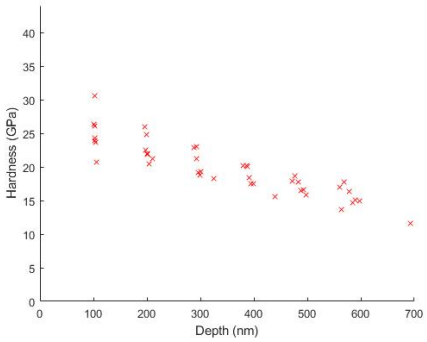
At room temperature there is no clear size effect seen at all, confirming what was seen in Chapter 4, with no discernible difference seen looking at size effects in the irradiated sample. Looking at increased temperatures as seen in Figure 6.4 we can see that unirradiated material hardness at elevated temperatures has a clear and significant dependence on depth. The irra-



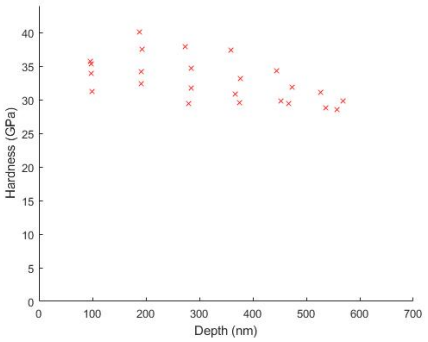
(a) Unirradiated DS-SiC at RT



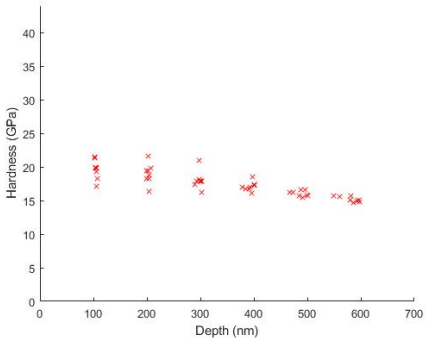
(b) Irradiated DS-SiC at RT



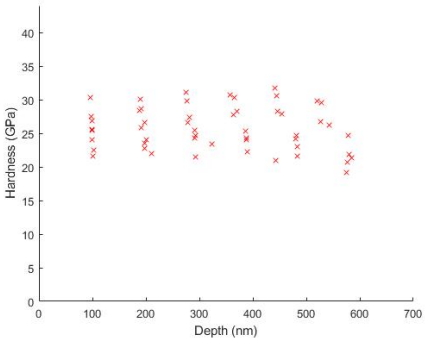
(c) Unirradiated DS-SiC at 280°C



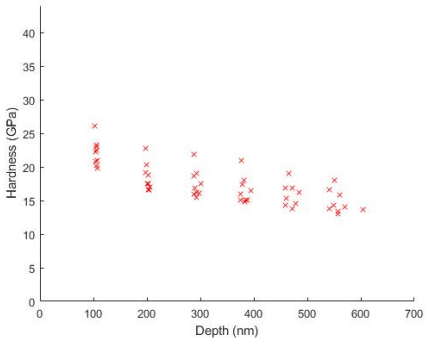
(d) Irradiated DS-SiC at 280°C



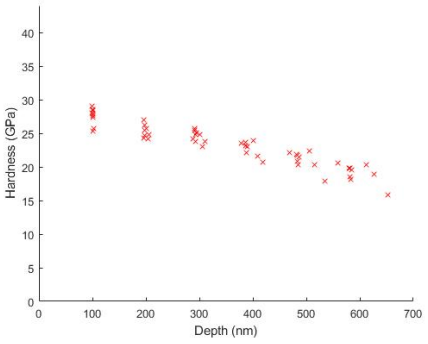
(e) Unirradiated DS-SiC at 480°C



(f) Irradiated DS-SiC at 480°C

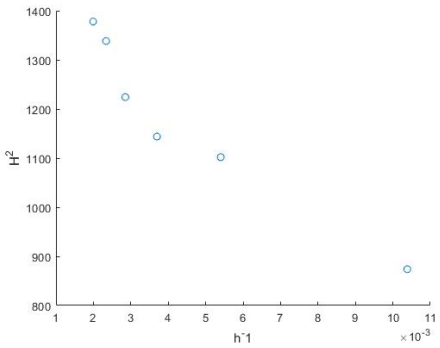


(g) Unirradiated DS-SiC at 675°C

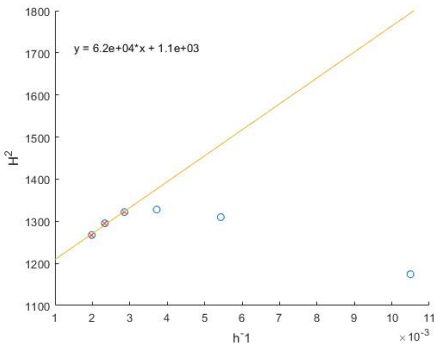


(h) Irradiated DS-SiC at 675°C

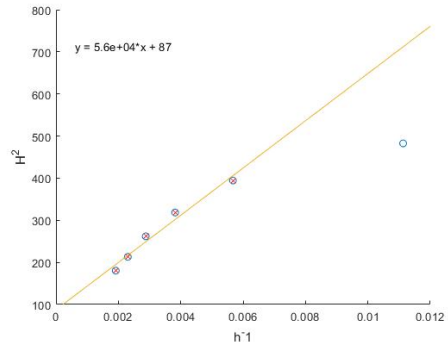
Figure 6.4: Plots showing the depth dependance of hardness with temperature and irradiation condition. The unirradiated material at higher temperatures showing a much stronger depth dependance than the irradiated material, although increased depth dependance is seen in both with temperature. Each data point represents a value calculated from a single cycle within each indentation run



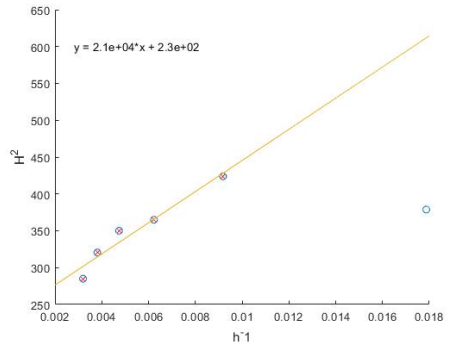
(a) Unirradiated DS-SiC at RT



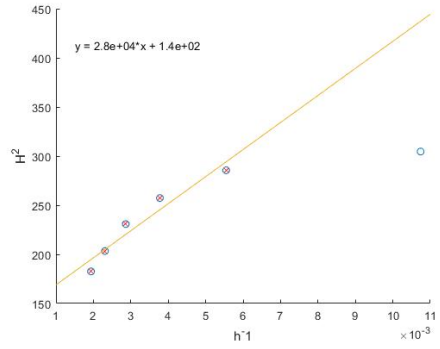
(b) Irradiated DS-SiC at RT



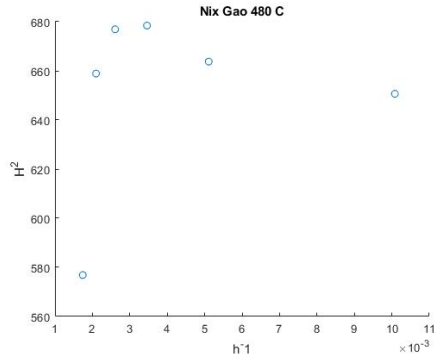
(c) Unirradiated DS-SiC at 280°C



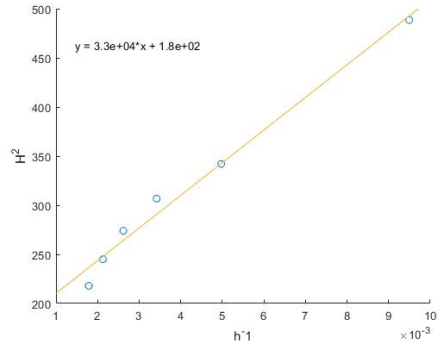
(d) Irradiated DS-SiC at 280°C



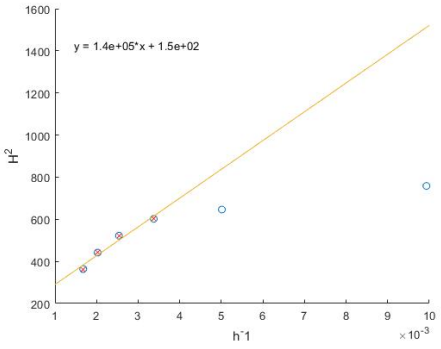
(e) Unirradiated DS-SiC at 480°C



(f) Irradiated DS-SiC at 480°C



(g) Unirradiated DS-SiC at 675°C



(h) Irradiated DS-SiC at 675°C

Figure 6.5: Nix-Gao plots showing the depth dependance of hardness with temperature and irradiation condition. The unirradiated material generally showing a good relation, where it is showing a much stronger depth dependance than the irradiated material, although increased depth dependance is seen in both with temperature.

diated material hardness shows a lesser dependence on depth than the unirradiated material, however a size effect can still be observed, with this depth dependence generally increasing with temperature. The highest temperarature irradiated sample shown in Figure 6.4h shows the largest size effect.

Given the clear size effects it was decided that further analysis of these results was required. The best way at looking at size effects in nanoindentation is using a Nix-Gao analysis. This was performed to observe the elastic/plastic nature of these indentations further and to look for characteristic hardness [235]. Analysis was performed using the Nix-Gao equation shown in Eq 6.1 where H is a given hardness at a given indentation depth of h, giving a characteristic depth dependence of hardness in h^*, where H_0 represents the hardness resulting only from the statistically stored dislocations. These empirical values are designed to get an overall impression of size dependent hardness.

$$\frac{H}{H_0} = \sqrt{1 + \frac{h^*}{h}} \tag{6.1}$$

Plots were produced showing H^2 against $1/h$ as shown in Figure 6.5, with the aim of looking for the characteristic linear behaviour of the Nix-Gao model and to calculate H_0 and h^*. It is clear that in general none of these plots show a good linear relation through the whole depth of indentation, with some variables showing no linear relation at all. The lack of linearity is mainly seen in the surface layer of the unirradiated layer where it may be being skewed by surface damage. For those plots with some linearity, the linear portions were plotted to give the relation seen in Equation 6.1. These allowed for the observation of the characteristic depth dependence of hardness varying with temperature to be seen in the unirradiated material as summarised in Table 6.2, with relatively good R^2 values showing these values fit well with the data provided. The unirradiated room temperature test is behaving in the opposite manner with an increase in hardness being seen with depth. While a good physical meaning for this has not been found, it is thought that the extensive fracture mechanisms occurring in the room temperature tests, especially with multiple 'pop in' events, may be the cause.

A clear correlation with temperature is seen, with the characteristic depth for hardness reducing with temperature, and thus the hardness from the statistically stored dislocations increasing with temperature. With no acceptable equivalent for the irradiated material a full

Temperature (°C)	H_0 (GPa)	h^*(nm)	R^2
RT	N/A	N/A	N/A
280	8.4	644	0.988
480	11.8	200	0.958
675	13.4	183	0.985

Table 6.2: Nix-Gao analysis showing effect of temperature on size effect in unirradiated DS-SiC including the R^2 values to show fit to the data

description of size effect is not possible however, with the Nix-Gao analysis in conjunction with the simpler results showing the depth dependence of hardness, conclusions can be made that the smaller cycle depths for each indentation will not be producing a representative data set. As the Nix-Gao analysis did not show size effects at shallower depths in the same way as modelled, it is clear that further mechanisms not considered in the traditional room temperature model are at play.

Given the good linear fit to the data it is postulated that the Nix-Gao Equation 6.1 is not suitable for establishing size effects in this type of data, in the same way it would be for looking at room temperature data. This is likely due to a change in damage mechanisms taking place at the higher temperatures. The Nix-Gao Equation 6.1 is dependant on what they call 'statistically stored dislocations', i.e. those not directly created by the indentations themselves, but inherent in the material citeNix1998. With the increasing temperatures in this experiment, the type and number of these 'stored' dislocations will be reducing as some form of annealing will be taking place. In addition to this the created dislocations could have the opportunity to anneal out during the indentation process. This could explain the 'size effect' seen, where s a change in created dislocations and a reduction in 'stored' dislocations lead to a reduction in hardness with depth.

6.3.2 Bulk Properties

Given the size effects seen at all temperatures and with values not always settling to a representative bulk measurement decisions were made given the data available regarding how to calculate bulk characteristics. It was shown that the there are varying characteristic depth dependencies on hardness, however given the need for consistency across all data sets, and the lack of a linear relationship seen at the larger indentation depths, it was decided that only the

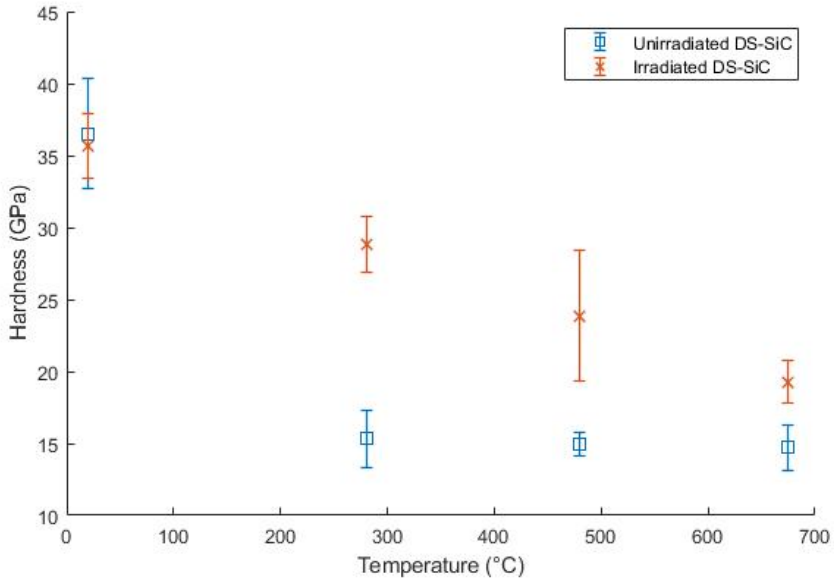


Figure 6.6: The effect of temperature and irradiation on indentation hardness of DS-SiC irradiated with Si ions to a peak of 3.9dpa at 300°C. Error bars represent one standard deviation in the measured hardness. The unirradiated material plateaus to a hardness of $\sim$ 15GPa by 280°C however the harder irradiated material is still seen to be reducing. Standard deviations are given as errors.

last cycle of indentations would be taken to give good representations for the bulk material characteristics.

Bulk indentation hardness as a function of temperature is shown in Fig 6.6. We know that room temperature readings produced in this data set will not be as accurate as the data acquired using the NanoXP, due to the lack of CSM and the relative size of the data set creating much larger errors. This gives reason for the similar room temperature values for hardness of 36GPa, the error being larger than the 4GPa increase in hardness seen in the NanoXP data. The trend of irradiation induced hardening is continued here, with the degree of hardening at first increasing, with the irradiated material being 13GPa harder than the unirradiated at 280°C. We then see a reduction of hardness with temperature approaching that of the plateaued unirradiated hardness, with the hardness effect at 675°C reducing back to the 4GPa we saw in the room temperature experiments. The much larger error seen in the irradiated data at 480°C is due to increased drift in the system caused by road maintenance, and shows the degree to which any vibrations can effect results. The absolute values of increased hardness are interesting, however the percentage increase gives us a much better picture of these effects, where at 280°C there is $\sim$ 88% increase in hardness, this reduces to an increase $\sim$ 60% at 480°C and $\sim$ 31% at

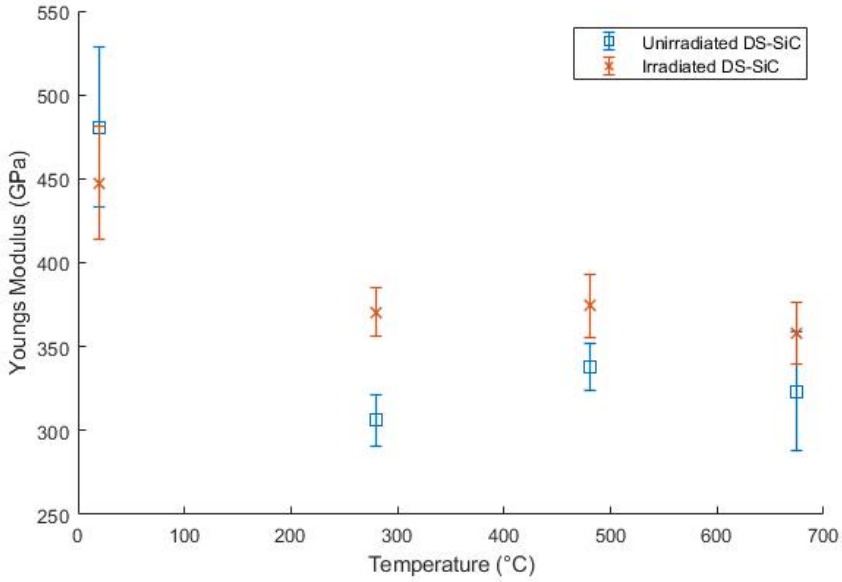


Figure 6.7: The effect of temperature and irradiation on Youngs modulus of DS-SiC irradiated with Si ions to a peak of 3.9dpa at 300°C. Error bars represent one standard deviation in the measured hardness. The reduction of modulus seen at room temperature is not seen at the higher temperatures, with both the unirradiated and irradiated material plateauing at 280°C to a youngs modulus of $\sim$ 374GPa for the irradiated material and $\sim$ 320GPa for the unirradiated material. Standard deviations are given as errors.

675°C. This increased hardness effect is clearly reducing, however with such a high increase of hardness even at 675° there is clearly a retention of the radiation damage in the material.

All modulus from the MicroMaterials hot nanoindentation system were given as reduced modulus. To allow for better comparison with other data all reduced modulus values were converted to elastic moduli as described in Section 3.3.

Irradiation had an interesting effect of reducing the modulus of all SiC samples in room temperature tests on the NanoXP as discussed in Sections 4.3.1 and 4.4.1, and this is seen in the room temperature data on the hot nanoindenter as well. The effect of temperature on the elastic modulus is seen in Fig 6.7. The reduction in modulus characteristic to SiC at room temperature is no longer seen at these higher temperatures, instead the elastic modulus is seen to be $\sim$ 50GPa larger in the irradiated material than the unirradiated material at all temperatures here, with both plateauing in this data at 280°C. Looking again at the percentage increases in elastic modulus we are seeing a $\sim$ 21% at 280°C, but only $\sim$ 11% increase in elastic modulus at higher temperatures.

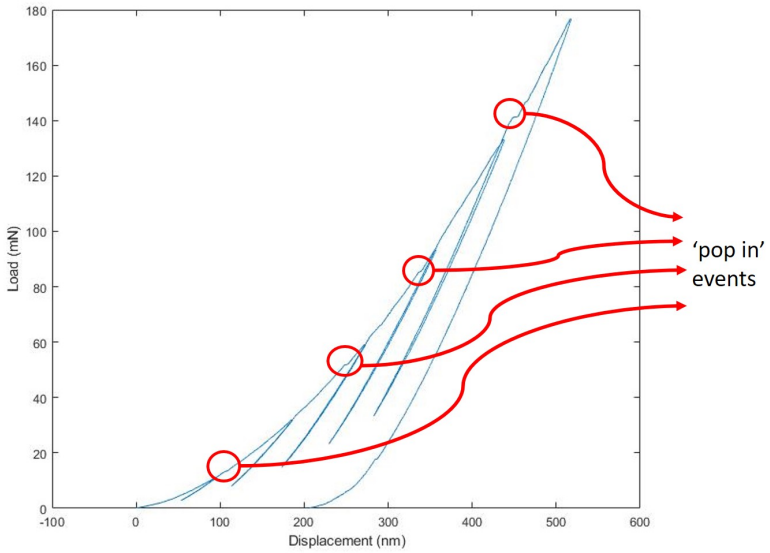


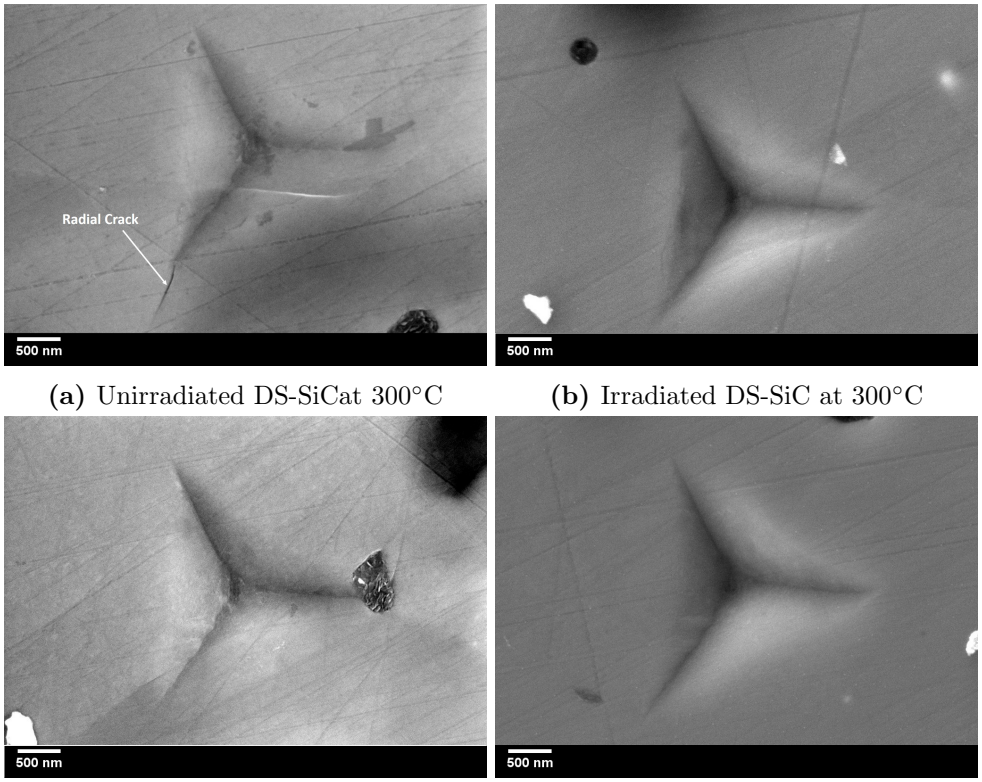
Figure 6.8: An example of a Room Temperature indentation on unirradiated DS-SiC showing multiple 'pop in' events in comparison to the indentation profiles produced in the NanoXP

6.3.3 Fracture Behaviour

Room temperature fracture behaviour of irradiated and unirriadiated DS-SiC was heavily investigated in Section 4.4.1, showing vast changes in the fracture behaviour induced by the Si ion irradiations. Here this study has been further investigated, looking at how indentation temperature has effected fracture behaviour in DS-SiC.

The first problem encountered was that although the size of indentations were made to a depth at which fracture events always occurred in the NanoXP, the slower strain rate used for these indentations inherently changed the fracture behaviour, as the material had more time to adjust to the deformation. This meant that where no instant fracture events were evident in the room temperature load/displacement curves on the NanoXP, 'pop in' events were evident in various indentations, both unirradiated and irradiated using the hot nanoindentation system as seen in Figure 6.8. It is possible that the reason these 'pop in' events are seen here is due to the load/unload process giving the material some recovery, rather than allowing for continuous crack growth. These may lead to the bizzare Nix-Gao behaviour previously discussed in the room temperature tests.

Looking directly at the hot nanoindenter room temperature indentations in the SEM the fracture is qualitatively the same as we saw in the NanoXP, with indentations in the unirradiated



(a) Unirradiated DS-SiCat 300°C **(b)** Irradiated DS-SiC at 300°C

(c) Unirradiated DS-SiC at 500°C **(d)** Irradiated DS-SiC at 500°C

Figure 6.9: SEM images of indentations exhibiting fracture behaviour at 300°C and no fracture behaviour at 500°C in unirradiated and Si ion irradiated DS-SiC enhanced to show fracture clearly.

material showing radial fracture from the corners of the indentation, and some lateral cracks in the indentation surface. The indentations in the irradiated material showed no radial fracture, but did continue to show the lateral fracture in the indentation itself. This consistency with both machines across the varying strain rate however does allow us to say that any strain rate effects on the fracture behaviour seen here is minimal.

Characteristic fracture behaviour was seen across all unirradiated indentation experimental runs up to a temperature of $\sim$ 300°C, however by the next temperature of $\sim$ 500°C these characteristic cracks were no longer seen, as shown in Fig 6.9. It is also clear in these SEM images that the indentations in the irradiated material are 'sharper' and more distinct, where the edges of the indentations are more uneven in the unirradiated samples, with this characteristic consistent across temperatures. This effect is enhanced here with the unirradiated SEM images being 'In Lens' and the irradiated images a Secondary Electron Image (SEI) as these settings gave the best contrast to see features, however this effect was visible when all the images were in the same conditions as well. 'In lens' images are not shown for the irradiated material as

the optical differences noted in Chapter 4 between the irradiated and unirradiated material prevented in lens electron diffraction from occurring at a level that gave clear images.

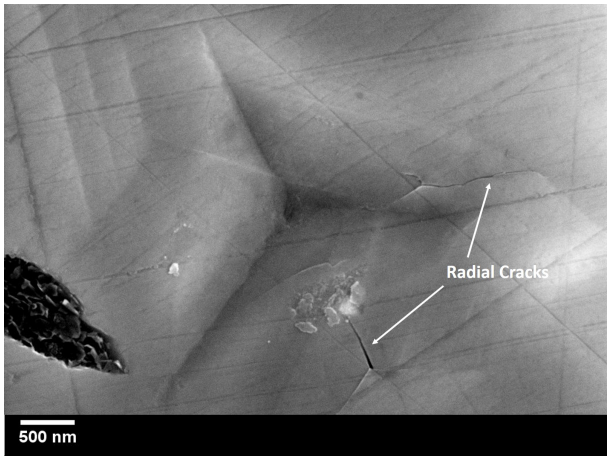


Figure 6.10: An In lens SEM image of DS-SiC indented at 600°C showing fracture, and some grain structures

There were however a few outliers to the generalisation of the fracture behaviour with some fracture behaviour evident in the $\sim$ 600° indentations, more characteristic of single crystal fracture seen by Bo-Shiuan Li [236], where in the single crystal nanoindentation dominant slip systems led to shear occurring at higher temperatures, likely either on the basal plane or the pyramidal $\langle c + a \rangle$ slip systems as predicted by K.Ho et al [152]. An example of such an indentation is shown in Fig 6.10. This indentation also shows some grain structure with twins seen in the top left hand corner. These features are of note as grain structures on DS-SiC were not visible on other samples, but are visible after being heated.

6.3.4 Recovery Mechanisms

As mentioned briefly already there is evidence that during these experiments at elevated temperatures that annealing is taking place, allowing some of the microstructure to recover. Idris et al [121] reported that as the annealing temperature exceeded the irradiation temperature swelling, in the irradiated material began to be eliminated, with recombination of interstitial atoms and vacancies however continuing to be relatively slow but continuous up to the maximum annealing temperature of $\sim$ 1473K. The temperatures seen in this hot nanoindentation experiment were no-where near as high, and were not at temperatures above the irradiation temperature of 300°C for more than 36hrs, whereas in Idris et al's work had increments of 50K up to the highest temperature and were held for 6hrs each. Despite this some recovery has clearly occurred in this study. Kerbiriou et al's study [237] has even reported dynamic annealing happening during irradiations at higher temperatures preventing larger amounts damage accumulating in the material.

In contrast Gosset et al [105] report that their nanometric 3C-SiC is healed only after annealing to 1000°C, and none was seen at the previous annealing temperature of 900°C. This is very difficult to compare with this study as the nanometric nature of the material in their study changes the way damage accumulates and how it can move within the lattice. Although many studies in the literature discuss annealing, the vast majority are focussing on material that has amorphised under irradiation, so are not relevant for comparison with this work.

It therefore appears that as the temperature is increased in this study, diffusion of the defects caused by the ion implantation is becoming more easy as there is more thermal energy in the system. Recombination of vacancies and interstitials is more likely to be taking place, and dislocations are more likely to be able to diffuse to grain boundaries or surfaces. This is allowing for some recovery to take place, although not as much as would occur at higher temperature annealing. Given the nearing of temperatures to an operational temperature this phenomena could be critical in understanding how much damage remains in the material.

6.4 Discussion

Some clear conclusions can be drawn from this work, allowing for a good characterisation of ion irradiation damage on material properties of DS-SiC at temperature. With Si ion irradiated material maintaining an increase in hardness and showing an increased elastic modulus at elevated temperatures compared to unirradiated samples due to the damage induced.

It is clear that as temperature begins to increase, although the bulk material has a reduction in properties, the effect of the ion implantation is enhanced greatly, with the hardness almost double that of the unirradiated material at 280°C. This is showing that despite the additional dislocation mobility allowed by the increased temperature which is causing the bulk reduction in hardness and modulus, the various induced damage mechanisms are not showing the same mobility. It is postulated that in increased dislocation density seen in the Transmission Electron Microscope (TEM) studies in Section 4.3.3 are not fully mobilising, and those that are combining are restricting slip and therefore increasing the hardness of the material. It is also postulated that the irradiation has created more point defects and clusters, which at higher temperatures are preventing dislocation mobilisation and making the irradiated material effectively harder [238]. An increase of the mobility of the additional Si ions introduced in the irradiation process

may also be at play with the energy available for these interstitials to mobilise into vacancy gaps and into the main matrix lattice. Without a better understanding of the dislocation dynamics in these samples it is difficult to pinpoint the origins of the hardness mechanisms at play here, however as it was not possible to do TEM work further than that performed in Section 4.3.3 these assumptions must be made.

The fast drop in hardness seen in this study is unexpected, and does not fit well with other high temperature nanoindentation studies done on other forms of SiC as shown in Figure 6.11, however it does fit with the preliminary studies done in this work, with the DS-SiC bulk sample tested with a blunt tip even matching this trend. Although the exact values are not relevant here, as the tip was almost a flat punch (Figure 6.1), so the analysis methods based on the Oliver / Pharr nanoindentation model [**?**] are not valid, the results can be used as a good first approximation and the large reduction in hardness with temperature is clear. This implies that there are additional mechanisms at play in this DS-SiC than the CVD SiC and TRISO coatings studies [133, 239, 240]. The polycrystalline nature of the DS-SiC in comparison to the single crystal 6H-SiC study [236] would predict a lower hardness for this work. It is also of note that this work is on predominantly 6H-SiC where the Rohbeck samples were all β-SiC (3C) and a significant difference is well known between α and β SiC as discussed in Chapter 2.

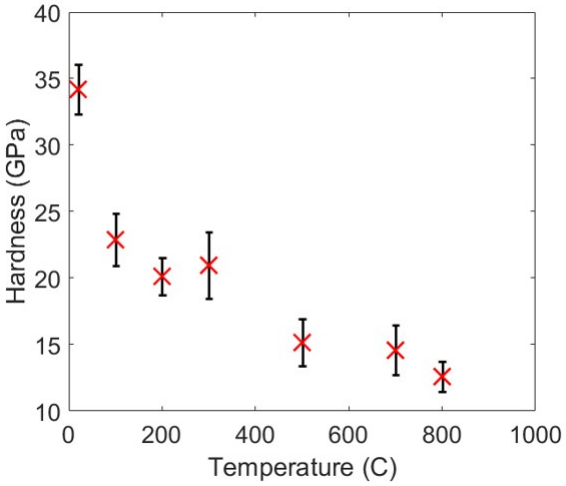
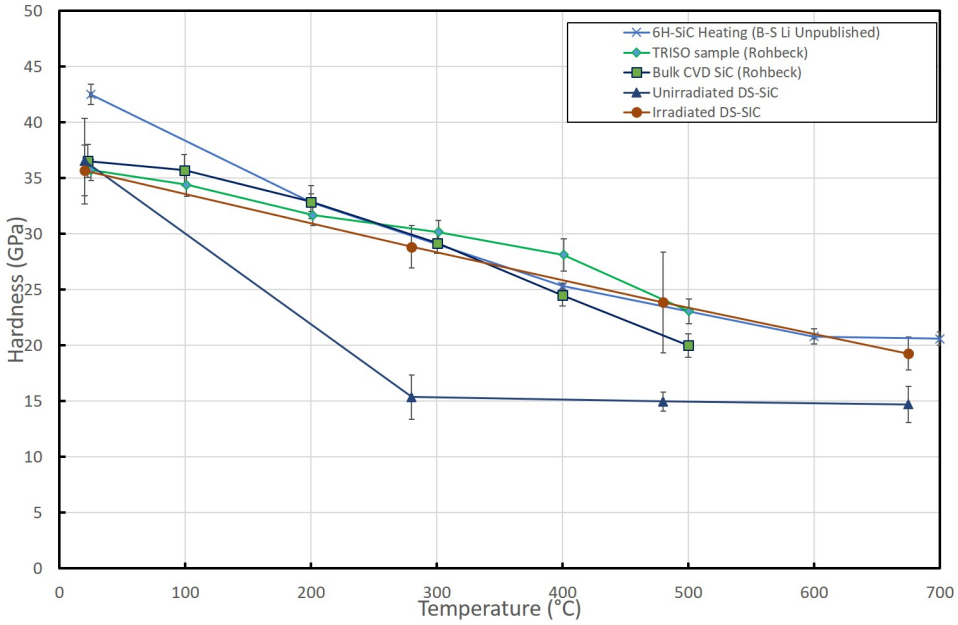
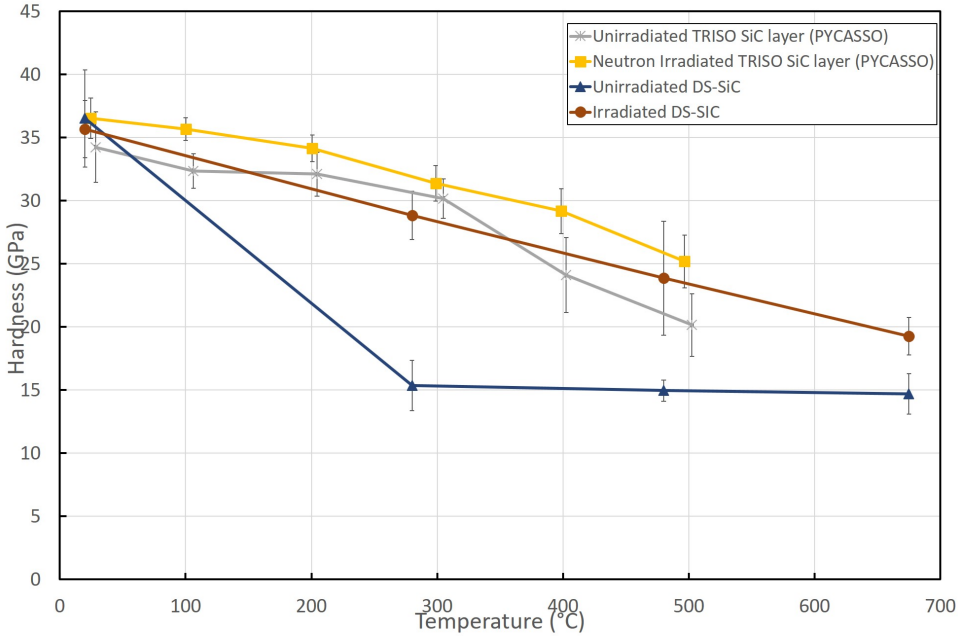


Figure 6.12: Results from a pelimenary experiment with blunt indenter tip on unirradiated DS-SiC, showing fast drop in hardness with temperature. Standard deviations are given as errors.

In general it is known that as temperature increases we would expect a reduction in the effects of the radiation damage because the increased number of defects caused by the ion irradiation are mobilised as the temperature of the material increases. Shen at al's study showed that lattice damage was significantly removed after annealing at 30mins at only 600°C. We would also expect diffusion of dislocations to occur at an increasing rate across the boundary into the bulk material beneath the layer to which the ion implantation damage reached. Snead et al [241] studied the stored energy release in neutron irradiated SiC, and after a furnace hold of 700°C



(a)



(b)

Figure 6.11: Plots showing various effect of temperature on hardness: in single crystal 6H-SiC [236], a SiC layer in TRISO fuel particle and Bulk Chemical Vapour Deposition (CVD) SiC [239] and in this work 6.11a ; and the neutron radiation study on the TRISO SiC layer [240] in comparison to this work 6.11b. A consistency is seen, although this work generally shows a reduced hardness in comparison to the literature. Irradiation effects are more pronounced in this work, and the irradiated DS-SiC in this work shows the best correlation to the literature high temperature studies.

expected recombination of thermally activated defect recovery, and showed that 74% of the defect recovery in their work was due to C-Frenkel pairs in both 3C-SiC and 6H-SiC samples. The long time periods that the sample in this work was held at temperature would also allow for various defect recoveries. It is known that the C-Frenkel pairs are some of the lowest thermally activated of the defects seen in SiC [188], and these defects were seen to recover in Shen et al's work as well, however with the added pressure and energy induced by the indentation we would expect other defects to recover especially at the highest temperature indentation.

These well known effects can be looked at in conjunction with the size effect observations in this study. With the Nix-Gao analysis proving to be insufficient to fully explain the effects we look to dislocation dynamics to explain these high temperature effects. The Nix-Gao model works from the basis of statistically stored dislocations providing the length scale of hardness size effects, however as we elevate temperature we will also see a change in the behaviour of these statistically stored dislocations, with the combination of indentation pressure and the higher temperature allowing for further mobilisation of dislocations, where surface effects can dominate at low depths reducing the freedom of movement of the dislocations, as the indentation becomes deeper this is enhanced, reducing the linearity of the Nix-Gao effect. This gives a good explanation of the size effects in the unirradiated material, however the behaviour is affected even more by the introduction of radiation damage. In addition. as the temperature increases a larger hardness size effect is visible: here we are seeing the effect enhanced as we have a greatly increased mobility between the irradiated layer and unirradiated bulk beneath reducing the depth at which we are truly measuring the hardness of the irradiated material not the bulk. This diffusion is likely of both dislocations, defects and the Si interstitials introduced in the ion irradiation. The enhanced linearity of the reduction of hardness with depth of the irradiated material at 675°C as seen in Figure 6.4e would support this theory. The effect will be causing an increased underestimation of hardness with temperature, at this stage this effect is not quantifiable, however it is expected that a shallower gradient in the reduction of hardness of irradiated material with temperature would be more accurate. This is an inherent problem with ion implantation but as it is by far the quickest and easiest way of studying radiation damage modelling of such phenomena would be very useful.

It is well known that at room temperature radiation damage is seen to create lattice swelling

in SiC [74, 242], as seen by the decrease in elastic modulus, also seen in the room temperature work presented in Chapter 4. One of the principle mechanisms of this in the ion irradiation studies is the additional Si interstitials introduced by the Si implantation. As the change of modulus with temperature is studied, this decrease in elastic modulus in irradiated material is no longer visible, with a more traditional increase in elastic modulus being seen. This implies again that there has been a mobilisation of Si interstitials. The increased energy present in the system in combination with the point defects and clusters discussed earlier with regards to the increase in hardness with temperature then come into effect causing the increase in elastic modulus of the irradiated material in comparison to the unirradiated bulk.

Another feature seen post the high temperature nanoindentation was the distinctive nature of the microstructure becoming visible in the SEM in both the unirradiated and irradiated material. This is showing a similar effect as seen in annealed samples in the literature, where surface re-crystallisation has occurred [243], as well as the high temperature implantations in this work where grain structures became more pronounced as discussed in Section 4.4.1. The TEM work performed in Section 4.3.3 showed that no amorphisation had occurred in the irradiated material despite the loss of a crystalline raman signal. This appearance of a clear microstructure post an 'annealing' process suggests that the very surface of the material may indeed have been amorphised. With the known amorphisation threshold to be 1dpa for neutron irradiated samples [241], and the variations in this critical threshold caused by dose rate, ion implantation and temperature it is not unexpected that some amorphisation could have taken place, and that this $< 10nm$ surface has recrystallised post hot nanoindentation. It is clear that a change in behaviour of the irradiated SiC has occurred during the hot nanoindentation process akin to that of an annealing process, and further studies on this would be pertinent.

6.5 Summary

This work is an important step forward in understanding the mechanical properties of SiC at operational relevant temperatures, including how radiation damage effects are altered. This study has shown that any hardness determined by the high temperature nanoindentation system is seen to reduce with temperature in line with literature data, and that the effect of Si ion irradiation damage to 2.4dpa performed at 300° is seen at first to increase with temperature then

slowly reduce again, with the increased hardness at 675°C still a larger increase in percentage of the unirradiated material than seen at room temperature. This is believed to be due to the dislocations slowly gaining energy to move, which increased the response to compression.

The effect of increased temperature nanoindentation has changed the behaviour of the elastic modulus of the irradiated material, from reduction of elastic modulus in room temperature studies to a larger percentage increase of elastic modulus with irradiation at higher temperatures. All of these effects are likely due to the enhanced effect of point defects and decreased mobilisation in the Si implanted material in comparison to the unirradiated bulk. This increase of elastic modulus in comparison to the unirradiated material is especially of note when looking at tolerances for SiC as it becomes an engineering material.

Significant size effects are also seen, increasing with temperature with fewer size effects evident at lower temperatures in the irradiated material, until at 675°C where increased mobility of defects and dislocations into the unirradiated bulk are being seen. These size effects seem to show that standard Nix-Gao analysis is not suitable when looking at size effects with elevated temperature, and this new result will need further investigation.

Chapter 7

Summary, Conclusions and Future Work

7.1 Summary

The potential nuclear fusion uses of silicon carbide have been widely considered, however after a comprehensive review of the literature it was clear that there were distinctive areas which required further investigation. The principle problem found was the lack of direct comparison available between different irradiation studies: where there are so many variables with both SiC polytpes and materials, as well as with the irradiation conditions themselves pinning down where origins of behaviour changes were became almost impossible. Along with this the focus in much of the literature had been looking at microstructural changes under irradiation, without looking at the mechanical changes they then caused. This project focused on looking at changes in mechanical properties with varying irradiation conditions, allowing for the direct comparison of results across the project to look at how different levels of irradiation damage effected mechanical properties in different ways.

A vast amount of the previous SiC studies were using either single crystal or Chemical Vapour Deposition (CVD) monolithic materials, which are both slow to make and expensive. This project took a different approach and looked at radiation effects on currently available commercial materials, which are likely to be easier to develop for engineering materials for nuclear fusion applications. In addition to this the project investigated the Transient Eutectic-Phase (TEP) fabrication method for production of both monolithic and composite materials, which allowed for material to be followed from fabrication to evaluation of radiation damage, and for changes in behaviour to be pinpointed to single variables.

Before any radiation studies were performed baseline properties were investigated to allow for better understanding of the changes brought on by implanted damage. The three commercially available materials, Reaction Bonded SiC (REFEL), Hot Pressed SiC (HP-SiC) and

Direct Sintered SiC (DS-SiC) were seen to have very similar hardness and elastic modulus behaviours, and they all manifested similar behaviours in fracture around nanoindentation, with significant subsurface fracture seen in DS-SiC. The fabricated TEP samples were tested using four-point bend tests as a macroscopic evaluation technique, along with the use of X-ray Computed Tomography (XCT) and Scanning Electron Microscope (SEM) techniques to help evaluate the whole range of materials produced. It was found that composite materials heated to 1900°C during the hot pressing process lost all composite behaviour, and the fibres were no longer visible as distinct fibres with Pyrolitic Carbon (PyC) interphase layers and matrix amalgamating to create a monolithic sample. It was found that samples produced with 10%wt sintering agents, had large remnants left in the microstructure after fabrication, which in many samples created paths for fracture, especially in monolithic samples hot pressed to 1900°C for 60mins. Three of the best samples C-5-1800-75, C-10-1800-75 and M-10-1900-75 were selected for further investigations of %wt of sintering agents to be performed. Nanoindentation studies on these samples showed the 5%wt composite matrix to have slightly higher hardness and elastic modulus than the 10% sample, and both were higher than the monolithic sample, however all fell within similar values to the commercially available materials. Fracture behaviour after nanoindentation proved similar between the fabricated TEP samples and the commercially produced samples, with extensive radial fractures from the indentation corners as well as cracks lateral to the indentation surface seen. The REFEL and M-10-1900-75 samples both exhibited material pop out from slip at grain boundaries.

A selection of silicon ion implantations were performed on the materials under 4 conditions: temperatures of 300°C and 750°C and doses leading to 0.24 and 2.4 displacements per atom (dpa). The initial 300°C 2.4dpa study was performed on all three commercially available materials, which led to irradiation induced increases in hardness and reductions in elastic modulus across all samples. All further Si ion implantations were performed on DS-SiC, and all three of the TEP fabricated materials, and the same trends of increased hardness and reduced modulus were seen across all material types. The DS-SiC material showed its largest reduction in modulus under the low dose, low temperature irradiation, and its smallest reduction in modulus under the high dose, high temperature irradiation. Conversely the largest increase in hardness was after the high dose, high temperature irradiation and the smallest increase in hardness was

seen after the low dose, low temperature study. When looking at the TEP fabricated materials the effects of the irradiations were generally lesser after the high temperature irradiations. The C-10-1800-75 sample showed the largest increase in hardness of any of the materials with a $\sim 30\%$ increase in hardness being observed after the irradiation at 300°C to 2.4dpa. the largest decrease in modulus seen was the M-10-1900-75 sample under the same conditions, where a $\sim 16\%$ reduction in modulus was seen. The behaviour of the monolithic and composite samples with the same %wt saw very different behaviour under irradiation, showing that the matrix of the composite is behaving in a different manner to equivalent monolithic material. A final neon implantation at 300°C to 2.4dpa was performed on DS-SiC and was able to show almost identical changes to hardness and elastic modulus as seen in the silicon ion implantation under the same conditions.

Across the irradiation experiments on all samples nanoindentation surface fracture was suppressed: no radial fracture was visible on any of the materials, and only the lateral cracks around the indentation surface were seen. The only condition which did not fully show this was DS-SiC under the 750°C 2.4dpa where minimal radial fracture could be seen. Suppression of surface fracture was generally seen as an effect of residual stresses being induced in the materials with implantation. The self-annealing seen in samples irradiated at 750°C to 2.4dpa, especially in the nanoindentation results in DS-SiC was seen to allow some fracture to occur in that sample. Cross sections were taken across indentations in the DS-SiC material irradiated at 300°C to 2.4dpa, and extensive sub-surface crack networks were visible, these cracks seemed more complex that those seen in the unirradiated material. The top layer which contained the irradiated material showed virtually no fracture, and acted like a thin film on top of the unirradiated bulk, amplifying the fracture effects into the bulk material beneath. Fracture around nanoindentations was also investigated after hot nanoindentation studies, where characteristic radial fracture was seen around unirradiated indentation up to temperatures of ~ 300°C, however none were present after the ~ 500°C indentations. No fracture was seen around any of the irradiated indentations at any temperatures.

Along with the mechanical changes, optical properties of the materials were also altered, and briefly investigated. Changes to the surface of the material were clearly visible with the naked eye, where the blanked unirradiated portion of the samples was clearly different to the

irradiated portion. This effect was seen in the SEM and in cross sections in the Transmission Electron Microscope (TEM). Using raman spectroscopy, characteristic 6H-SiC peaks seen in the unirradiated material were not visible in the 300°C 2.4dpa sample, instead low intensity peaks showing the Si-Si and Si-C bond were seen. Qualitative TEM studies showed a crystalline irradiated material, with a large increase in defect density in the irradiated material, where the 300°C 2.4dpa neon and silicon irradiations showed very similar effects.

The hot nanoindentation study enabled testing of mechanical properties up to low in-service fusion temperatures. While obvious indentation size effects were seen in the unirradiated materials across the temperature range, and examined using Nix-Gao analysis, such effects were not seen in irradiated indentations. The Nix-Gao analysis proved insufficient for understanding of the behaviours at temperature, leading to belief that additional mechanisms are at play which are not considered within the Nix-Gao model. The large amounts of fracture seen at room temperature in the unirradiated material likely caused the bizarre increase in hardness seen in that indentation set. While unimplanted material dropped in hardness significantly from the $36GPa$ seen at room temperature to a plateau of about $15GPa$ at ~ 300°C. The irradiated material has a gradual reduction in hardness across the range investigated, where the irradiated sample was $\sim 88\%$ larger than the unimplanted material at ~ 300°C, the increase was $\sim 60\%$ at ~ 500°C and $\sim 31\%$ at the highest temperature of 675°C: while the effect of the radiation damage is lessening with temperature there is still some retention of damage. Looking at the change in elastic modulus with the hot nanoindentation, while decreases in elastic modulus were seen at room temperature across all samples studies, by ~ 300°C the elastic modulus is higher in the irradiated samples. The elastic modulus of the unirradiated sample drops from $\sim 450GPa$ at room temperature to $\sim 300GPa$ by ~ 300°C, at which point the irradiated material is seen to be $\sim 50GPa$ higher. While there is some further change above this temperature (the same temperature as the implantation temperature) both the unirradiated and irradiated materials effectively plateau at this point. These hot nanoindentation studies also fit well with the few literature values of hot nanoindentation studies.

This work has led to some key results, manifested across the separate studies. One of the principal findings is the fracture behaviour of the irradiated materials, and how this correlates with amount of damage induced in the materials. This is further emphasises by the studies in

the ion implantations at 750°C and the hot nanoindentation study, that showed some forms of annealing out of the defects where surface fracture then became evident again. This is an incredibly important result for looking at how these materials may perform in an in-service machine undergoing continuous radiation damage.

The combination of the monolithic and fabricated composite work give valuable insight into truly understanding the differences between how each behaves under irradiation conditions.

The high temperature nanoindetation performed in this project is a vital step forward in the field for understanding the mechanical behaviour of SiC at in-service temperatures, and how the effects of radiation damage are completely different to those seen at room temperature especially with respect to the irradiated material showing larger elastic moduli than the unirradiated material.

7.2 Conclusions

There were two principle aims to this project, to investigate micromechanical properties of silicon carbide under irradiation conditions, and to enable direct comparisons of different irradiation conditions and materials with those investigations. With the combination of multiple silicon and a neon implantation along with nanoindentaion studies this has been the central theme of the whole work. The analysis of commercially produced SiC against the fabricated TEP materials was able to give an extra dimension to the project and was able to highlight further areas for future investigations.

While the various materials studied in this work behaved in very similar manners under nanoindentation in their virgin state, slightly different degrees of radiation damage were seen across the different materials under the various irradiation conditions. While the commercial grade materials behaved in conclusive manners according to the radiation damage, the inhomogeneity of the TEP samples made conclusions about the effects of radiation damage on hardness and elastic modulus more difficult. Despite this the fracture behaviour of all samples showed consistent damage mechanisms to be suppressing surface fracture. The addition of the hot nanoindentation study was able to further analyse nanoindentation properties and fracture behaviour to an in-service temperature range.

It was clear that the fabrication technique used for the TEP materials was not optimal, with

inhomogenaity seen both at the macroscopic and microscopic scales, however there were distinctive irradiation behaviours seen. With improvements to statistical analysis of nanoindentation more quantitative conclusions could be drawn.

While the literature and additional microstructural studies performed with this work were able to give some insight into the mechanisms behind the hardening and reduction in elastic modulus in the room temperature studies, with small scale defects seen in the low dose low temperature irradiation material more work is needed to better understand the mechanisms at play.

7.3 Future Work

With the development of silicon carbide for fusion increasing, and nearing use in some fission reactors, its potential for use is vastly improving. Despite this there are a lot of basic scientific questions still needing answering. While this project has looked into some specific areas, it has also showed places where future investigation is needed.

As previously discussed at times there were quantitative investigations in this work were not able to be performed and only qualitative results were given as explanations for effects seen in micromechanical results. The author believes these are some of the principle places where future work could produce interesting science.

While the literature on defect dynamics and the microstructure of silicon carbide was used draw some conclusions as to the origins of the mechanical changes seen in this work, these were insufficient to pin down the mechanisms at play. Expanding the current work to look in detail at the damage caused in the materials studied here would bring together these disparate works.

There was clearly a problem with statistical variance across the nanoindentation studies performed at room temperature across the different forms of silicon carbide. This caused problems with being able to draw accurate conclusions of the effects of different radiation conditions. Hausild et al 2019 [244] have recently published work on statistical analysis of nanoindentations, including looking at interface and length scale problems. Using more advanced statistical techniques on nanoindentation studies, especially on inhomogeneous samples like the ones fabricated using TEP would help to produce more statistically and scientifically sound results in these types of works. The way that data is produced by the software itself seems to be at fault

here, and investigations into how more 'raw' data could be obtained would be a first step in allowing for comparisons of data sets allowing for better significance to be evaluated.

The hot nanoindentation study performed as part of this work managed to show interesting effects of irradiation damage on at temperature mechanical properties. This technique was very time consuming, and is still an developing analysis technique, and further studies to higher temperatures and across the range of materials studied here would create a much broader understanding of the field.

With large investments into fusion facilities like the Materials Research Facility at Culham Centre for Fusion Energy, and the progression of facilities like International Fusion Materials Irradiation Facility (IFMIF), a wide range of technologically advanced analysis methods are becoming more available in fusion studies. With so many different areas of fusion and silicon carbide research still needing investigating, and understanding, these technological advances will help with the increasing requirement for fusion relevant studies.

Bibliography

[1] International Energy Agency I. World Energy Outlook 2018; 2018.

[2] UN. Climate Change; 2015. Available from: http://www.un.org/en/globalissues/climatechange/.

[3] Rogelj J, Shindell D, Fifita S, Forster P, Ginzburg V, Handa C, et al. Mitigation Pathways Compatible with 1.5C in the Context of Sustainable Development. In: Masson-Delmotte, Zhai VP, Pörtner HO, Roberts D, Skea J, Shukla PR, et al., editors. Global Warming of 1.5C. An IPCC Special Report on the impacts of global warming of 1.5C above pre-industrial levels and related global greenhouse gas emission pathways, in the context of strengthening the global response to the threat of climate change,. IPCC; 2018. .

[4] British Petroleum. BP Statistical Review of World Energy June 2015; 2015. June. Available from: http://scholar.google.com/scholar?hl=en{&}btnG=Search{&}q=intitle:BP+Statistical+Review+of+World+Energy{#}0.

[5] British Petroleum. BP Energy Outlook 2019 edition; 2019.

[6] Bryce R. The Real Problem With Renewables; 2010. Available from: http://www.forbes.com/2010/05/11/renewables-energy-oil-economy-opinions-contributors-robert-bryce.html.

[7] de Coninck H, Revi A, Babiker M, Bertoldi P, Buckeridge M, Cartwright A, et al. Strengthening and Implementing the Global Response. In: Masson-Delmotte, Zhai VP, Pörtner HO, Roberts D, Skea J, Shukla PR, et al., editors. Global Warming of 1.5C. An IPCC Special Report on the impacts of global warming of 1.5C above pre-industrial levels and related global greenhouse gas emission pathways, in the context of strengthening the global response to the threat of climate change,. IPCC; 2018. .

[8] World Nuclear Association. Fukushima Accident; 2015. Available from: http://www.world-nuclear.org/info/safety-and-security/safety-of-plants/fukushima-accident/.

[9] EDF Energy. Answering the big questions about new nuclear power stations; 2015. Available from: http://www.edfenergy.com/energyfuture/edf-energys-approach-why-we-choose-new-nuclear/implications-for-new-nuclear.

[10] Koyanagi T, Katoh Y, Nozawa T, Snead LL, Kondo S, Henager Jr CH, et al. Recent progress in the development of SIC composites for nuclear fusion applications. Journal of Nuclear Materials. 2018;511:544–555. Available from: https://doi.org/10.1016/j.jnucmat.2018.06.017.

[11] Sawan ME, Katoh Y, Snead LL. Transmutation of silicon carbide in fusion nuclear environment. Journal of Nuclear Materials. 2013;442(1):S370–S375. Available from: http://www.sciencedirect.com/science/article/pii/S0022311512006046.

[12] Tobita K, Utoh H, Liu C, Tanigawa H, Tsuru D, Enoeda M, et al. Search for reality of solid breeder blanket for DEMO. Fusion Engineering and Design. 2010 dec;85(7-9):1342–1347. Available from: http://linkinghub.elsevier.com/retrieve/pii/S0920379610001092.

[13] Gilbert MR, Sublet JC. Scoping of material response under DEMO neutron irradiation : Comparison with fission and influence of nuclear library selection. Fusion Engineering and Design. 2017;125:299–306. Available from: https://doi.org/10.1016/j.fusengdes.2017.06.016.

[14] Kohyama A, Katoh Y, Ando M, Jimbo K. A new Multiple BeamsMaterial Interaction Research Facility for radiation damage studies in fusion materials. Fusion Engineering and Design. 2000 nov;51-52:789–795. Available from: http://linkinghub.elsevier.com/retrieve/pii/S0920379600001812.

[15] Kishimoto H, Ozawa K, Kondo S, Kohyama A. Effects of Dual-Ion Irradiation on the Swelling of SiC/SiC Composites. Materials Transactions. 2005;46(8):1923–1927. Available from: https://www.jstage.jst.go.jp/article/matertrans/46/8/46{_}8{_}1923/{_}article.

[16] Katoh Y, Hashimoto N, Kondo S, Snead LL, Kohyama A. Microstructural development in cubic silicon carbide during irradiation at elevated temperatures. Journal of Nuclear Materials. 2006 jun;351(1-3):228–240. Available from: http://www.sciencedirect.com/science/article/pii/S0022311506000869http://linkinghub.elsevier.com/retrieve/pii/S0022311506000869.

[17] Shen Z, Hu D, Yang G, Han X. Ballistic reliability study on SiC/UHMWPE composite armor against armor-piercing bullet. Composite Structures. 2019 apr;213:209–219. Available from: https://linkinghub.elsevier.com/retrieve/pii/S0263822318344039.

[18] Kienzle A, Jäger H. Carbon-Fiber-Reinforced Silicon Carbide: a New Brake Disk Material. In: Crolla D, Foster DE, Kobayashi T, Vaughan N, editors. Encyclopedia of Automotive Engineering; 2014. p. 1–12.

[19] Huseynov E, Jazbec A, Snoj L. Temperature vs . impedance dependencies of neutron-irradiated nanocrystalline silicon carbide (3C-SiC). Applied Physics A. 2019;125(9). Available from: http://dx.doi.org/10.1007/s00339-018-2294-x.

[20] Davis RF. Silicon Carbide. Reference Module in Materials Science and Materials Engineering. 2017 jan;Available from: https://www.sciencedirect.com/science/article/pii/B9780128035818024450.

[21] Zok FW. Ceramic-matrix composites enable revolutionary gains in turbine engine efficiency. American Ceramics Society Bulletin. 2016;95(5).

[22] ESA. Space in Images - 2017 - 05 - Silicon carbide mirror subjected to thermalvacuum testing; 2017. Available from: http://www.esa.int/spaceinimages/Images/2017/05/Silicon{_}carbide{_}mirror{_}subjected{_}to{_}thermal{_}vacuum{_}testing.

[23] Katoh Y, Snead LL, Henager CH, Nozawa T, Hinoki T, Iveković A, et al. Current status and recent research achievements in SiC/SiC composites. Journal of Nuclear Materials. 2014 dec;455(1-3):387–397. Available from: http://www.sciencedirect.com/science/article/pii/S0022311514003602.

[24] Iveković A, Novak S, Dražić G, Blagoeva D, de Vicente SG. Current status and prospects of SiCf/SiC for fusion structural applications. Journal of the European Ceramic Society. 2013 sep;33(10):1577–1589. Available from: http://www.sciencedirect.com/science/article/pii/S0955221913001052http://linkinghub.elsevier.com/retrieve/pii/S0955221913001052.

[25] Cheng ET. Assessment of low activation materials. The 14th IEEE/NPSS Symposium Fusion Engineering. 1992;p. 621–625. Available from: http://ieeexplore.ieee.org/lpdocs/epic03/wrapper.htm?arnumber=218844.

[26] Katoh Y, Snead LL, Cheng T, Shih C, Lewis WD, Koyanagi T, et al. Radiation-tolerant joining technologies for silicon carbide ceramics and composites. Journal of Nuclear Materials. 2014 may;448(1-3):497–511. Available from: http://www.sciencedirect.com/science/article/pii/S0022311513011410.

[27] El-Guebaly L, Jaber A, Mynsberge L, ARIES-ACT Team. State-of-the-Art 3-D Assessment of Elements Degrading the TBR of the Aries-Act SiC/LiPb Blanket; 2012.

[28] Jones RH, Giancarli L, Hasegawa A, Katoh Y, Kohyama A, Riccardi B, et al. Promise and challenges of SiC f / SiC composites for fusion energy applications. Journal of Nuclear Materials. 2002;311:1057–1072.

[29] Snead LL, Nozawa T, Katoh Y, Byun TS, Kondo S, Petti DA. Handbook of SiC properties for fuel performance modeling. Journal of Nuclear Materials. 2007;371(1):329–377. Available from: http://www.sciencedirect.com/science/article/pii/S0022311507007623.

[30] Abe T, Kishimoto H, Nakazato N, Park JS, Jung HC, Kohno Y, et al. SiC/SiC composite heater for IFMIF. Fusion Engineering and Design. 2012;87(7-8):1258–1260. Available from: http://linkinghub.elsevier.com/retrieve/pii/S0920379612001986.

[31] Konishi S, Enoeda M, Nakamichi M, Hoshino T, Ying A, Sharafat S, et al. Functional materials for breeding blankets status and developments. Nuclear Fusion. 2017;57(092014).

[32] Snead LL, Nozawa T, Ferraris M, Katoh Y, Shinavski R, Sawan M. Silicon carbide composites as fusion power reactor structural materials. Journal of Nuclear Materials. 2011;417(1):330–339. Available from: http://www.sciencedirect.com/science/article/pii/S0022311511002637.

[33] Hosemann P, Martos JN, Frazer D, Vasudevamurthy G, Byun TS, Hunn JD, et al. Mechanical characteristics of SiC coating layer in TRISO fuel particles. Journal of Nuclear Materials. 2013;442(1-3):133–142. Available from: http://dx.doi.org/10.1016/j.jnucmat.2013.08.041.

[34] Hinoki T, Katoh Y, Snead LL, Jung HC, Ozawa K, Katsui H, et al. Silicon Carbide and Silicon Carbide Composites for Fusion Reactor Application. Materials Transactions. 2013;54(4):472–476. Available from: https://www.jstage.jst.go.jp/article/matertrans/54/4/54{_}MG201206/{_}article.

[35] Deck CP, Jacobsen GM, Sheeder J, Gutierrez O, Zhang J, Stone J, et al. Characterization of SiC-SiC composites for accident tolerant fuel cladding. Journal of Nuclear Materials. 2015;466:667–681. Available from: http://dx.doi.org/10.1016/j.jnucmat.2015.08.020.

[36] Sharma AS, Fitriani P, Yoon DH. Fabrication of SiC f / SiC and integrated assemblies for nuclear reactor applications. Ceramics International. 2017;43(18):17211–17215. Available from: http://dx.doi.org/10.1016/j.ceramint.2017.09.126.

[37] Moissan H. Nouvelles recherches sur la météorité de Cañon Diablo. Comptes rendus hebdomadaires des séances de l'Académie des sciences. 1904;139:778–786.

[38] Constance Parche M. Silicon Carbide. In: Kirk-Othmer encyclopedia of chemical technology Volume 4. 2nd ed. John Wiley & Sons NY; 1964. p. 114–132.

[39] Jepps NW, Page TF. Polytypic transformations in silicon carbide. Progress in Crystal Growth and Characterization. 1983;7(December):259–307.

[40] Yao T, Yin D, Saito M, Wu B, Chen C, Ma X. Nanoindentation-induced phase transformation between SiC polymorphs. Materials Letters. 2018;220:152–155.

[41] Sawyer GR, Page TF. Microstructural characterization of REFEL (reaction-bonded) silicon carbides. Journal of Materials Science. 1978 apr;13(4):885–904. Available from: http://link.springer.com/10.1007/BF00570528.

[42] Shimoda K, Eiza N, Park JS, Hinoki T, Kohyama A, Kondo S. High-Temperature Mechanical Property Improvements of SiC Ceramics by NITE Process. Materials Transactions. 2006;47(4):1204–1208. Available from: https://www.jstage.jst.go.jp/article/matertrans/47/4/47{_}4{_}1204/{_}article.

[43] Munro RG. Material properties of a sintered α-SiC. Journal of Physical and Chemical Reference Data. 1997;26(5):1195–1203.

[44] Edington JW, Rowcliffe DJ, Henshall JL. The Mechanical Properties of Silicon Nitride and Silicon Carbide Part I: Materials and Strength. Powder Metallurgh International Journal. 1975;7(2):82–96.

[45] Orange G, Tanaka H, Fantozzi G. Fracture toughness of pressureless sintered silicon carbide: A comparison of Klc measurement methods. Ceramics International. 1987 jan;13(3):159–165. Available from: http://www.sciencedirect.com/science/article/pii/0272884287900265.

[46] Henshall JL, Rowcliffe DJ, Edington JW. Fracture Toughness of Single-Crystal Silicon Carbide. Journal of the American Ceramic Society. 1977 jul;60(7-8):373–375. Available from: http://doi.wiley.com/10.1111/j.1151-2916.1977.tb15564.x.

[47] Henshall JL, Brookes CA. The measurement of K IC in single crystal SiC using the indentation method. Journal of Materials Science Letters. 1985 jun;4(6):783–786. Available from: http://link.springer.com/10.1007/BF00726990.

[48] Qian J, Daemen LL, Zhao Y. Hardness and fracture toughness of moissanite. Diamond and Related Materials. 2005;14:1669–1672.

[49] Zhang H, López-Honorato E, Javed A, Shapiro I, Xiao P. A Study of the Microstructure and Vickers Indentation Fracture Toughness of Silicon Carbide Coatings on TRISO Fuel Particles. Journal of the American Ceramic Society. 2012 jan;95(3):1086–1092. Available from: http://doi.wiley.com/10.1111/j.1551-2916.2011.05044.x.

[50] Nogami S, Hasegawa a, Snead LL. Indentation fracture toughness of neutron irradiated silicon carbide. Journal of Nuclear Materials. 2002 dec;307-311:1163–1167. Available from: http://linkinghub.elsevier.com/retrieve/pii/S0022311502010553.

[51] Anstis GR, Chantikul P, Lawn BR, Marshall DB. A critical evaluation of indentation techniques for measuring fracture toughness: I Direct crack measurements. Journal of the American Ceramic Society. 1981;46(September):533–538. Available from: http://onlinelibrary.wiley.com/doi/10.1111/j.1151-2916.1981.tb10320.

x/abstract;jsessionid=8DD229270528CF8F6698F4F500593C2E.f03t04http://onlinelibrary.wiley.com/doi/10.1111/j.1151-2916.1981.tb10320.x/abstract.

[52] Lawn BR. Fracture and deformation in brittle solids : A perspective on the issue of scale. Journal of Materials Research. 2004;19(1):22–29.

[53] Kitahara H, Noda Y, Yoshida F, Nakashima H, Shinohara N, Abe H. Mechanical Behavior of Single Crystalline and Polycrystalline Silicon Carbides Evaluated by Vickers Indentation. Journal of the Ceramic Society of Japan. 2001;109(7):602–606.

[54] Newsome G, Snead LL, Hinoki T, Katoh Y, Peters D. Evaluation of neutron irradiated silicon carbide and silicon carbide composites. Journal of Nuclear Materials. 2007;371(1):76–89. Available from: http://www.sciencedirect.com/science/article/pii/S0022311507007428.

[55] Snead LL, Jones RH, Kohyama A, Fenici P. Status of silicon carbide composites for fusion. Journal of Nuclear Materials. 1996 oct;233-237:26–36. Available from: http://www.sciencedirect.com/science/article/pii/S0022311596003182.

[56] Ghoniem NM. High-temperature mechanical and material design for SiC composites. Journal of Nuclear Materials. 1992;191-194:515–519.

[57] Katoh Y, Ozawa K, Shih C, Nozawa T, Shinavski RJ, Hasegawa A, et al. Continuous SiC fiber, CVI SiC matrix composites for nuclear applications: Properties and irradiation effects. Journal of Nuclear Materials. 2014 may;448(1-3):448–476. Available from: http://www.sciencedirect.com/science/article/pii/S0022311513008647.

[58] Snead LL, Schwarz OJ. Advanced SiC composites for fusion applications. Journal of nuclear materials. 1995;219:3–14. Available from: http://www.sciencedirect.com/science/article/pii/0022311594006636.

[59] Ho CY, Tsai SC, Lin HT, Chen FR, Kai JJ. Microstructural investigation of Si-ion-irradiated single crystal 3C-SiC and SA-Tyrannohex SiC fiber-bonded composite at high temperatures. Journal of Nuclear Materials. 2013;443(1):1–7. Available from: http://www.sciencedirect.com/science/article/pii/S0022311513008696.

[60] Novak S, Dražić G, König K, Iveković A. Preparation of SiCf/SiC composites by the slip infiltration and transient eutectoid (SITE) process. Journal of Nuclear Materials. 2010;399(2-3):167–174. Available from: http://linkinghub.elsevier.com/retrieve/pii/S0022311510000152.

[61] Frazer D, Abad MD, Krumwiede D, Back CA, Khalifa HE, Deck CP, et al. Localized mechanical property assessment of SiC/SiC composite materials. Composites Part A: Applied Science and Manufacturing. 2015;70:93–101. Available from: http://linkinghub.elsevier.com/retrieve/pii/S1359835X14003479.

[62] Deck CP, Jacobsen GM, Sheeder J, Gutierrez O, Zhang J, Stone J, et al. Characterization of SiCSiC composites for accident tolerant fuel cladding. Journal of Nuclear Materials. 2015;466:667–681. Available from: http://linkinghub.elsevier.com/retrieve/pii/S0022311515301598.

[63] Khalifa HE, Koyanagi T, Jacobsen GM, Deck CP, Back CA. Radiation stable, hybrid, chemical vapor infiltration/preceramic polymer joining of silicon carbide components. Journal of Nuclear Materials. 2017;487:91–95. Available from: http://www.sciencedirect.com/science/article/pii/S0022311516305785.

[64] Koyanagi T, Katoh Y, Kiggans JO, Hinoki T, Khalifa HE, Deck CP, et al. Irradiation resistance of silicon carbide joint at light water reactor-relevant temperature. Journal of Nuclear Materials. 2017;488:150–159. Available from: http://dx.doi.org/10.1016/j.jnucmat.2017.03.017.

[65] Price RJ. Effects of fast-neutron irradiation on pyrolytic silicon carbide. Journal of Nuclear Materials. 1969 oct;33(1):17–22. Available from: http://www.sciencedirect.com/science/article/pii/0022311569900038.

[66] Centronic Ltd. Fission Chambers; 2005. Available from: www.centronic.co.uk.

[67] O'Connell JH, Neethling JH. Investigation of radiation damage and hardness of H- and He-implanted SiC. Radiation Effects and Defects in Solids. 2012 may;167(5):299–306. Available from: http://ezproxy-prd.bodleian.ox.ac.uk:2108/doi/abs/10.1080/10420150.2012.678008{#}.VRsskY54p3Q.

[68] Shen Q, Zhou W, Ran G, Li R, Feng Q, Li N. Evolution of Helium Bubbles and Discs in Irradiated 6H-SiC during Post-Implantation Annealing. Materials. 2017;10(101).

[69] Han W, Li B. Microstructural defects in He-irradiated polycrystalline alpha-SiC at 1000C. Journal of Nuclear Materials. 2018;504:161–165.

[70] Sasase M, Ito Y, Yasuda K, Ishigami R, Hatori S, Yamamoto A. Defect formation in 6H-SiC irradiated by 3 MeV He ions. Nuclear Instruments and Methods in Physics Research Section B: Beam Interactions with Materials and Atoms. 2003 aug;209:179–183. Available from: http://www.sciencedirect.com/science/article/pii/S0168583X02020232.

[71] Leclerc S, Beaufort MF, Declémy A, Barbot JF. Damage induced in high energy helium-implanted 4H-SiC. Nuclear Instruments and Methods in Physics Research Section B: Beam Interactions with Materials and Atoms. 2006 jan;242(1-2):399–401. Available from: http://www.sciencedirect.com/science/article/pii/S0168583X05015582http://linkinghub.elsevier.com/retrieve/pii/S0168583X05015582.

[72] Harrison RW, Ebert S, Hinks JA, Donnelly SE. Damage microstructure evolution of helium ion irradiated SiC under fusion relevant temperatures. Journal of the European Ceramic Society. 2018;38(11):3718–3726. Available from: https://doi.org/10.1016/j.jeurceramsoc.2018.04.060.

[73] Snead LL, Hay JC. Neutron irradiation induced amorphization of silicon carbide. Journal of Nuclear Materials. 1999 jul;273(2):213–220. Available from: http://linkinghub.elsevier.com/retrieve/pii/S0022311599000239.

[74] Snead LL, Katoh Y, Connery S. Swelling of SiC at intermediate and high irradiation temperatures. Journal of Nuclear Materials. 2007 aug;367-370:677–684. Available from: http://www.sciencedirect.com/science/article/pii/S0022311507004515.

[75] Pramono Y, Sasaki K, Yano T. Release and Diffusion Rate of Helium in Neutron-Irradiated SiC. Journal of Nuclear Science and Technology. 2004;41(7):751–755. Available from: http://www.tandfonline.com/doi/abs/10.1080/18811248.2004.9715542.

[76] Prasad KE, Ramesh KT. Hardness and mechanical anisotropy of hexagonal SiC single crystal polytypes. Journal of Alloys and Compounds. 2019;770:158–165. Available from: https://doi.org/10.1016/j.jallcom.2018.08.102.

[77] Barbot JF, Beaufort MF, Texier M, Tromas C. Swelling and stacking fault formation in helium implanted SiC. Journal of Nuclear Materials. 2011;413(3):162–165. Available from: http://www.sciencedirect.com/science/article/pii/S0022311511003813.

[78] Li JJ, Zhang CH, Xu CL, Jia XJ, Song Y, Li JY, et al. Lattice damage and nanohardness in 6HSiC implanted with multiple-energy Xe ions. Nuclear Instruments and Methods in Physics Research Section B: Beam Interactions with Materials and Atoms. 2012 sep;286:124–128. Available from: http://www.sciencedirect.com/science/article/pii/S0168583X11010652.

[79] Yang Y, Zhang C, Su C, Ding Z, Song Y. Dose dependence of nano-hardness of 6H-SiC crystal under irradiation with inert gas ions. Nuclear Inst and Methods in Physics Research, B. 2018;422(509):50–53. Available from: https://doi.org/10.1016/j.nimb.2018.02.035.

[80] Chen X, Zhou W, Zhang X, Feng Q, Zheng J, Liu X, et al. Mechanical properties of 6H-SiC irradiated by neutron and MeV heavy ions : A nanoindentation and finite element method study. Journal of Applied Physics. 2018;123(025104).

[81] Wang X, Zhang Y, Liu S, Wang C, Zhao Z. Optical and structural properties of 6HSiC irradiated by coimplantation. Nuclear Instruments and Methods in Physics Research Section B: Beam Interactions with Materials and Atoms. 2012 oct;289:47–51. Available from: http://www.sciencedirect.com/science/article/pii/S0168583X12004922.

[82] Wang X, Zhang Y, Han D, Zhao Y, Zhao Z. Damage production in silicon carbide by dual ion beams irradiation. Journal of Nuclear Materials. 2018;499:326–333. Available from: https://doi.org/10.1016/j.jnucmat.2017.11.020.

[83] Wang X, Zhao Z, Zhang M, Zhao Y, Han D, Chu J, et al. Damage effects of Au & He dual ion irradiated silicon carbide. Materials Research Express. 2018;5(105902).

[84] Osborne MC, Hay JC, Snead LL, Steiner D. Mechanical- and Physical-Property Changes of Neutron-Irradiated Chemical-Vapor-Deposited Silicon Carbide. Journal of the American Ceramic Society. 1999 sep;82(9):2490–2496. Available from: http://doi.wiley.com/10.1111/j.1151-2916.1999.tb02108.x.

[85] Kondo S, Katoh Y, Snead LL. Microstructural defects in SiC neutron irradiated at very high temperatures. Journal of Nuclear Materials. 2008 dec;382(2-3):160–169. Available from: http://www.sciencedirect.com/science/article/pii/S0022311508004583.

[86] Yu K, Ru Y, Jun P, Jung J, Hu A. Microscopic origin of black spot defect swelling in single crystal 3C- SiC. Journal of Nuclear Materials. 2018;508:292–298. Available from: https://doi.org/10.1016/j.jnucmat.2018.05.054.

[87] Lin YR, Chen LG, Hsieh CY, Chang MT, Fung KY, Hu A, et al. Atomic Configuration of Point Defect Clusters in Ion-Irradiated Silicon Carbide. Scientific Reports. 2017;7(1):1–6.

[88] Sprouster DJ, Koyanagi T, Dooryhee E, Ghose SK, Katoh Y, Ecker LE. Microstructural evolution of neutron irradiated 3C-SiC. Scripta Materialia. 2017 aug;137:132–136. Available from: http://dx.doi.org/10.1016/j.scriptamat.2017.02.030http://linkinghub.elsevier.com/retrieve/pii/S1359646217300969.

[89] Hu X, Koyanagi T, Zhao J, Yamamoto T, Katoh Y. Microstructural evolution of 3C-SiC exposed to simultaneous neutron irradiation and helium implantation. Journal of Nuclear Materials. 2018;509:366–376. Available from: https://doi.org/10.1016/j.jnucmat.2018.07.007.

[90] Kondo S, Katoh Y, Snead LL. Analysis of grain boundary sinks and interstitial diffusion in neutron-irradiated SiC. Physical Review B. 2011 feb;83(7):075202. Available from: http://link.aps.org/doi/10.1103/PhysRevB.83.075202.

[91] Sprouster DJ, Koyanagi T, Dooryhee E, Ghose SK, Katoh Y, Ecker LE. Reprint of : Microstructural evolution of neutron irradiated 3C-SiC. Scripta Materialia. 2018;143:176–180. Available from: https://doi.org/10.1016/j.scriptamat.2017.09.034.

[92] Katoh Y, Kishimoto H, Kohyama A. The influences of irradiation temperature and helium production on the dimensional stability of silicon carbide. Journal of Nuclear Materials. 2002 dec;307-311:1221–1226. Available from: http://www.sciencedirect.com/science/article/pii/S0022311502010620.

[93] Kondo S, Hinoki T, Kohyama A. Synergistic Effects of Heavy Ion and Helium Irradiation on Microstructural and Dimensional Change in β-SiC. Materials Transactions. 2005;46(6):1388–1392. Available from: https://www.jstage.jst.go.jp/article/matertrans/46/6/46{_}6{_}1388/{_}article.

[94] Lin YR, Ku CS, Ho CY, Chuang WT, Kondo S, Kai JJ. Irradiation-induced microstructural evolution and swelling of 3C-SiC. Journal of Nuclear Materials. 2015;459:276–283. Available from: http://linkinghub.elsevier.com/retrieve/pii/S0022311515000537.

[95] Park KH, Kishimoto H, Kohyama A. 3D analysis of cracking behaviour under indentation in ion-irradiated -SiC. Journal of Electron Microscopy. 2004 oct;53(5):511–513. Available from: http://jmicro.oupjournals.org/cgi/doi/10.1093/jmicro/dfh079.

[96] Chen CH, Zhang Y, Fu E, Wang Y, Crespillo ML, Liu C, et al. Irradiation-induced microstructural change in helium-implanted single crystal and nano-engineered SiC. Journal of Nuclear Materials. 2014 oct;453(1-3):280–286. Available from: http://www.sciencedirect.com/science/article/pii/S0022311514004590.

[97] Sun D, Li R, Ding J, Zhang P, Wang Y, Zhao J. Interaction between helium and intrinsic point defects in 3C-SiC single crystal. Journal of Applied Physics. 2017;121(225111).

[98] Sun J, You Yw, Hou J, Li X, Li BS, Liu CS. The effect of irradiation-induced point defects on energetics and kinetics of hydrogen in 3C-SiC in a fusion environment. Nuclear Fusion. 2017;57(066031).

[99] Park KH, Katoh Y, Kishimoto H, Kohyama a. Evaluation of dual-ion irradiated β-SiC by means of indentation methods. Journal of Nuclear Materials. 2002 dec;307-311(2 SUPPL.):1187–1190. Available from: http://www.sciencedirect.com/science/article/pii/S0022311502009558.

[100] Matthews RB. Irradiation damage in reaction-bonded silicon carbide. Journal of Nuclear Materials. 1974 jun;51(2):203–208. Available from: http://www.sciencedirect.com/science/article/pii/0022311574900038.

[101] Nogami S, Hasegawa A. Indentation Properties of Silicon Carbide after Neutron Irradiation and Helium Implantation. IOP Conference Series: Materials Science and Engineering. 2011 oct;18(16):162007. Available from: http://iopscience.iop.org/1757-899X/18/16/162007.

[102] Katoh Y, Koyanagi T, Mcduffee JL, Snead LL, Yueh K. Dimensional stability and anisotropy of SiC and SiC-based composites in transition swelling regime. Journal of Nuclear Materials. 2018;499:471–479. Available from: https://doi.org/10.1016/j.jnucmat.2017.12.009.

[103] Koyanagi T, Ozawa K, Hinoki T, Shimoda K, Katoh Y. Effects of neutron irradiation on mechanical properties of silicon carbide composites fabricated by nano-infiltration and transient eutectic-phase process. Journal of Nuclear Materials. 2014 may;448(1-3):478–486. Available from: http://www.sciencedirect.com/science/article/pii/S0022311513011446.

[104] Terrani KA, Ang C, Snead LL, Katoh Y. Irradiation stability and thermo-mechanical properties of NITE-SiC irradiated to 10 dpa. Journal of Nuclear Materials. 2018;499:242–247. Available from: https://doi.org/10.1016/j.jnucmat.2017.11.040.

[105] Gosset D, Audren A, Leconte Y, Thome L, Monnet I, Herlin-Boime N. Structural irradiation damage and recovery in nanometric silicon carbide. Progress in Nuclear Energy. 2012 may;57:52–56. Available from: http://www.sciencedirect.com/science/article/pii/S0149197011002691.

[106] Page TF, Sawyer GR. Discusssion of 'Microstructural characterization of 'REFEL' (reaction-bonded) silicon carbides': Authors' reply. Journal of Materials Science. 1980 jul;15(7):1850–1856. Available from: http://link.springer.com/10.1007/BF00550606.

[107] Parish CM, Koyanagi T, Kondo S, Katoh Y. Irradiation-induced β to α SiC transformation at low temperature. Scientific Reports. 2017;(December 2016):1–9. Available from: http://dx.doi.org/10.1038/s41598-017-01395-y.

[108] Gao F, Weber WJ, Devanathan R. Defect production, multiple ion-solid interactions and amorphization in SiC. Nuclear Instruments and Methods in Physics Research, Section B: Beam Interactions with Materials and Atoms. 2002;191(1-4):487–496.

[109] Gao F, Weber W. Cascade overlap and amorphization in 3C-SiC: Defect accumulation, topological features, and disordering. Physical Review B. 2002;66(2):1–10.

[110] Gao F, Weber WJ, Devanathan R. Atomic-scale simulation of displacement cascades and amorphization in beta-SiC. Nuclear Instruments and Methods in Physics Research, Section B: Beam Interactions with Materials and Atoms. 2001;180(1-4):176–186.

[111] Gao F, Weber W. Atomic-scale simulation of 50 keV Si displacement cascades in β-SiC. Physical Review B. 2000;63(5):054101. Available from: http://link.aps.org/doi/10.1103/PhysRevB.63.054101.

[112] Snead LL, Steiner D, Zinkle SJ. Measurement of the effect of radiation damage to ceramic composite interfacial strength. Journal of Nuclear Materials. 1992;191-194:566–570. Available from: http://linkinghub.elsevier.com/retrieve/pii/S0022311509801098.

[113] Snead LL, Zinkle SJ, Steiner D. Radiation induced microstructure and mechanical property evolution of SiC/C/SiC composite materials. Journal of Nuclear Materials. 1992 sep;191-194:560–565. Available from: http://linkinghub.elsevier.com/retrieve/pii/S0022311509801086.

[114] Katoh Y, Ozawa K, Hinoki T, Choi Y, Snead LL, Hasegawa A. Mechanical properties of advanced SiC fiber composites irradiated at very high temperatures. Journal of Nuclear Materials. 2011 oct;417(1-3):416–420. Available from: http://www.sciencedirect.com/science/article/pii/S0022311511001917.

[115] Ozawa K, Katoh Y, Nozawa T, Snead LL. Effect of neutron irradiation on fracture resistance of advanced SiC/SiC composites. Journal of Nuclear Materials. 2011;417(1):411–415. Available from: http://www.sciencedirect.com/science/article/pii/S0022311510009074.

[116] Ozawa K, Katoh Y, Nozawa T, Hinoki T, Snead LL. Evaluation of Damage Tolerance of Advanced SiC/SiC Composites after Neutron Irradiation. IOP Conference Series: Materials Science and Engineering. 2011 oct;18(16):162005. Available from: http://stacks.iop.org/1757-899X/18/i=16/a=162005?key=crossref.646fce5a16c45a9f03fb68c243a29a63.

[117] Perez-Bergquist AG, Nozawa T, Shih C, Leonard KJ, Snead LL, Katoh Y. High dose neutron irradiation of Hi-Nicalon Type S silicon carbide composites, Part 1: Microstructural evaluations. Journal of Nuclear Materials. 2015 jul;462:443–449. Available from: http://www.sciencedirect.com/science/article/pii/S002231151400395X.

[118] Ozawa K, Hinoki T, Nozawa T, Katoh Y, Maki Y, Kondo S, et al. Evaluation of Fiber/Matrix Interfacial Strength of Neutron Irradiated SiC/SiC Composites Using Hysteresis Loop Analysis of Tensile Test. Materials Transactions. 2006;47(1):207–210. Available from: http://joi.jlc.jst.go.jp/JST.JSTAGE/matertrans/47.207?from=CrossRef.

[119] Koyanagi T, Katoh Y. Mechanical properties of SiC composites neutron irradiated under light water reactor relevant temperature and dose conditions. Journal of Nuclear Materials. 2017;494:46–54. Available from: http://dx.doi.org/10.1016/j.jnucmat.2017.07.007.

[120] Koyanagi T, Nozawa T, Katoh Y, Snead LL. Mechanical property degradation of high crystalline SiC fi ber reinforced SiC matrix composite neutron irradiated to 100 displacements per atom. Journal of the European Ceramic Society. 2018;38(4):1087–1094. Available from: https://doi.org/10.1016/j.jeurceramsoc.2017.12.026.

[121] Idris MI, Yamazaki S, Yoshida K, Yano T. Recovery behavior of SiC f / SiC composites by post-irradiation annealing up to of 1673 K. Energy Procedia. 2017;131:413–419. Available from: https://doi.org/10.1016/j.egypro.2017.09.461.

[122] Nogami S, Hasegawa A, Taguchi T, Abe K, Yamada R. Surface Morphology Changes in a SiC/SiC Composite as Caused by Simultaneous Triple-Ion-Beam Irradiation.; 2001.

[123] Miwa S, Hasegawa A, Taguchi T, Igawa N, Abe K. Cavity Formation in a SiC/SiC Composite under Simultaneous Irradiation of Hydrogen, Helium and Silicon Ions. Materials Transactions. 2005;46(3):536–542. Available from: http://joi.jlc.jst.go.jp/JST.JSTAGE/matertrans/46.536?from=CrossRef.

[124] Duh TS, Yin KM, Yan JY, Fang PC, Chen CW, Kai JJ, et al. Study of helium bubble formation in SiCf/PyC/β-SiC composites by dual-beam irradiation. Journal of Nuclear Materials. 2004 aug;329-333:518–523. Available from: http://www.sciencedirect.com/science/article/pii/S0022311504002508.

[125] Huguet-Garcia J, Jankowiak A, Miro S, Vandenberghe T, Grygiel C, Monnet I, et al. In situ characterization of ion-irradiation enhanced creep of third generation Tyranno SA3 SiC fibers. Journal of Materials Research. 2015 feb;30(09):1–11. Available from: http://journals.cambridge.org/abstract{_}S0884291414004129.

[126] Chai Y, Zhang H, Zhou X, Zhang Y. Effects of silicon ion irradiation on the interface properties of SiC f / SiC composites. Ceramics International. 2018;44:2165–2169.

[127] Fitriani P, Sharma AS, Yoon DH. Effects of sintering additives on the microstructural and mechanical properties of the ion-irradiated SiC f / SiC. Journal of Nuclear Materials. 2018;503:226–234. Available from: https://doi.org/10.1016/j.jnucmat.2018.02.045.

[128] Armstrong DEJ. Measuring Elastic , Plastic and Fracture Properties using Micro-Cantilever Testing. University of Oxford; 2009.

[129] Hardie CD. Micro-Mechanics of Irradiated Fe-Cr Alloys for Fusion Reactors. University of Oxford; 2013.

[130] Gibson JSKL. Mechanical Behaviour of Irradiated Tungsten for Fusion Power. Univeristy of Oxford; 2015.

[131] Armstrong DEJ, Hardie CD, Gibson JSKL, Bushby AJ, Edmondson PD, Roberts SG. Small-scale characterisation of irradiated nuclear materials: Part II nanoindentation and micro-cantilever testing of ion irradiated nuclear materials. Journal of Nuclear Materials. 2015;462:374–381. Available from: http://linkinghub.elsevier.com/retrieve/pii/S0022311515000690.

[132] Bull SJ. Nanoindentation of coatings. Journal of Physics D: Applied Physics. 2005;38(24):R393–R413.

[133] Rohbeck N, Tsivoulas D, Shapiro IP, Xiao P, Knol S, Escleine JM, et al. In-situ nanoindentation of irradiated silicon carbide in TRISO particle fuel up to 500 C. Journal of Nuclear Materials. 2015;465:692–694. Available from: http://linkinghub.elsevier.com/retrieve/pii/S002231151530060X.

[134] Hosemann P, Kiener D, Wang Y, Maloy SA. Issues to consider using nano indentation on shallow ion beam irradiated materials. Journal of Nuclear Materials. 2012 jun;425(1-3):136–139. Available from: http://www.sciencedirect.com/science/article/pii/S0022311511010269.

[135] Oliver WC, Pharr GM. An improved technique for determining hardness and elastic modulus using load and displacement sensing indentation experiments. Journal of Materials Research. 1992;7(6):1564–1583.

[136] Pharr GM, Oliver WC. Measurement of Thin Film Mechanical Properties Using Nanoindentation. MRS Bulletin. 1992;17(7):28–33.

[137] Pharr GM, Oliver WC, Brotzen FR. On the generality of the relationship among contact stiffness, contact area, and elastic modulus during indentation. Cambridge University Press; 1992. Available from: http://journals.cambridge.org/abstract{_}S088429140001582X.

[138] Li X, Bhushan B. A review of nanoindentation continuous stiffness measurement technique and its applications. Materials Characterization. 2002;48:11–36.

[139] Pharr GM. Measurement of mechanical properties by ultra-low load indentation. Materials Science and Engineering: A. 1998 sep;253(1-2):151–159. Available from: http://www.sciencedirect.com/science/article/pii/S0921509398007242.

[140] Oliver WC, Pharr GM. Measurement of hardness and elastic modulus by instrumented indentation : Advances in understanding and refinements to methodology. J Mater Res. 2004;19(1):3–20.

[141] Schuh CA, Lund AC. Application of nucleation theory to the rate dependence of incipient plasticity during nanoindentation. Journal of Materials Research. 2011 mar;19(07):2152–2158. Available from: http://journals.cambridge.org/abstract{_}S0884291400094759.

[142] Zhao X, Langford RM, Shapiro IP, Xiao P. Onset Plastic Deformation and Cracking Behavior of Silicon Carbide under Contact Load at Room Temperature. Journal of the American Ceramic Society. 2011 oct;94(10):3509–3514. Available from: http://doi.wiley.com/10.1111/j.1551-2916.2011.04674.x.

[143] Bhakhri V, Wang J, Ur-rehman N, Ciurea C, Giuliani F, Vandeperre LJ. Instrumented nanoindentation investigation into the mechanical behavior of ceramics at moderately elevated temperatures. Journal of Materials Research. 2011 sep;27(01):65–75. Available from: http://journals.cambridge.org/abstract{_}S0884291411002469.

[144] Ostojic P, McPherson R. A review of indentation fracture theory: its development, principles and limitations. International Journal of Fracture. 1987;33(4):297–312.

[145] Nawaz A, Islam B, Mao W, Lu C, Shen Y. Nanoscale elasticplastic deformation and mechanical properties of 3C SiC thin film using nanoindentation. International Journal of Applied Ceramic Technology. 2019;16(August 2018):706–717.

[146] Alvarado-Rivera J, Muñoz-Saldaña J, Ramírez-Bon R. Determination of fracture toughness and energy dissipation of SiO2-poly(methyl metacrylate) hybrid films by nanoindentation. Thin Solid Films. 2011;519(16):5528–5534. Available from: http://linkinghub.elsevier.com/retrieve/pii/S0040609011008340.

[147] Tandon R, Green DJ, Cook RF. Surface Stress Effects on Indentation Fracture Sequences. Journal of the American Ceramic Society. 1990;73(9):2619–2627.

[148] Guo Y, Staedler T, Müller J, Heuser S, Butz B, Jiang X. A detailed analysis of the determination of fracture toughness by nanoindentation induced radial cracks. Journal of the European Ceramic Society. 2020;40(2):276–289. Available from: https://doi.org/10.1016/j.jeurceramsoc.2019.10.013.

[149] Lawn BR. Indentation of Ceramics with Spheres: A Century after Hertz. Journal of the American Ceramic Society. 2005;81(8):1977–1994.

[150] Li Y, Li Y, Xiao W. Point defects and grain boundary effects on tensile strength of 3C-SiC studied by molecular dynamics simulations. Nuclear Engineering and Technology. 2019;51(3):769–775. Available from: https://doi.org/10.1016/j.net.2018.12.010.

[151] Li W, Shirvan K. ABAQUS analysis of the SiC cladding fuel rod behavior under PWR normal operation conditions. Journal of Nuclear Materials. 2019;515:14–27. Available from: https://doi.org/10.1016/j.jnucmat.2018.12.017.

[152] Pang KH, Tymicki E, Roy A. Indentation in single-crystal 6H silicon carbide : Experimental investigations and finite element analysis. International Journal of Mechanical Sciences. 2018;144:858–864. Available from: https://doi.org/10.1016/j.ijmecsci.2017.11.021.

[153] Liu C, Szlufarska I. Distribution of defect clusters in the primary damage of ion irradiated 3C-SiC. Journal of Nuclear Materials. 2018;509:392–400. Available from: https://doi.org/10.1016/j.jnucmat.2018.07.010.

[154] Song X, Niu L. Effect of uniaxial stress on the threshold displacement energy of silicon carbide. Journal of Applied Physics. 2018;124(105105).

[155] Cowen BJ, El-genk MS. Point defects production and energy thresholds for displacements in crystalline and amorphous SiC. Computational Materials Science. 2018;151:73–83. Available from: https://doi.org/10.1016/j.commatsci.2018.04.063.

[156] Singh G, Terrani K, Katoh Y. Thermo-mechanical assessment of full SiC / SiC composite cladding for LWR applications with sensitivity analysis. Journal of Nuclear Materials. 2018;499:126–143. Available from: https://doi.org/10.1016/j.jnucmat.2017.11.004.

[157] Saha U, Devan K. The computation of displacement damage cross sections of silicon, carbon and silicon carbide for high energy applications. Materials Today: Proceedings. 2018;5(8):16501–16508. Available from: https://doi.org/10.1016/j.matpr.2018.06.003.

[158] Sahoo DR, Szlufarska I, Morgan D, Swaminathan N. Role of pre-existing point defects on primary damage production and amorphization in silicon carbide (β -SiC). Nuclear Inst and Methods in Physics Research, B. 2018;414:45–60. Available from: https://doi.org/10.1016/j.nimb.2017.10.011.

[159] Zhao Q, Zhang Z, Li Y, Ouyang X. The mechanical and thermodynamical properties of beta-Si1-xC. RSC Advances. 2017;7:28499–28505.

[160] Katoh Y, Snead LL, Szlufarska I, Weber WJ. Radiation effects in SiC for nuclear structural applications. Current Opinion in Solid State and Materials Science. 2012;16(3):143–152. Available from: http://www.sciencedirect.com/science/article/pii/S1359028612000095.

[161] Simeone D, Costantini JM, Luneville L, Desgranges L, Trocellier P, Garcia P. Characterization of radiation damage in ceramics: Old challenge new issues? Journal of Materials Research. 2015 apr;30(09):1–21. Available from: http://journals.cambridge.org/abstract{_}S0884291415000771.

[162] Lu W, Wang W, Jiang H, Zuo G, Pan B, Xu W, et al. Investigation of wetting property between liquid lead lithium alloy and several structural materials for Chinese DEMO reactor. Journal of Nuclear Materials. 2017;494:303–310. Available from: http://dx.doi.org/10.1016/j.jnucmat.2017.07.055.

[163] Nozawa T, Ozawa K, Park C, Park JS, Kohyama A, Hasegawa A, et al. Japanese activities of the R & D on silicon carbide composites in the broader approach period and beyond. Journal of Nuclear Materials. 2018;511:582–590. Available from: https://doi.org/10.1016/j.jnucmat.2018.05.045.

[164] Goldstein J. Scanning Electron Microscopy and X-ray Microanalysis : A Text for Biologists, Materials Scientists, and Geologists. New York ; London : Plenum; 1981.

[165] Korte S, Stearn RJ, Wheeler JM, Clegg WJ. High temperature microcompression and nanoindentation in vacuum. Journal of Materials Research. 2012;27(1):167–176.

[166] Trenkle JC, Packard CE, Schuh CA. Hot nanoindentation in inert environments. Review of Scientific Instruments. 2010;81(073901).

[167] Wheeler JM, Michler J. Invited Article: Indenter materials for high temperature nanoindentation. The Review of scientific instruments. 2013 oct;84(10):101301. Available from: http://ezproxy-prd.bodleian.ox.ac.uk:2837/content/aip/journal/rsi/84/10/10.1063/1.4824710http://www.ncbi.nlm.nih.gov/pubmed/24182094.

[168] Wachtman JBJ, Tefft WE, Lam DGJ, Apstein CS. Exponential Temperature Dependence of Young's Modulus for Serveral Oxides. Physical Review. 1961;122(6):1754–1759. Available from: https://link.aps.org/doi/10.1103/PhysRev.122.1754.

[169] Young RJ. Micro-machining a focused ion beam. Vacuum. 1993;44(3-4):353–356.

[170] Trtik P, Reeves CM, Bartos PJM. Use of focused ion beam (FIB) for advanced interpretation of microindentation test results applied to cementitious composites. Materials and Structures. 2000;33(April):189–193.

[171] Bischoff L, Teichert J, Heera V. Focused ion beam sputtering investigations on SiC. Applied Surface Science. 2001;184:372–376.

[172] Dunzik-Gougar ML, Rooyen IJV, Hill CM, Trowbridge T, Madden J, Burns J. Sample Preparation Techniques for Grain Boundary Characterization of Annealed TRISO- Coated Particles. Nuclear Technology. 2017;196(1):111–120.

[173] Veerapandian SKP, Beuer S, Rumler M, Stumpf F, Thomas K, Pillatsch L, et al. Comparison of silicon and 4H silicon carbide patterning using focused ion beams. Nuclear Inst and Methods in Physics Research, B. 2015;365:44–49. Available from: http://dx.doi.org/10.1016/j.nimb.2015.07.079.

[174] Lehrer C, Frey L, Mizutani M, Takai M, Ryssel H. Defects and Gallium - Contamination During Focused Ion Beam Micro Machining. In: International Conference on Ion Implantation Technology; 2000. p. 695–698.

[175] Ziegler JF, Ziegler MD, Biersack JP. SRIM The stopping and range of ions in matter (2010). Nuclear Instruments and Methods in Physics Research Section B: Beam Interactions with Materials and Atoms. 2010 jun;268(11-12):1818–1823. Available from: http://linkinghub.elsevier.com/retrieve/pii/S0168583X10001862.

[176] Stoller RE, Toloczko MB, Was GS, Certain AG, Dwaraknath S, Garner FA. On the use of SRIM for computing radiation damage exposure. Nuclear Inst and Methods in Physics Research, B. 2013;310:75–80. Available from: http://dx.doi.org/10.1016/j.nimb.2013.05.008.

[177] Bratchenko MI, Bryk VV, Dyuldya SV, Kalchenko AS, Lazarev NP, Voyevodin VN. Comments on DPA calculation methods for ion beam driven simulation irradiations. Problems of Atmoic Science and Technology. 2013;(2):11–16.

[178] Devanathan R, Weber WJ. Displacement energy surface in 3C and 6H SiC. Journal of Nuclear Materials. 2000;278:258–265.

[179] Angelini P, Sevely J, Hasein K, Zanchi G. No Title. In: Joy DC, editor. Analytical Electron Microscopy. San Fransisco Press; 1987. p. 267.

[180] Jiang W, Weber WJ, Thevuthasan S, McCready DE. Displacement energy measurements for ion-irradiated 6HSiC. Nuclear Instruments and Methods in Physics Research Section B: Beam Interactions with Materials and Atoms. 1999;148(1):557–561.

[181] Rempel AA, Sprengel W, Blaurock K, Reichle KJ, Major J, Schaefer HE. Identification of Lattice Vacancies on the Two Sublattices of SiC. Physical Review Letters. 2002 oct;89(18):185501. Available from: http://link.aps.org/doi/10.1103/PhysRevLett.89.185501.

[182] Kerbiriou X, Barthe MF, Esnouf S, Desgardin P, Blondiaux G, Petite G. Silicon displacement threshold energy determined by electron paramagnetic resonance and positron annihilation spectroscopy in cubic and hexagonal polytypes of silicon carbide. Journal of Nuclear Materials. 2007 may;362(2-3):202–207. Available from: http://linkinghub.elsevier.com/retrieve/pii/S0022311507000529.

[183] Volm D, Meyer BK, Mokhov EN, Baranov PG. Radiation Defects in SiC - Electron Irradiation With Different Energies. MRS Proceedings. 1994 jan;339(6):705. Available from: http://journals.cambridge.org/abstract{_}S1946427400408596.

[184] Steeds JW, Evans GA, Danks LR, Furkert S, Voegeli W, Ismail MM, et al. Transmission electron microscope radiation damage of 4H and 6H SiC studied by photoluminescence spectroscopy. Diamond and Related Materials. 2002;11(12):1923–1945.

[185] Barry AL. Energy Dependence of electron damage and displacement threshold energy in 6H Silicon Carbide. IEEE Transactions on Nuclear Science. 1991;38(6):1111–1115.

[186] Inui H, Mori H, Fujita H. Electron-irradiation-induced crystalline to amorphous transition in α-Sic single crystals. Philosophical Magazine Part B. 1990 jan;61(1):107–124. Available from: http://www.tandfonline.com/doi/abs/10.1080/13642819008208655.

[187] Hudson B, Sheldon BE. High voltage electron transmission microscopy of pyrolytic silicon carbide coatings from nuclear fuel particles. Journal of Microscopy. 1973 jan;97(1-2):113–119. Available from: http://doi.wiley.com/10.1111/j.1365-2818.1973.tb03765.x.

[188] Zinkle SJ, Kinoshita C. Defect production in ceramics. Journal of Nuclear Materials. 1997;251:200–217.

[189] Hønstvet IA, Smallman RE, Marquis PM. A determination of the atomic displacement energy in cubic silicon carbide. Philosophical Magazine A. 1980 feb;41(2):201–207. Available from: http://www.tandfonline.com/doi/abs/10.1080/01418618008236135.

[190] Geiczy II, Nesterov AA, Smirnov LS. Luminescence of irradiated β-SiC. Radiation Effects. 1971 jun;9(3-4):243–246. Available from: http://www.tandfonline.com/doi/abs/10.1080/00337577108231054.

[191] Raman CV, Krishnan KS. A New Type of Secondary Radiation. Nature. 1928;121(3048):501–502.

[192] Nakashima S, Harima H. Raman Investigation of SiC Polytypes. physica status solidi (a). 1997 jul;162(1):39–64. Available from: http://doi.wiley.com/10.1002/1521-396X(199707)162:1{%}3C39::AID-PSSA39{%}3E3.0.CO;2-L.

[193] Bumbrah GS, Sharma RM. Raman spectroscopy Basic principle, instrumentation and selected applications for the characterization of drugs of abuse. Egyptian Journal of Forensic Sciences. 2015;Available from: http://www.sciencedirect.com/science/article/pii/S2090536X15000477.

[194] Leide A. Reaction-bonded silicon carbide for nuclear fusion blanket applications. University of Oxford; 2019.

[195] Jannotti P, Subhash G, Zheng J, Halls V. Measurement of microscale residual stresses in multi-phase ceramic composites using Raman spectroscopy. Acta Materialia. 2017;129:482–491. Available from: http://dx.doi.org/10.1016/j.actamat.2017.03.015.

[196] Miro S, Bordas E, Thome L, Costantini J, Lepretre F, Trocellier P, et al. Monitoring of the microstructure of ion-irradiated nuclear ceramics by in situ Raman spectroscopy. Journal of Raman Spectroscopy. 2016;47:476–485.

[197] Kang Y, Qiu Y, Lei Z, Hu M. An application of Raman spectroscopy on the measurement of residual stress in porous silicon. Optics and Lasers in Engineering. 2005;43(8):847–855.

[198] Inoue Y, Nakashima S, Mitsuishi A, Tabata S, Tsuboi S. Raman Spectra of amorphous SiC. Solid State Communications. 1983;48(12):1071–1075.

[199] Koyanagi T, Lance MJJ, Katoh Y. Quantification of irradiation defects in beta-silicon carbide using Raman spectroscopy. Scripta Materialia. 2016 dec;125:58–62. Available from: http://dx.doi.org/10.1016/j.scriptamat.2016.08.004http://linkinghub.elsevier.com/retrieve/pii/S1359646216303724.

[200] Chauhan VS, Riyad MF, Du X, Wei C, Tyburska-Püschel B, Zhao JC, et al. Thermal Conductivity Degradation and Microstructural Damage Characterization in Low-Dose Ion Beam-Irradiated 3C-SiC. Metallurgical and Materials Transactions E. 2017;4(December):61–69. Available from: http://link.springer.com/10.1007/s40553-017-0107-3.

[201] Matsumoto M, Huang H, Harada H, Kakimoto K, Yan J. On the phase transformation of single-crystal 4H-SiC during nanoindentation. Journal of Physics D: Applied Physics. 2017 jul;50(26):265303. Available from: http://stacks.iop.org/0022-3727/50/i=26/a=265303?key=crossref.09317b0b4db364e7ce1e8d0017b80942.

[202] Groth BP, Langan SM, Haber RA, Mann AB. Relating residual stresses to machining and finishing in silicon carbide. Ceramics International. 2016;42(1):799–807. Available from: http://dx.doi.org/10.1016/j.ceramint.2015.08.179.

[203] De Wolf I. Micro-Raman spectroscopy to study local mechanical stress in silicon integrated circuits. Semiconductor Science and Technology. 1996;11(2):139–154.

[204] Okumura H, Sakuma E, Lee JH, Mukaida H, Misawa S, Endo K, et al. Raman scattering of SiC: Application to the identification of heteroepitaxy of SiC polytypes. Journal of Applied Physics. 1987;61(3):1134. Available from: http://scitation.aip.org/content/aip/journal/jap/61/3/10.1063/1.338157.

[205] Goehlert K, Irmer G, Michalowsk L, Monecke J. Polytype analysis of SiC Powders by Raman Spectroscopy. Journal of Molecular Structure. 1990;219:135–140.

[206] Costantini JM. Study of the Ion-Irradiation Behavior of Advanced SiC Fibers by Raman Spectroscopy and Transmission Electron Microscopy. Journal of American Ceramics Society. 2015;98(2):675–682.

[207] Deslandes A, Guenette MC, Thomsen L, Ionescu M, Karatchevtseva I, Lumpkin GR. Retention and damage in 3C- beta SiC irradiated with He and H ions. Journal of Nuclear Materials. 2016;469:187–193. Available from: http://dx.doi.org/10.1016/j.jnucmat.2015.11.022.

[208] Lawn BR, Evans AG, Marshall DB. Elastic/Plastic Indentation Damage in Ceramics: the Median/Radial Crack System. Journal of the American Ceramic Society. 1980;63(9-10):574–581.

[209] Schiffmann KI. Determination of fracture toughness of bulk materials and thin films by nanoindentation: comparison of different models. Philosophical Magazine. 2011;91(7-9):1163–1178. Available from: http://www.tandfonline.com/doi/abs/10.1080/14786435.2010.487984.

[210] Laugier MT. Palmqvist indentation toughness in WC-Co composites. Journal of Materials Science Letters. 1987;6(8):897–900.

[211] Ouchterlony F. Stress Intensity Factors for the Expansion loaded star crack. Engineering Fracture Mechanics. 1976;8:447–448.

[212] Gouadec G, Colomban P. Raman Spectroscopy of nanomaterials: How spectra relate to disorder, particle size and mechanical properties. Progress in Crystal Growth and Characterization of Materials. 2007;53(1):1–56.

[213] Sorieul S, Costantini JM, Gosmain L, Calas G, Thome L, Grob JJ. Raman spectroscopy study of heavy-ion-irradiated α-SiC. Journal of Physics: Condensed Matter. 2006 jun;18(22):5235–5251. Available from: http://stacks.iop.org/0953-8984/18/i=22/a=022?key=crossref.02bd6a71d821f4170be2194c2a90ba02.

[214] Harima H. Raman scattering characterization on SiC. Microelectronic Engineering. 2006;83(1 SPEC. ISS.):126–129.

[215] Chen X, Zhou W, Feng Q, Zheng J, Liu X, Tang B, et al. Irradiation effects in 6H - SiC induced by neutron and heavy ions : Raman spectroscopy and high-resolution XRD analysis. Journal of Nuclear Materials. 2016;478:215–221. Available from: http://dx.doi.org/10.1016/j.jnucmat.2016.06.020.

[216] Yan J, Gai X, Harada H. Subsurface damage of single crystalline silicon carbide in nanoindentation tests. Journal of nanoscience and nanotechnology. 2010 nov;10(11):7808–11. Available from: http://www.ncbi.nlm.nih.gov/pubmed/21138038.

[217] Kim JH, Lee HK, Park JY, Kim WJ, Kim DK. Mechanical properties of chemical-vapor-deposited silicon carbide using a nanoindentation technique. Journal of the Korean Ceramic Society. 2008;45(9):518–523.

[218] Lankford J, Davidson DL. Indentation plasticity and microfracture in silicon carbide. Journal of Materials Science. 1979 jul;14(7):1669–1675. Available from: http://link.springer.com/10.1007/BF00569289.

[219] Chen J, Jung P, Trinkaus H. Microstructural evolution of helium-implanted α-SiC. Physical Review B. 2000 may;61(19):12923–12932. Available from: http://link.aps.org/doi/10.1103/PhysRevB.61.12923.

[220] Tromas C, Audurier V, Leclerc S, Beaufort MF, Declémy a, Barbot JF. Evolution of mechanical properties of SiC under helium implantation. Journal of Nuclear Materials. 2008;373:142–149.

[221] Ning K, Lu K, Bodnar RJ. High dose self-ion irradiation of silicon carbide with nanostructured ferritic alloy aid. Journal of Materials Science. 2019;54(1):605–612. Available from: https://doi.org/10.1007/s10853-018-2824-0.

[222] Zang H, Yang T, Guo D, Xi J, He C, Wang Z, et al. Modifications of SiC under high fluence Kr-ion irradiation at different temperatures. Nuclear Inst and Methods in Physics Research, B. 2013;307:558–561. Available from: http://dx.doi.org/10.1016/j.nimb.2012.11.089.

[223] Wright RB, Gruen DM. Raman scattering study of ion bombardment induced amorphization of SiC. Radiation Effects. 1977;33(3):133–140.

[224] Dong S, Katoh Y, Kohyama A. Preparation of SiC / SiC Composites by Hot Pressing , Using Tyranno-SA Fiber as Reinforcement. Journal of American Ceramics Society. 2003;86(1):26–32.

[225] Novitskaya E, Khalifa HE, Graeve OA. Microhardness and microstructure correlations in SiC / SiC composites. Materials Letters. 2018;213:286–289.

[226] ASTM International. Standard Test Method for Flexural Properties of Continuous Fiber-Reinforced Advanced Ceramic Composites; 2016.

[227] GA. General Atomics correspondence; 2016.

[228] Chan HM. Layered ceramics: Processing and mechanical behavior. Annual Review of Materials Science. 1997;27(1):249–282.

[229] Zhao P, Ji S. Refinements of shear-lag model and its applications. Tectonophysics. 1997;279(1-4):37–53.

[230] Rodríguez-Castro R, Wetherhold RC, Kelestemur MH. Microstructure and mechanical behavior of functionally graded Al A359/SiCp composite. Materials Science and Engineering A. 2002;323(1-2):445–456.

[231] Vecchio KS, Jiang F. Fracture toughness of Ceramic-Fiber-Reinforced Metallic-Intermetallic-Laminate (CFR-MIL) composites. Materials Science and Engineering A. 2016;649:407–416. Available from: http://dx.doi.org/10.1016/j.msea.2015.10.018.

[232] Koyanagi T, Kondo S, Hinoki T. The influence of sintering additives on the irradiation resistance of NITE SiC. Journal of Nuclear Materials. 2011;417(1):435–439. Available from: http://dx.doi.org/10.1016/j.jnucmat.2010.12.181http://www.sciencedirect.com/science/article/pii/S0022311510010032.

[233] Shimoda K, Hinoki T, Kohyama A. Effect of additive content on transient liquid phase sintering in SiC nanopowder infiltrated SiC f / SiC composites. Composites Science and Technology. 2011;71(5):609–615. Available from: http://dx.doi.org/10.1016/j.compscitech.2010.12.014.

[234] Koyanagi T, Kondo S, Hinoki T. Effect of differential swelling between fiber and matrix on the strength of irradiated SiC/SiC composites. Journal of Nuclear Materials. 2013 nov;442(1-3):S380–S383. Available from: http://www.sciencedirect.com/science/article/pii/S0022311513005953.

[235] Nix WD, Gao H. Indentation size effects in crystalline materials: A law for strain gradient plasticity. Journal of Mechanics and Physics of Solids. 1998;46(3):411–425.

[236] Li BS. Email Correspondence; 2019.

[237] Kerbiriou X, Costantini JM, Sauzay M, Sorieul S, Thome L, Jagielski J, et al. Amorphization and dynamic annealing of hexagonal SiC upon heavy-ion irradiation: Effects on swelling and mechanical properties. Journal of Applied Physics. 2009;105(7):073513. Available from: http://scitation.aip.org/content/aip/journal/jap/105/7/10.1063/1.3103771.

[238] Beake BD, Harris AJ. Nanomechanics to 1000 C for high temperature mechanical properties of bulk materials and hard coatings. Vacuum. 2019;159(May 2018):17–28. Available from: https://doi.org/10.1016/j.vacuum.2018.10.011.

[239] Rohbeck N, Xiao P. Evaluation of the mechanical performance of silicon carbide in TRISO fuel at high temperatures. Nuclear Engineering and Design. 2016;.

[240] Rohbeck N. The High Temperature Mechanical Properties of SiC in TRISO Particle Fuel. University of Manchester; 2014.

[241] Snead LL, Katoh Y, Koyanagi T, Terrani K. Stored energy release in neutron irradiated silicon carbide. Journal of Nuclear Materials. 2019;514:181–188. Available from: https://doi.org/10.1016/j.jnucmat.2018.12.005.

[242] Malherbe JB, van der Berg NG, Botha AJ, Friedland E, Hlatshwayo TT, Kuhudzai RJ, et al. SEM analysis of ion implanted SiC. Nuclear Instruments and Methods in Physics Research Section B: Beam Interactions with Materials and Atoms. 2013 nov;315:136–141. Available from: http://www.sciencedirect.com/science/article/pii/S0168583X13006551.

[243] Malherbe JB, Berg NGVD, Kuhudzai RJ, Hlatshwayo TT, Thabethe TT, Odutemowo OS, et al. Nuclear Instruments and Methods in Physics Research B Scanning electron microscopy of the surfaces of ion implanted SiC. Nuclear Inst and Methods in Physics Research, B. 2015;354:23–27. Available from: http://dx.doi.org/10.1016/j.nimb.2015.01.045.

[244] Haušild P, Čech J, Materna A, Matějíček J. Statistical treatment of grid indentation considering the effect of the interface and the microstructural length scale. Mechanics of Materials. 2019;129:99–103. Available from: https://doi.org/10.1016/j.mechmat.2018.11.006.